CENPD-285-NP

FUEL ROD DESIGN METHODS FOR BOILING WATER REACTORS

ABB Combustion Engineering Nuclear Operations

LEGAL NOTICE

THIS REPORT WAS PREPARED AS AN ACCOUNT OF WORK SPONSORED BY COMBUSTION ENGINEERING, INC. NEITHER COMBUSTION ENGINEERING, INC. NOR ANY PERSON ACTING ON ITS BEHALF:

A. MAKES ANY WARRANTY OR REPRESENTATION, EXPRESS OR IMPLIED INCLUDING THE WARRANTIES OF FITNESS FOR A PARTICULAR PURPOSE OR MERCHANTABILITY, WITH RESPECT TO THE ACCURACY, COMPLETENESS, OR USEFULNESS OF THE INFORMATION CONTAINED IN THIS REPORT, OR THAT THE USE OF ANY INFORMATION, APPARATUS, METHOD, OR PROCESS DISCLOSED IN THIS REPORT MAT NOT INFRINGE PRIVATELY OWNED RIGHTS; OR

B. ASSUMES ANY LIABILITIES WITH RESPECT TO THE USE OF, OR FOR DAMAGES RESULTING FROM THE USE OF, ANY INFORMATION, APPARATUS, METHOD OR PROCESS DISCLOSED IN THIS REPORT.

CENPD-285-NP

Fuel Rod Design Methods for Boiling Water Reactors

May 1994

ABB Combustion Engineering Nuclear Operations

TABLE OF CONTENTS

TABLE OF CONTENTS (Continued)

TABLE OF CONTENTS (Continued)

TABLE OF CONTENTS (Continued)

TABLE OF CONTENTS (Continued)

TABLE OF CONTENTS (Continued)

1 INTRODUCTION

This Licensing Topical Report presents three computer codes, STAV6.2, VIK-2, and COLLAPS-II, used for analysis of the fuel rod thermal and mechanical performance. The correlations, models, and calculational methods used in each code are discussed in this document. Evaluations are also provided which demonstrate that the codes are qualified for fuel rod design and safety analyses.

1.1 Summary and Conclusions

It is concluded from the qualification evaluations in this document that the fuel rod performance computer code, STAV6.2, is qualified for determination: (1) of fuel rod performance relative to thermal-mechanical limits and, (2) for evaluation of nuclear fuel rod performance parameters for input into reload safety analyses. The calculational methods in STAV6.2 have been demonstrated through separate effects and synergistic interaction benchmarking, to be qualified for predicting fuel rod performance. For example, the STAV6.2 code has been qualified for prediction of the following fuel rod performance effects as a function of burnup:

(1) Fuel pellet and cladding temperature, heat capacity, and thermal conductivity,

(2) Fuel pellet and cladding dimensional changes,

(3) Fission gas release and internal rod gas pressure,

(4) Pellet-cladding gap heat transfer,

(5) Pellet-cladding mechanical interaction (PCMI),

(6) Cladding corrosion and hydriding rates.

The STAV6.2 code uses energy conservation equations, mechanistic models, and constitutive correlations, to predict the fuel pellet, void volume, and cladding performance under quasi-static nuclear irradiation conditions. Separate effects and integral phemonena are shown to be consistently and accurately modeled by qualification comparisons to experimental and in-plant data. Individual models for specific phemonena (e.g., fission gas release, cladding corrosion and hydriding, rod growth) are extensively qualified relative to data available in the literature and proprietary data. The integration of the models in STAV6.2 is qualified by integral benchmark comparisons, such as fuel centerline temperature and end-of-life free volume.

The data base currently available demonstrates the STAV6.2 code can accurately predict fuel rod performance to a rod burnup of 60,000 MWd/MtU.

The cladding stress analysis code, VIK-2, evaluates classical stress-strain formulas to determine beginning-of-life cladding stresses. The formulas and models are used to determine the fuel rod cladding axial, radial, and azimuthal stresses in an unirradiated state. The formulas and models are based on universally accepted analytical solutions of classical equations.

The cladding ovality code, COLLAPS-II, evaluates the cladding cross sectional ovality as a function of irradiation. The code is qualified in this document by benchmarking against the NRC-approved CEPAN and BUCKLE-II codes. The code utilizes state-of-the-art elastic and plastic cladding models to evaluate margin to cladding collapse and a cladding creep model based on the ABB data base.

Based on the qualification evaluations in this report, it is concluded that STAV6.2, VIK-2, and COLLAPS-II are acceptable for referencing in design and licensing applications for:

(1) Fuel rod performance relative to thermal-mechanical limits, for example, end-of-life rod pressure, cladding strain, fuel melting, gap conductance, etc. and

(2) Initial conditions for safety analyses evaluations, i.e., LOCA, overpower transients, minimum critical power ratio, and fuel melt evaluations.

1.2 Fuel Rod Mechanical Design and Licensing Applications

This Licensing Topical Report describes the methods used to evaluate the fuel rod performance under varying pressure, power, temperature, and irradiation conditions. The fuel rod design bases and methodologies used to apply the computer codes described herein, to applications in fuel assembly reload design, are described in the "ABB Fuel Assembly Mechanical Design Methodology for BWR Fuel" CENPD-287-P (Reference 1-1).

The application methodology of the fuel rod design methods described herein to reload safety analyses is described in "Reference Safety Report for Boiling Water Reactor Reload Fuel," CENPD-300-P (Reference 1-2)

1.3 Overview of Computer Codes

This section contains an overview description of the computer codes used for fuel rod mechanical design and safety analyses calculations.

STAV6.2 is the principal design code used by ABB for BWR fuel performance analyses. The VIK-2 code is a collection of models and formulas used to calculate cladding stresses at the beginning of life. The COLLAPS-II code is used to calculate the cladding ovality as a function of irradiation. A brief overview of the three codes are provided below.

1.3.1 STAV6.2 Computer Code

The STAV6.2* code is used by ABB for BWR and PWR fuel rod performance analyses. This report addresses the application of STAV6.2 in the United States for BWR applications only. STAV6.2 is used in Europe for both BWR and PWR applications. STAV6.2 offers a best-estimate analytical tool for predicting steady-state fuel performance for operation of Light Water Reactor (LWR) fuel rods including UO_2-Gd_2O_3 fuel.

STAV6.2 calculates the variation with time of all important fuel rod performance quantities including fuel and cladding temperatures, fuel densification, fuel swelling, gaseous fission product release, rod pressure, gas gap conductance, cladding stresses and strains due to elastic and thermal creep and plastic deformations, cladding oxidation, and cladding hydriding. Burnup-dependent radial power distributions for both UO_2 and UO_2-Gd_2O_3 fuel, fuel grain growth, and helium release are modeled in the code. A simplified flow-chart of STAV6.2 is shown in Figure 1-1.

The fuel rod geometric parameters, the actual or projected irradiation history, and the core thermal and hydraulic conditions are the required input for initialization of the code.

Rod Geometric Parameters and Modelling

The fuel rod in STAV6.2 is a typical Light Water Reactor (LWR) fuel rod with an active fuel length consisting of fuel pellets enclosed in Zircaloy cladding. A plenum for accommodation of released fission gases is above the fuel stack.

The Zircaloy cladding is modeled as a tube concentric with the fuel pellet column. The cladding material can be either fully-

* STAV is a Swedish word for "rod"

recrystallized Zircaloy-2 or cold-worked and stress-relieved Zircaloy-4.

The active fuel length is separated into axial segments. The plenum region is treated independently as an additional node. The fuel pellets are right circular cylinders.

The code takes into account the void volume of the rod due to pellet dishing, chamfering, and stacking faults. The fuel rod can be pressurized or unpressurized. The fill gas can be any combination of helium, nitrogen, argon, and xenon. Complete and instantaneous mixing of gases in the fuel rod in the void volume is assumed.

Input Power and Fast Flux Histories

The fuel rod power history given by the local linear heat generation rate (LHGR), as a function of burnup or time, can be supplied either from the output of reactor physics codes or input directly. Fast neutron flux is calculated from the power history and a burnup or time-dependent input factor.

Thermal Hydraulic Parameters

The fuel rod pitch, coolant inlet temperature, coolant pressure, and coolant mass flow rates are supplied as inputs for the cladding outer surface temperature calculation.

As shown in Figure 1-1, the STAV6.2 calculational path starts from the coolant with thermal and hydraulic calculations and extends to cladding strain stress calculations and fission gas release calculations.

The heat transfer between the cladding and the coolant is modeled with either single phase convection, subcooled boiling, or saturated flow boiling. [Proprietary Information Deleted]

An important quantity in STAV6.2 is the heat transfer across the pellet-cladding gap and the pellet-cladding contact pressure. The model is phenomenological, is quite detailed, and is interactive with a pellet cladding mechanical model.

The fuel swelling model in STAV6.2 consists of empirical models for the contributions of: [Proprietary Information Deleted]

[Proprietary Information Deleted]

The fission gas release (FGR) model in STAV6.2 consists of an athermal FGR model and a thermal FGR model. The athermal FGR

model accounts for the contribution to FGR by the knock-out process from regions close to surfaces of the pellet periphery and internal cracks. [Proprietary Information Deleted]

A comprehensive description of all the models in STAV6.2 is provided in Section 2.

1.3.2 VIK-2 Computer Code

VIK-2 calculates the cladding stresses at the beginning-of-life (BOL) for a fuel rod. The code consists of subroutines which calculate different stresses on the cladding. These individual stresses are subsequently added according to the Tresca rule or the "Von Mises" rule and compared to the allowed stresses specified by the appropriate design criterion. Standard analytical expressions are used to calculate the stresses. The source of each stress component and the model used to calculate it can be summarized as follows:

Cladding Internal and External Pressure

The stresses caused by loading of a fuel rod by internal gas pressure and external coolant pressure are calculated. [Proprietary Information Deleted]

Pressure at End Plug

Stress components caused by the pressure at the end plug of a fuel rod are calculated. [Proprietary Information Deleted]

Ovality

The initial ellipticity of the cladding under uniform external pressure gives rise to tangential and axial stresses in the fuel cladding. [Proprietary Information Deleted] The model assumes that there is an initial deviation from a perfect circular form in the shape of the cladding tube. Upon loading the non-circular tube with pressure, the further flattening of the tube as a result of pressures on the tube is calculated.

Radial Temperature Gradient

The stresses caused by a radial temperature distribution within the cladding are calculated. [Proprietary Information Deleted]

Azimuthal Temperature

VIK-2 includes a model for calculating the effect on the cladding temperature distribution of asymmetric positioning of the fuel pellets.

Springs

The axial stresses on the fuel rod caused by the internal and external springs are calculated.

Rod Bending

The stresses exerted on the fuel rods caused by flow-induced vibrations are calculated. The model describes the rod as a straight beam clamped at both ends.

Spacer Grid

The stresses applied to the cladding by the spacer grids consist of three components: spacer membrane, spacer bending, and spacer beam bending. The spacer membrane and spacer bending stresses are caused by the spacer springs. The spacer beam bending stresses arise from the bending in a portion of the rod between the spacer and supports. The model describes the cladding and the spacer as cylindrical shells with closed ends supported at the ends.

End Plug Temperature Gradient

The heat transferred from the UO_2 pellet to the bottom end plug causes thermal expansion of this plug. This expansion loads the cladding on the circumferential bottom end plug weld. The axial and radial temperature gradients in the fuel rod are calculated, [Proprietary Information Deleted]

End Plug Angle

Misalignment of the holes in the tie plates and the end plug extensions combined with maximum unfavorable tolerances in tie plates can be postulated to lead to a bending moment in the fuel rods. [Proprietary Information Deleted]

A simplified flow chart of the VIK-2 code calculational process is shown in Figure 1-2. A comprehensive description of the VIK-2 code models is presented in Section 4.

1.3.3 COLLAPS-II Computer Code

COLLAPS-II is used for prediction of cladding ovality in BWR fuel rods as a function of irradiation time.

The COLLAPS-II code models the cladding as a long, thin cylindrical tube which is subject to creep as a result of a uniform net external pressure. The cross section of the tube is assumed to have a slight

initial deviation from circularity. The standard assumptions appropriate to creep deformation analysis of shells are utilized in the COLLAPS-II code.

COLLAPS-II calculates the following quantities as a function of irradiation time:

- Cladding ovality,
- Creep down strain and total axial strain of the cladding, and
- Bending moments of the cladding.

A simplified flow chart of the COLLAPS-II code is shown in Figure 1-3. A comprehensive description of the COLLAPS-II code models is presented in Section 6.

1.4 Overview of Qualification

1.4.1 STAV6.2 Computer Code Qualification

The verification of STAV6.2 includes validation of the individual models used in the code by comparison with pertinent experimental data and integral validation of the synergistic interaction of the code by comparison with in-pile data such as centerline temperature, fraction of fission gas released, cladding creep, and fuel internal volume measurements.

The qualification of STAV6.2 includes benchmarking for PWR as well as BWR applications. The STAV6.2 code is currently used in Europe for both BWR and PWR fuel design and safety analyses. It is currently intended for use in the United States in BWR applications only.

The present evaluations qualifies the STAV6.2 code for light water fuel operating under normal conditions. Rods irradiated in commercial reactors and rods irradiated in experimental reactors have been included in the comparisons between measured data and predicted values.

The benchmarking is divided into the following parts:

(1) Fuel Temperature Comparisons

- Beginning-of-life fuel centerline temperature
- In-life fuel centerline temperature

(2) Gaseous Fission Product Release

- Helium release
- Xenon and krypton production and release
- Low temperature fission gas release
- High Temperature fission gas release

(3) Cladding Models

- Clad creep down
- Pellet-Clad Mechancial Interaction (PCMI)
- Rod growth
- Cladding waterside corrosion/hydriding

(4) End-of-Life Rod Free Volume

Details of the STAV6.2 code qualification are presented in Section 3.

1.4.2 VIK-2 Computer Code Qualification

As describe above, the VIK-2 code is a compilation of classical formulas and models implemented in an integral fashion in a computer code. This approach facilitates quick, accurate calculation of the fuel rod stresses at beginning-of-life. Qualification of VIK-2 consists of verifying proper implementation of the classical formulae and models. This is done by inspection of a spectrum of examples. A description of the VIK-2 code qualification is presented in Section 5 in the form of an input description, several sample input and output listings and clarifying descriptive text.

1.4.3 COLLAPS-II Computer Code Qualification

The computer code COLLAPS-II predicts fuel rod cladding ovality as a function of irradiation time. The program COLLAPS-II uses an original solution method to solve the non-linear, large deflection, thin cylindrical shell equilibrium equations. In the qualification of COLLAPS-II, detailed comparisons are made with the NRC approved codes CEPAN and BUCKLE-II. Owing to the well documented qualification procedures of the CEPAN program, where the CEPAN predictions were thoroughly checked against the predictions of the NRC-program BUCKLE-II, the same testing program has been applied here to COLLAPS-II. [Proprietary Information Deleted]

Details of the COLLAPS-II code qualification are presented in Section 7.

1.5 References

1-1 "ABB Fuel Assembly Mechanical Design Methodology for BWR Fuel," CENPD-287-P, June 1994.

1-2 "Reference Safety Report for Boiling Water Reactor Reload Fuel," CENPD-300-P.

[Proprietary Information Deleted]

Figure 1-1 Simplified STAV6.2 Flow Chart

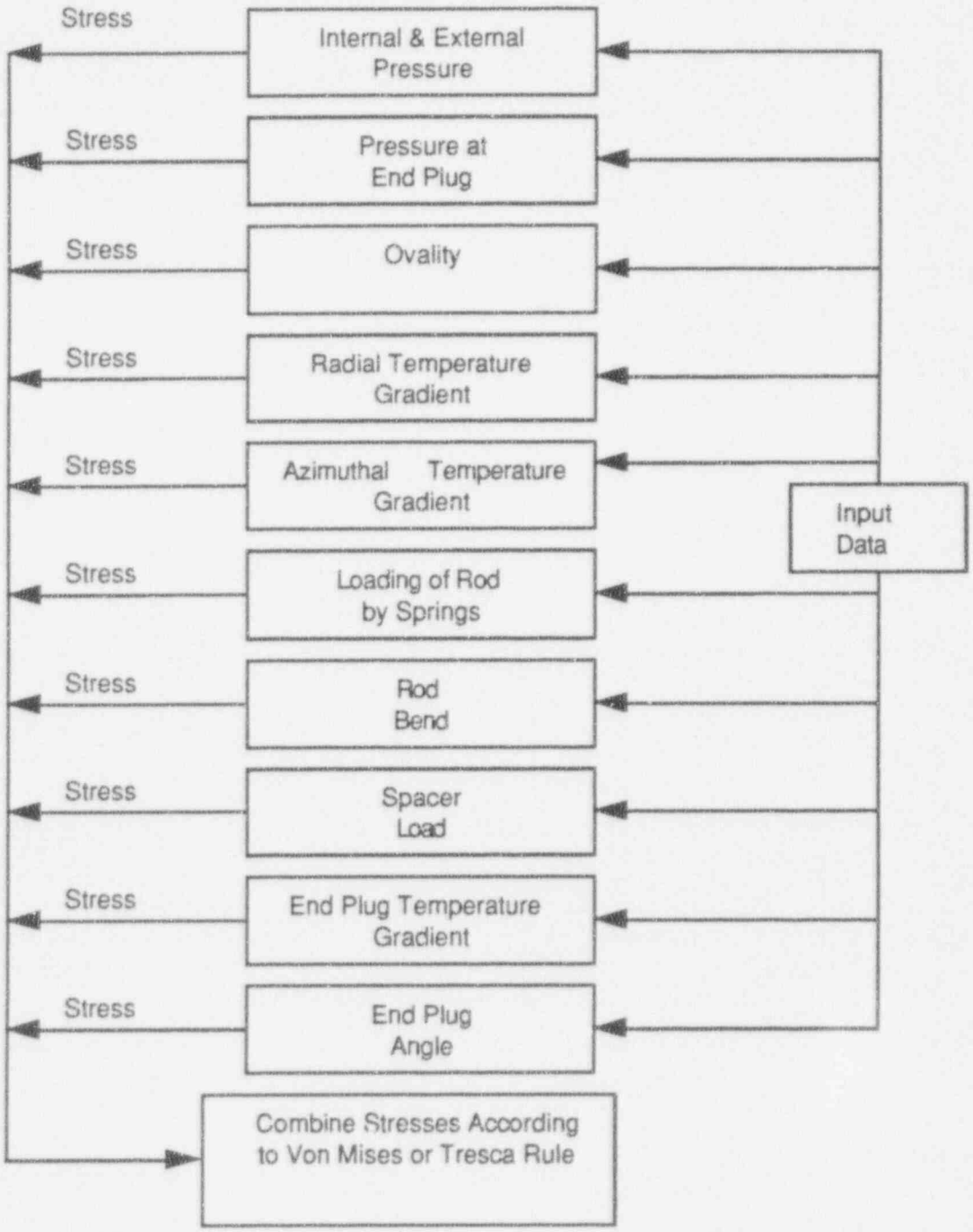

Figure 1-2 VIK-2 Flow Chart

[Proprietary Information Deleted]

Figure 1-3 Simplified COLLAPS-II Flow Chart

2 STAV6.2 COMPUTER CODE MODELS

The STAV6.2 code is the BWR fuel performance code used by ABB for U.S. applications. STAV6.2 affords a best-estimate analytical tool for predicting steady-state fuel performance for operation of light water reactor (LWR) fuel rods including UO_2-Gd_2O_3 fuel.

STAV6.2 calculates the variation with time of all significant fuel rods performance quantities including fuel and cladding temperatures, fuel densification, fuel swelling, fission product gas release, rod pressure, gas gap conductance, cladding stresses and strains due to elastic, thermal, creep and plastic deformations, rod growth, cladding oxidation and cladding hydriding. Other submodels include burnup dependent radial power distribution for both UO_2 and UO_2-Gd_2O_3 fuel, fuel grain growth, and helium release.

The fuel rod geometrical parameters, the actual or projected irradiation history, and the core thermal and hydraulic conditions (system pressure and coolant mass flow) are required inputs for initialization of the code.

Geometric parameters

STAV6.2 models a typical LWR fuel rod with an active fuel length consisting of fuel pellets enclosed in Zircaloy cladding. Above the fuel stack is an end plenum for accommodation of released fission gases. A fuel rod is illustrated in Figure 2-1. The code can also model two individual plena, one at the top and the other at the bottom of the fuel stack.

The Zircaloy cladding is assumed to be concentric with the fuel. The cladding can be Zircaloy-2 or Zircaloy-4. Single values of cladding inner and outer radius are used along the entire rod length.

The active fuel length is separated into axial segments of equal length. The plenum region is treated independently as an additional node. The fuel pellets are right circular cylinders.

The code takes into account the additional void volume in the rod due to pellet dishing and chamfering. The fuel rod can be pressurized or unpressurized. The fill gas can be helium, nitrogen, argon, xenon, or any combination of these. Complete and instantaneous mixing of gases in the fuel rod in the void volume is assumed.

Irradiation parameters

The fuel rod power history is input as axial distributions of the local linear heat generation rate (LHGR) as a function of burnup. [Proprietary Information Deleted]

Thermal-hydraulic parameters

For calculating the cladding outer surface temperature, the subchannel geometry (pitch), coolant inlet temperature, coolant pressure, and coolant mass flow rate are supplied as input to the code.

The heat transfer between the cladding and the coolant is modelled with either single phase convection, subcooled boiling, or saturated flow boiling. [Proprietary Information Deleted]

A crucial quantity in STAV6.2 is the heat transfer across the pellet-clad gap and the pellet-clad contact pressure. [Proprietary Information Deleted]

[Proprietary Information Deleted]

Fission gas release (FGR) model in STAV6.2 consists of two parts: an athermal low temperature FGR model and a thermal FGR model.

The athermal FGR model accounts for the contribution of the release caused by a knock-out process from regions close to the surfaces of the pellet periphery and the internal cracks. [Proprietary Information Deleted]

The model for thermal FGR is a physically based model which takes into account a number of processes in the fuel and the amount released. The processes include fission gas migration in UO_2 grains, irradiation induced resolution, and grain boundary saturation. An equivalent sphere model for UO_2 or UO_2-Gd_2O_3 grains is assumed.

STAV6.2 has been calibrated with in-reactor fuel rod performance data. The data include

- Fuel centerline temperature
- Clad creep down
- Pellet-clad-mechanical interaction
- Fission gas release

- Fuel rod internal void volume

The details of the benchmarking of the code with measured data are presented in Section 3.

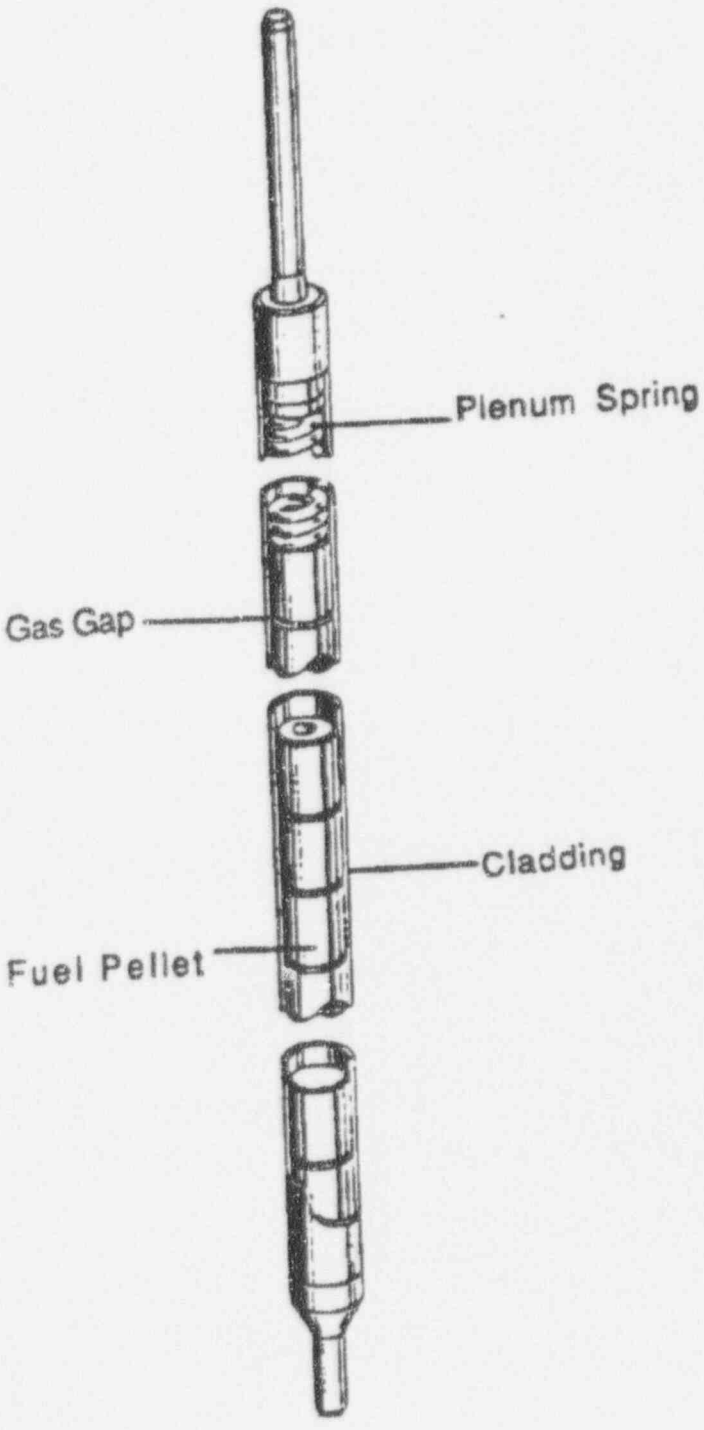

Figure 2-1 BWR Fuel Rod

2.1 Fuel Rod Pellet Models

Fuel pellets can be either UO_2 or UO_2-Gd_2O_3 material. Models of the fuel apply to normal operations (non-accident conditions) of light water reactor fuel.

[Proprietary Information Deleted]

The following sections describe the calculation of the fuel pellet radial temperature distribution, power distribution, change in volume, relocation, fission gas release and helium release.

2.1.1 Radial Temperature Distribution

The fuel temperature distribution in STAV6.2 is a steady-state description. The radial temperature distribution at each axial segment for a given power at each time step is calculated. The model describes both solid and annular pellets. The pellet is subdivided into annular rings. The steady-state heat conduction equation with uniform volumetric heat generation is considered:

$$-\frac{d}{dr}\left[r\,k(T)\frac{dT}{dr}\right] = S(r)\,r \qquad (2.1\text{-}1)$$

where $S(r) = Q\,F(r)$ is the radial source density distribution (W/m^3), T the temperature, k the thermal conductivity, Q the linear heat generation rate (W/m), and F(r) the radial power distribution density for a given axial node normalized to unity via:

$$F(r) = \frac{f(r)}{\int_{R_i}^{R_0} f(r)\,2\pi r\,dr} \qquad (2.1\text{-}2)$$

and, therefore

$$\int_{R_i}^{R_0} F(r)\,2\pi r dr = 1 \qquad (2.1\text{-}3)$$

with

f(r) = radial power distribution, dimensionless

R_0 = outer radius of pellet, m

R_i = inner radius of pellet, m

k = fuel pellet thermal conductivity, W/m K

r = radius from pellet center, m

In STAV6.2 the pellet is discretized into N concentric annuli, of radii $R_i = r(1) < r(2) < \ldots < r(N+1) = R_0$, (see Figure 2.1-1) and it is assumed that the integrals:

$$W(i) = \int_{R_i}^{r(i)} F(r)\, 2\pi r\, dr, \quad i = 2,3,\ldots,N+1 \tag{2.1-4}$$

are known apriori, where W(1)=0 and W(N+1)=1 by definition. Thus W(i) is the portion of the total heat generated within radius r of the pellet and as such it is a dimensionless quantity (F(r) has a dimension $1/m^2$). The calculations of the W(i) are described in Section 2.1.2.

The average heat source density in the ith annulus is given by:

$$S(i) = Q\,\frac{W(i+1)-W(i)}{\pi[\, r(i+1)^2 - r(i)^2]}, \quad i=1,2,\ldots N \tag{2.1-5}$$

and the total linear generated within r = r(i) is

$$C(i) = C(R_i) + QW(i) \quad i = 1,\ldots,N+1 \tag{2.1-6}$$

Locally, at location r within the annuli

$$C(r) = -2\pi r k(T)\frac{dT}{dr} \tag{2.1-7}$$

Assuming that the heat source density is uniform within the annulus we have

$$C(r) = C(i)+S(i)\pi\,[\, r^2 - r(i)^2] \tag{2.1-8}$$

Combining Equations (2.1-7) and (2.1-8) and integrating within the interval $r(i) < r < r(i+1)$ yields:

$$-\int_{T(i)}^{T(i+1)} k(T)dT = \frac{1}{2\pi}\left\{\left[C(i) - \pi S(i) r(i)^2\right]\ln\frac{r(i+1)}{r(i)} + S(i)\pi\frac{r(i+1)^2 - r(i)^2}{2}\right\} \tag{2.1-9}$$

The left hand side of Equation (2.1-9) is solved by the Simpson integration method using two subintervals, namely:

$$\int_{T(i)}^{T(i+1)} k(T)dT = \frac{T(i+1)-T(i)}{2}\frac{1}{3}\left[k[T(i)] + 4\,k[T(m)] + k[T(i+1)]\right] \qquad (2.1\text{-}10)$$

where T(m) = [T(i) + T(i+1)]/2.

After some algebra it can be shown that:

$$T(i) = T(i+1) + \frac{6\,Q\,A(i)}{k[T(i)] + 4k[T(m)] + k[T(i+1)]} \qquad (2.1\text{-}11)$$

where,

$$A(i) = \frac{1}{2\pi}\left[\frac{W(i+1)-W(i+1)a^2}{1-a^2}\ln\frac{1}{a} + \frac{W(i+1)-W(i)}{2}\right] \qquad (2.1\text{-}12)$$

with,

$$a = \frac{r(i)}{r(i+1)}$$

It can be noticed that coefficient A(i) depends only on W(i)'s and r(i)'s which are discretized radial power distribution and radii. The W(i)'s can be precomputed and used as long as a new power distribution is not introduced.

In STAV6.2, Equation (2.1-11) is solved iteratively for T(i) in the ith annulus, from T(i+1).

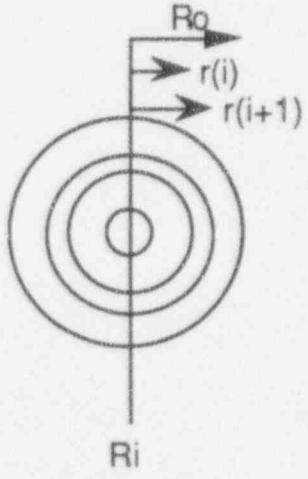

Figure 2.1-1 Energy generated within $R_i \le r \le r(i)$ by W(i) and within $r(i) \le r \le r(i+1)$ by S(i).

2.1.2 Heat Generated in the Pellet

2.1.2.1 General

The heat generated within the fuel pellet is calculated by integrating the radial power distribution through the pellet.

First we define a function G(r) by

$$G(r) = \int_{R_i}^{r} f(r) r dr \qquad (2.1\text{-}13)$$

By virtue of Equations (2.1-2) and (2.1-4), Equation (2.1-13) can be written as

$$W(r_i) = \frac{G(r_i)}{G(R_0)} \qquad (2.1\text{-}14)$$

Then the computer code can compute all $G(r_i)$ from i = 1 to N+1 and division by $G(R_0) = G\,[r(N+1)]$ to yield each $W(r_i)$.

In a simple example, the Bessel form of f(r) from solution of the diffusion equation in cyclindrical coordinates (see Equations (2.1-17) and (2.1-18)), is

$$f(r) = I_0(\kappa r) + \frac{I_1(\kappa R_i)}{K_1(\kappa R_i)} K_0(\kappa r) \qquad (2.1\text{-}15)$$

where $I_n(x)$, and $K_n(x)$ are the modified Bessel functions of first and second kind respectively, and $\kappa = 1/L$ is the inverse diffusion length of neutron in the pellet.

Substituting Equation (2.1-15) into (2.1-13) after some algebra gives:

$$G(r) = \frac{r}{k}\left[I_1(\kappa r) - \frac{I_1(\kappa R_i)}{K_1(\kappa R_i)} K_1(\kappa r) \right] \qquad (2.1\text{-}16)$$

In STAV6.2, a more exact, burnup dependent calculation of the radial power distribution in the pellet is performed. A diffusion calculation is done for UO_2 pellets and a transport theory calculation is performed for UO_2-Gd_2O_3.

2.1.2.2 UO_2 Burnup Dependent Radial Power Profile

The burnup dependence of the radial power profile in a thermal reactor fuel rod is a complicated function of fuel rod design parameters (for example, pellet radius and initial fuel enrichment) and reactor operating conditions. A subroutine (RADAR) based on the work of Palmer, Hesketh, and Jackson, Reference 2-2, has been coded in STAV6.2. The details of this model are provided by Reference 2-2 and summarized below.

The pellet is divided into a number of concentric annuli which coincide with the annuli for the radial temperature calculations. Starting with a given enrichment of U-235 per annulus and zero Pu-238 concentration, the depletion of U-235 and buildup of plutonium is followed in prescribed burnup steps per annulus. The buildup of Pu is obtained by adding to the smooth Pu distribution, the contribution of resonance absorption in U-238 which is distributed among annuli by means of a simple exponential correlation.

Depletion of U-235 and Pu-239 is followed in each annulus using simple correlations, fit to the local flux distribution and total prescribed burnup step. The local flux distribution has a Bessel function shape calculated for an inverse diffusion length of neutron, $\kappa = 1/L$. It is obtained by spatially weighting κ over the number of annuli.

The neutron thermal flux profile, ϕ, is the solution of the 1-group diffusion equation

$$\Delta \phi - \kappa^2 \phi = 0 \qquad (2.1\text{-}17)$$

with the boundary condition

$$\frac{d\phi}{dr} = 0 \quad \text{at } r = R_i, \qquad (2.1\text{-}18)$$

that is zero neutron current at the pellet inner radius.

The solutions are written in terms of modified Bessel functions I and K and take on different forms depending on if the pellet is solid or hollow:

For solid pellet

$$\phi = I_0(\kappa r) \quad 0 \le r \le R_o \qquad (2.1\text{-}19)$$

For hollow pellet

$$\phi = 1 \qquad 0 \le r \le R_i$$

and

$$\phi = I_0(\kappa r) + \frac{I_1(\kappa R_o)}{K_1(\kappa R_o)} K_0(\kappa r) \qquad R_i \le r \le R_o \tag{2.1-20}$$

where R_i and R_o are the inner and outer fuel pellet radii respectively.

The quantity that is calculated is the relative fission reaction rate which is obtained as the product of the Bessel type overall flux distribution and the local sum of macroscopic fission cross sections of U-235 and Pu-239. The fission rate per annulus is assumed to be proportional to the local power distribution. The radial power distribution follows the thermal flux distribution, $f(r) = \Sigma_f \phi(r)$ where Σ_f is the macroscopic fission cross section.

2.1.2.3 UO_2-Gd_2O_3 Burnup Dependent Radial Power Profile

For burnable absorber fuel (gadolinia mixed with urania) the physical situation is different. Because of high absorption cross section of Gd-155 and Gd-157, the burnable absorber fuel burns out practically from its surface, that is the fuel interior is completely shielded from thermal neutrons. There will be a gradual shift with time of the interface between burned and unburned gadolinium, moving from the pin's surface toward the center. This phenomenon has been studied extensively by ABB. A model has been developed and implemented in STAV6.2; it is denoted as the BURAS module. BURAS calculates using transport theory the burnup dependent radial power distribution for UO_2-Gd_2O_3. Details of the model are given Appendix B and also in Reference 2-3.

2.1.3 Pellet Densification and Swelling

2.1.3.1 Introduction

The volume change of UO_2 fuel is the sum of the volume changes due to thermal expansion and changes due to densification and swelling.

The swelling is defined as the increase in fuel volume caused by the replacement of uranium atoms by fission products in the fuel. However, due to the porous structure of ceramic nuclear fuel, the crystal lattice accommodates a sizeable amount of fission products during irradiation without a significant deformation of the pellet.

The swelling is to be distinguished from the total volume changes during irradiation of the fuel which includes also fuel densification,

as a volume decreasing mechanism, as well as fuel relocation and crack formation and healing as volume increasing mechanism. The total fuel volume change can either be positive or negative, however, the swelling is always positive.

The swelling mechanism can be subdivided into two parts: swelling due to solid fission products, and swelling caused by gaseous and volatile fission products such as cesium which can be in a liquidus state at operating fuel temperatures. The latter two at fuel temperatures above 1000°C diffuse to the grain boundaries and form into bubbles. These bubbles can dominate the swelling behavior of fuel at high temperatures and burnups, and their interlinkage leads to fission gas release.

The total fuel swelling consists of accumulated contributions of types of swelling and densification, i.e.,

$$(\Delta V/V)_{total} = (\Delta V/V)_{solid} + (\Delta V/V)_D + (\Delta V/V)_A + (\Delta V/V)_G \qquad (2.1\text{-}21)$$

where $(\Delta V/V)$ designates fraction of change in fuel volume, and the subscripts total, solid, D, A, and G, denote the contributions of the total swelling, solid swelling, densification, swelling accommodation, and gaseous swelling respectively.

2.1.3.2 The Model

[Proprietary Information Deleted]

[Proprietary Information Deleted]

[Figure 2.1-2 Proprietary Information Deleted]

2.1.4 Pellet Relocation Model

An increase in fuel rod power produces cracks in the pellets due to thermal stress induced by the radial temperature gradients across the fuel pellet. The void volume developed by these cracks inside the pellet is accommodated by the pellet-cladding gap volume. This gap size reduction, or alternatively, the increase in apparent pellet diameter due to pellet cracking is referred to as pellet relocation.

[Proprietary Information Deleted]

[Proprietary Information Deleted]

[Figure 2.1-3 Proprietary Information Deleted]

[Proprietary Information Deleted]

2.1.5 Fission Product Gas Release

The nuclear fission process produces the inert gases xenon and krypton at a rate of about 0.3 gas atoms per fissioned uranium. One part of this fission gas is retained in the fuel pellet. The other part is released from the fuel pellet and gives rise to gas pressure buildup in the fuel rod.

The fission gas release model in STAV6.2 consists of two parts: an athermal release model and a thermal release model. The athermal release model accounts the contribution of the release caused by knock-out process from regions close to surfaces of pellet periphery and internal cracks. [Proprietary Information Deleted] The model for thermal release is a physically based model which takes into account a number of processes in the fuel and the amount of gas released. The processes include fission gas migration in UO_2 grains, irradiation induced resolution, and grain boundary saturation.

2.1.5.1 Fission Yield of Xenon and Krypton

The fission yield of an atom is defined to be the number of atoms produced per fission. The isotopes produced directly from fission are radioactive and generally short-lived, and thus are transmuted to other elements.

The fission gas release products are predominated by the fission yield of xenon and krypton. The yield of Xe varies mainly with the fission rate since Xe-136 is produced directly by fission and by neutron capture in the unstable fission product Xe-135. In Figure 2.1-4 the Xe yield (atoms Xe/fissions) versus linear power density is plotted. The correlation is an exponential fit of the yield values obtained by Danielsson (Reference 2-6), at 20 MWd/kgU.

The Xe yield is somewhat higher for Pu-239 than for U-235, [Proprietary Information Deleted]

[Proprietary Information Deleted]

[Figure 2.1-4 Proprietary Information Deleted]

[Proprietary Information Deleted]

[Figure 2.1-5 Proprietary Information Deleted]

2.1.5.2 Thermal Fission Gas Release Model

Basic Equations

The thermal fission gas release model assumes that UO_2 fuel material consists of spherical grains of equal size. The fission product gases produced in a grain at a generation rate β migrate toward the grain boundary by free diffusion. The intragranular gas bubbles act as static traps where they modify the gas atom diffusion coefficient D(t). The gas atoms reaching the grain boundary are precipitated into the intergranular bubbles where their areal density at time t is designated by N(t). The gas atoms are assumed to resolve into the grain matrix with a probability b(t) per unit time within a distance λ from the grain boundary. Figure 2.1-6 shows a schematic two-dimensional representation of fission gas diffusion, resolution, and grain boundary saturation in grains of nuclear fuel.

The diffusion equation for concentration of gas atoms within a grain of radius **a** is written as

$$\frac{\partial C(r,t)}{\partial t} = D(t)\,\Delta_r\,C(r,t) + \beta(t)) \qquad (2.1\text{-}27)$$

with

$$\Delta_r = \frac{\partial^2}{\partial r^2} + \frac{2}{r}\,\frac{\partial}{\partial r}$$

subject to

$$C(r, 0) = 0$$

$$C(\mathbf{a}, t) = b(t)\,\lambda\,N(t) / 2\,D(t) \qquad (2.1\text{-}28)$$

where th boundary condition incorporates the effect of both grain boundary precipitation of gas atoms and re-solution (Reference 2-7). Note that the gas atom diffusion coefficient, D(t), is actually correlated to temperature, T, which is a changes with time, t.

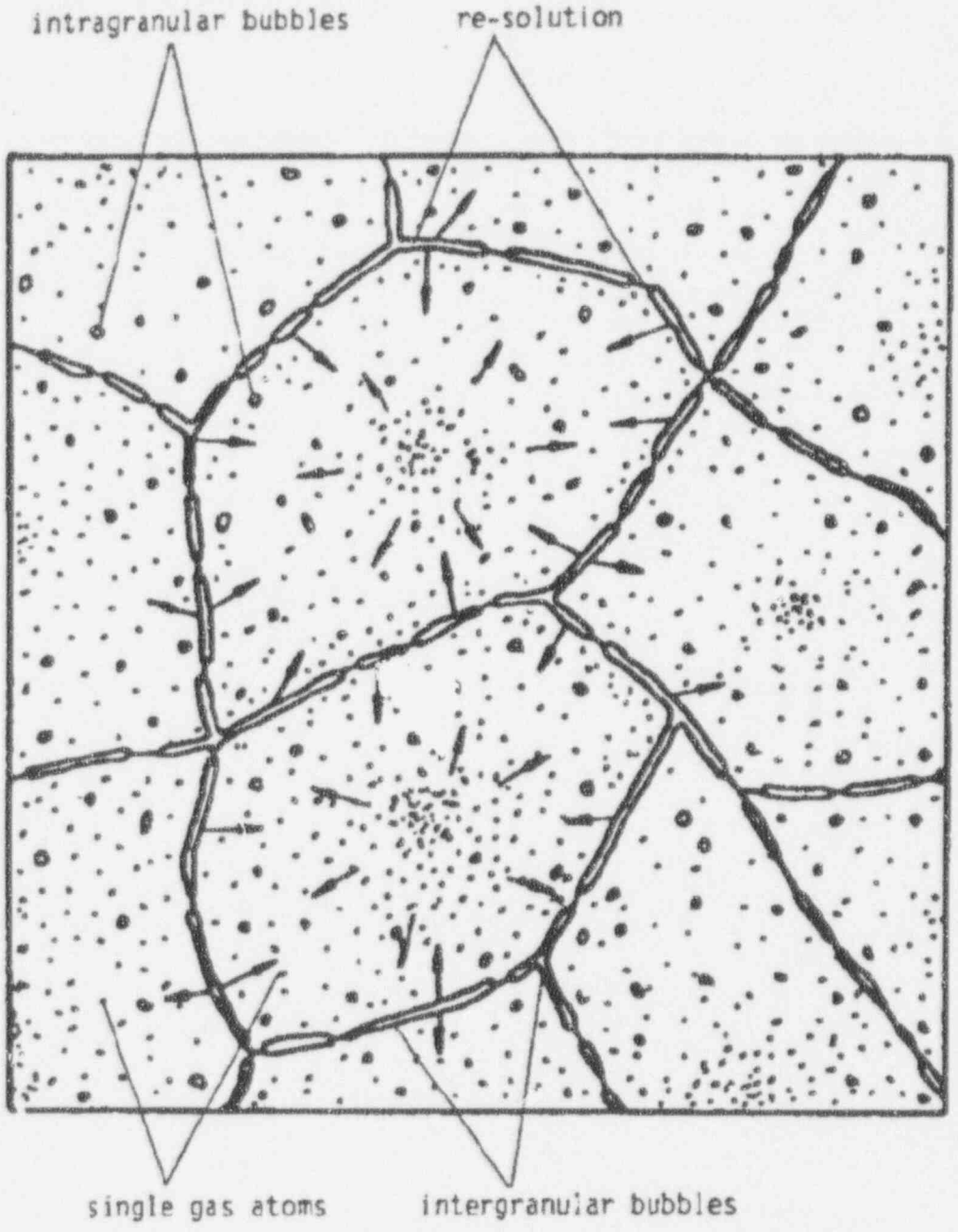

Figure 2.1-6 Two dimensional schematic of nuclear fuel grains and boundaries.

It has been shown in Reference 2-8 that Equations (2.1-27) and (2.1-28) can be transformed to the following expression:

$$N(\tau) = 2 \int_0^{\tau} K(\tau-\tau_0)\left[\beta_e(\tau_0) - \frac{1}{2} \frac{\partial}{\partial \tau_0} \{h_1(\tau_0) N(\tau_0)\} \right] d\tau_0 \qquad (2.1\text{-}29)$$

where

$$\tau = \int_0^t D(t_0)\, dt_0 \qquad (2.1\text{-}30)$$

$$\beta_e = \beta(\tau) / D(\tau) \qquad (2.1\text{-}31)$$

$$h_1 = b(\tau)\lambda / D(\tau) \qquad (2.1\text{-}32)$$

and

$$K(\tau) = \frac{a}{3} - \frac{2a}{\pi^2} \sum_{n=1}^{\infty} \frac{e^{-n^2\pi^2\tau/a^2}}{n^2} \qquad (2.1\text{-}33)$$

The integral Equation (2.1-29) is the basic equation which can be used to calculate the time dependence of the gas particle density on the grain boundary prior to release.

Fission Gas Equation of State and Diffusion Coefficient

The gas arriving at grain boundaries with a given rate will eventually saturate the boundaries through a network of interconnected bubbles. If the ideal gas equation of state is assumed, the density of the intergranular gas at saturation is given by:

$$N_s = \frac{4\, r\, f(\theta)\, f_b}{3\, k\, T \sin^2\theta} \left(\frac{2\gamma}{r} + P_{ext} \right) \qquad (2.1\text{-}34)$$

where $f(\theta) = 1 - \frac{3}{2}\cos\theta + \frac{1}{2}\cos^3\theta$,

r is the radius of the bubble and γ its surface tension, T the temperature, P_{ext} an external pressure, k the Boltzmann constant; $f(\theta)$ takes into account the nonsphericality of the bubbles on grain boundaries, where θ is half the dihedral angle (for UO_2 $\theta = 50°$); and

f_b is the fractional coverage of grain boundary at saturation (Reference 2-9). The release is assumed to occur when the ratio $\varphi(t) = N(t)/N_S$ (fractional saturation) is equal to unity.

The diffusion coefficient for gas atoms in UO_2 grain is based on the data provided in Reference 2-9 where an Arrhenius fit to that data gives:

$$D = 1.09 \times 10^{-17} \exp(-6614/T) \quad T > 1650 \text{ K} \qquad (2.1\text{-}35a)$$

$$D = 2.14 \times 10^{-13} \exp(-22884/T) \quad 1381 < T < 1650 \text{ K} \qquad (2.1\text{-}35b)$$

$$D = 1.51 \times 10^{-17} \exp(-9508/T) \quad T < 1381 \text{ K} \qquad (2.1\text{-}35c)$$

where D is in m^2/s and T the temperature in K.

In Figure 2.1-7, Equations (2.1-35) are plotted as a function of temperature.

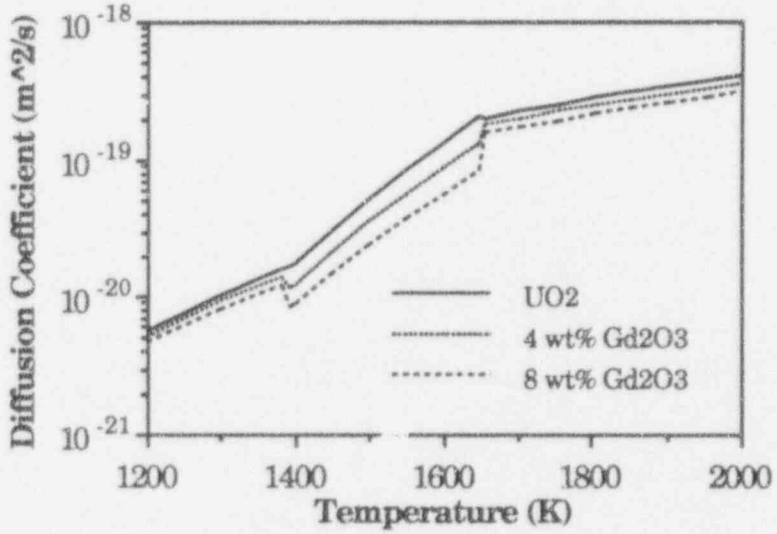

Figure 2.1-7 Effective fission gas diffusion coefficient in UO_2 and $(U,Gd)O_2$ fuel as a function of temperature.

For gadolinia fuel, a model which assumes a decrease in the diffusion coefficient with an increase in gadolinia concentration is used (see Figure 2.1-7). Introduction of gadolinia into urania produces oxygen vacancies which act as fission gas atom traps, thereby lowering the effective diffusion coefficient of gas atoms in the fuel (see References 2-3 and 2-10).

Saturation and Release

For a case of time varying power history, Equation (2.1-29) can be applied to obtain the time evolution of gas atoms within grain boundaries. The gas areal density within grain boundaries can be transformed to volume density, G_B, for a spherical grain, that is:

$$G_B(t) = 3\,N(t) / 2a \qquad (2.1\text{-}36)$$

Assuming that the ratio $b(t)/\beta(t)$ is time independent, since both are proportional to the fission rate, the integral equation can be written in terms of G_B as

$$G_B(\tau) = \frac{3}{a} \int_0^{\tau} K(\tau - \tau_0)\, q(\tau_0)\, d\tau_0 \qquad (2.1\text{-}37)$$

where

$$q(\tau) = \beta_e(\tau) - \frac{ab\lambda}{3\beta} \frac{\partial}{\partial\tau} [\beta_e(\tau)\, G_B(\tau)] \qquad (2.1\text{-}38)$$

Similarly, the number of gas atoms per unit volume of fuel within the grain, G_0, is

$$G_0(\tau) = \int_0^{\tau} [1 - \frac{3}{a} K(\tau - \tau_0)]\; q(\tau_0)\, d\tau_0 \qquad (2.1\text{-}39)$$

Combining (11) to (12):

$$G_0(\tau) + [1 + h_4\beta_e(\tau)]\, G_B(\tau) = \int_0^{\tau} \beta_e(\tau_0)\, d\tau_0 \qquad (2.1\text{-}40)$$

with

$$h_4 = \frac{ab\lambda}{3\beta} \qquad (2.1\text{-}41)$$

Equation (2.1-40) may be interpreted as a conservation of gas atoms within the fuel, i.e., the total number of gas particles generated on the right-hand-side of Equation (2.1-40), is equal to the number of gas atoms in the grain and on the grain boundary, the left-hand-side of Equation (2.1-40).

A numerical approximation is employed (References 2-8 and 2-11), to write

$$1 - \frac{3}{a} K(\tau) \approx \sum_{n=1}^{3} A_n \exp\left(-\frac{Bn}{a^2} \tau\right)$$

where,

$A_1 = 0.63003$ $B_1 = 9.9904$

$A_2 = 0.20651$ $B_2 = 64.488$

$A_3 = 0.14776$ $B_3 = 511.61$ (2.1-42)

Applying (2.1-37) through (2.1-40), the density of gas atoms within grain boundaries $G_B(\tau)$ and within grain, G_{grain}, where

$$G_{grain} = G_0 + h_4 \beta_e G_B , \quad (2.1\text{-}43)$$

are obtained. The last term in Equation (2.1-43) gives the contribution of gas atoms due to re-solution effect which is in equilibrium with the intergranular gas.

In References 2-8 the details of the algorithm for calculating G_B and G_0 as a function of time are sketched. Fission gas release is assumed to occur upon the saturation of grain boundaries. The density of gas within grain boundaries at saturation is

$$G_S = \frac{3}{2a} N_S \quad (2.1\text{-}44)$$

where N_S can be determined from the equation of state, Equation 2.1-34. When $G_B(\tau) \geq G_S$ the amount of gas released per unit volume, F_R, may be written

$$F_R = h_5 G_S \quad (2.1\text{-}45)$$

where $0 < h_5 \leq 1$, and h_5's upper bound corresponds to the condition that all the accumulated gas at grain boundaries would be released upon saturation. When saturation occurs, instead of frequent discrete gas-releases, a continuous gas release is assumed. At the instant of release the intergranular gas concentration is lowered to $(1-h_5)\, G_S + h_S G_S^{eq}$ which is the amount of intergranular gas in equilibrium with the intragranular gas at saturation. The gas that is thereby "left over" is released. The quantity G_0 which determines the

intragranular amount of gas not in equilibrium with intergranular gas, is correspondingly adjusted in order to preserve the total amount of gas.

2.1.5.3 Athermal Fission Gas Release Model

The athermal or low temperature fission gas release is caused by knock-out and recoil processes in nuclear fuel during fissioning and so is fission rate dependent but not temperature dependent. [Proprietary Information Deleted]

[Proprietary Information Deleted]

Athermal Release Correlation BWR

The BWR athermal release correlation is obtained by an exponential fitting of the data obtained from fuel rods irradiated in ABB Atom built BWRs and some U.S. BWR data. [Proprietary Information Deleted]

[Proprietary Information Deleted]

For the sake of comparison, the low temperature release correlation of ANS-5.4 model (Reference 2-13), is also stated here:

$$F = 8.5 \times 10^{-5} E \qquad (2.1\text{-}48)$$

For example, at E=40 MWd/kgU the release faction F is 0.34%. In Figure 2.1-8 the ANS-5.4 correlation is compared graphically with STAV6.2 model for BWR low temperature fission gas release.

[Proprietary Information Deleted]

Figure 2.1-8 BWR athermal fission gas release as a function of burnup predicted by the STAV6.2 correlations. The correlations are based on fit of measured in-reactor data.

PWR Athermal Release Correlation

The STAV6.2 PWR athermal release correlation is also presented for completeness. An [Proprietary Information Deleted] In Figure 2.1-9 we have plotted the best-estimate and upper bound athermal release versus rod burnup.

[Proprietary Information Deleted]

Figure 2.1-9 PWR athermal fission gas release as a function of burnup predicted by the STAV6.2

2.1.6 Helium Release

Helium is produced during irradiation of UO_2 fuel. The primary sources of helium are:

(1) alpha-decay of transuranic elements, mainly ^{242}Cm

(2) ternary fission

(3) $^{16}O(n,\alpha)^{13}C$ reaction

Ternary fission has a yield of 0.2 to 0.3% helium atoms per fission. The transuranic chain is illustrated in Figure 2.1-10. All of the elements in this chain decay by alpha process except ^{239}Np and ^{242}Am. However, most of the elements have long decay lives, that is about 90% of the helium generation from transuranic chain come from ^{242}Cm which has a half life of 163 days. In LWR fuel at the present design end-of-life burnup (≈ 50 MWd/kgU) this process contributes to about 0.3% helium atom per equivalent fission. Finally $^{16}O(n,\alpha)^{13}C$ reaction contributes up to 0.6% helium atom per equivalent fission. Summing these contributions will give 1.2% helium atom per equivalent fission. Compare this value with the krypton fission yield which is 3%.

[Proprietary Information Deleted]

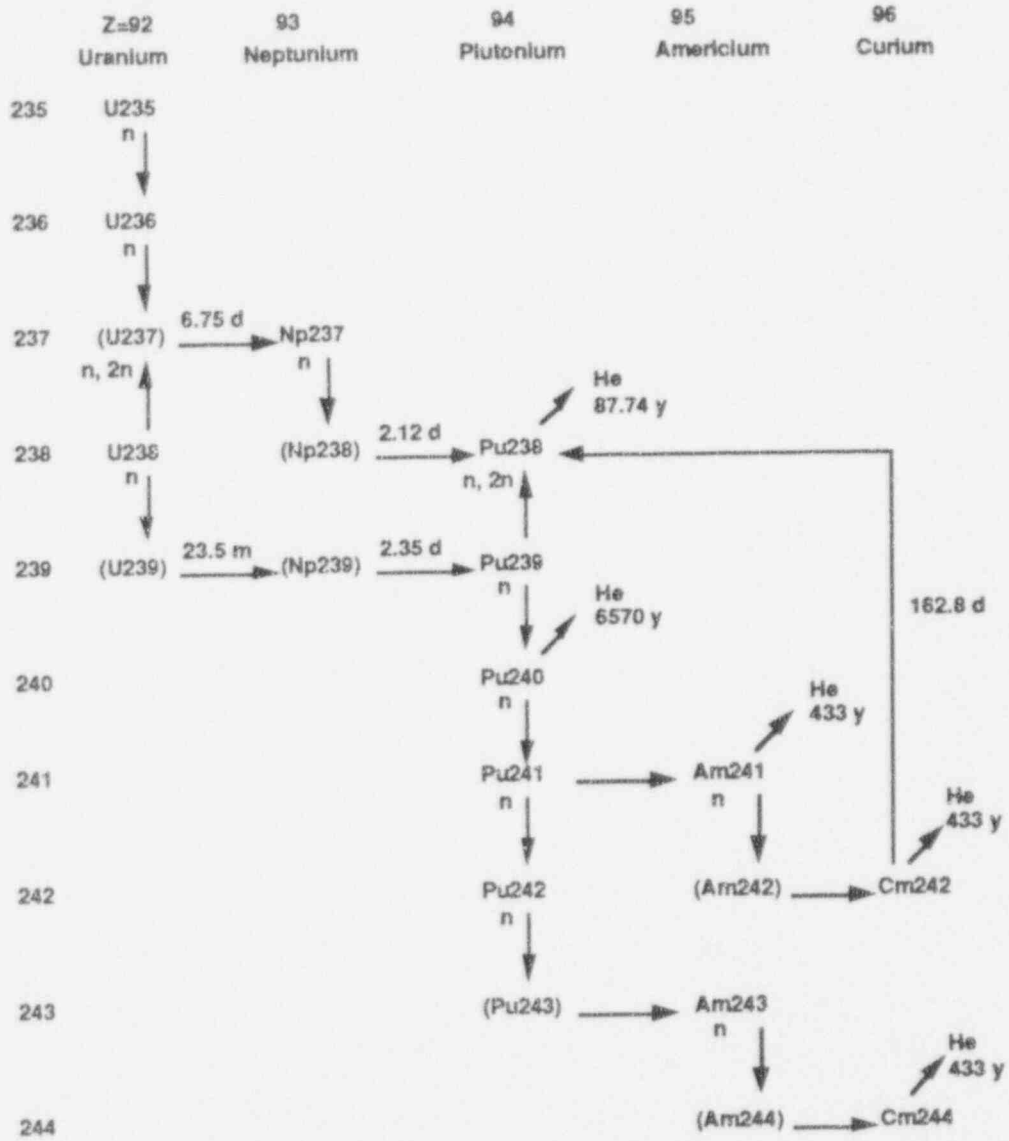

Figure 2.1-10 Chains of Actinides and Helium Production

2.2 Fuel Rod Cladding Models

The cladding is made of Zircaloy and is treated as a long, thin tube. The material is considered to be isotropic except for the thermal expansion which is taken to be different in the radial and axial direction. The cladding temperature model includes thermal conductivity and specific heat. The cladding deformation models include: thermal exparsion, elasticity and plasticity, creep, growth, and corrosion.

2.2.1 Cladding Temperature Distribution

The cladding outer surface temperature for any axial segment of the rod is determined by the rod power, the coolant thermodynamics, and the cladding oxide thickness as a function of burnup or time. The cladding inner surface temperature is then calculated by assuming steady state heat conduction, with a uniform heat generation, through the cladding wall.

The steady state heat conduction equation in a axisymmetric infinite hollow cylinder, neglecting internal heat generation, is given by the Poisson equation:

$$\nabla \bullet [\lambda(T)\nabla T] = 0 \qquad (2.2\text{-}1)$$

subject to the boundary condition at the cladding inner surface:

$$q = -\lambda \frac{dT}{dr} \qquad (2.2\text{-}2)$$

where T is the temperature, λ the thermal conductivity of Zircaloy cladding, q the heat flux at the cladding inner surface, r the radius, and:

$$\nabla \bullet = \frac{1}{r}\frac{d}{dr}r$$

$$\nabla = \frac{d}{dr}$$

are the divergence and the gradient operators in axisymmetric cylindrical coordinates respectively.

Integration of Equation (2.2-1) subject to the condition of Equation (2.2-2), gives:

$$r\,\lambda(T)\frac{dT}{dr} + \frac{Q}{2\pi} = 0 \qquad (2.2\text{-}3)$$

where Q is the fuel pellet linear power density (W/m).

Rewriting Equation (2.2-3) yields:

$$\int_{T_o}^{T_i} \lambda(T)dT = -\int_{r_o}^{r_i} \frac{Q}{2\pi r}\,dr \qquad (2.2\text{-}4)$$

where subscripts i and o denote the inner and the outer cladding surface respectively. Equation (2.2-4) can be solved exactly if the cladding thermal conductivity is specified. We assume the cladding conductivity is a linear function of temperature:

$$\lambda = a + b\,T \tag{2.2-5}$$

where a and b are constants (Appendix A, Section A.2). Inserting Equation (2.2-5) into (2.2-4) and integrating gives:

$$a(T_i - T_o) + \frac{b}{2}(T_i^2 - T_o^2) = \frac{Q}{2\pi} \ln\left(\frac{r_o}{r_i}\right) \tag{2.2-6}$$

The quadratic equation (2.2-6) can be solved to give the cladding inner surface temperature:

$$T_i = \frac{1}{b}\left[\sqrt{(a+bT_o)^2 + \frac{bQ}{\pi} \ln\left(\frac{r_o}{r_i}\right)} - a\right] \tag{2.2-7}$$

Equation (2.2-7) is coded in STAV6.2. It should be noted that in our calculation, Q only includes the amount of heat generated in the fuel pellet. The heat generated in the cladding which gives a negligible contribution to the cladding temperature is ignored.

2.2.2 Mechanical Calculations

In this section the cladding mechanical model of STAV6.2 is presented. The model considers the pellet-cladding mechanical interaction and calculates the cladding deformations due to elastic, creep, and plastic deformations. The stress-strain analysis is performed by utilizing the classical elastoplasticity relations for a hollow cylinder (Reference 2-14).

For the analysis of deformations two physical circumstances are envisaged. The first situation is that the fuel and the cladding are not in contact (the open gap regime) and the second situation is when the fuel and the cladding are in contact (the closed gap regime).

For the pellet-cladding interaction, we use the method of successive elastic solution (MSES). In this method, the cladding strain plastic and creep components are incremented and then successively updated to obtain the accumulated permanent strain. This is done by breaking the loading path to a number of small increments where for each increment of the loading the solution of all plasticity equations are obtained.

2.2.2.1 Model Basic Assumptions

The fuel rod is considered to be a cylindrically symmetric system, comprising of an inner cylinder being the nuclear fuel (the pellet) enclosed in a metallic tube (the cladding) with sealed ends and a space (pellet-to-cladding gap plus plenum) for fuel expansion and accommodation of released fission gases.

The loads exerted on the cladding are as follows:

- External coolant pressure
- Internal gas pressure
- Stresses caused by temperature gradients
- Axial forces resulting from these pressures
- Internal pellet-cladding contact pressure
- Axial force caused by fuel expansion

The deformation analysis in this model assumes that the fuel rod keeps its cylindrical shape with the following deformation effects:

- Fuel thermal expansion, densification, swelling and relocation,
- Cladding thermal expansion, creep, and plasticity.

Also it is assumed that:

- Cladding stresses and strains are axisymmetric
- There is no shear strain
- Thin shell model for the cladding with zero radial stress component is applicable

2.2.2.2 Model Fundamental Equations

STAV6.2 calculates, for each axial segment of the cladding, the stresses and the strains. The strain components in the axisymmetric cylinder are expressed by the *compatibility* relations:

$$\varepsilon_1 = \frac{du}{dr} \qquad (2.2\text{-}8)$$

$$\varepsilon_2 = \frac{u}{r} \tag{2.2-9}$$

$$\varepsilon_3 = \frac{dw}{dz} \tag{2.2-10}$$

where ε_1, ε_2, and ε_3 are the strains in radial, tangential, and axial directions, u and w are the radial and the axial displacements respectively.

The relation between the stresses and strains are expressed by:

$$\sigma = [\mathbf{C}]\,\mathbf{e} \tag{2.2-11}$$

where **e** is the elastic strain vector expressed by

$$e = \varepsilon - \varepsilon_0 \tag{2.2-12}$$

with

$$\varepsilon = (\varepsilon_1, \varepsilon_2, \varepsilon_3), \tag{2.2-13}$$

$$\varepsilon_0 = \varepsilon_p + \varepsilon_c + \alpha_T \tag{2.2-14}$$

is the sum of plastic, creep, and thermal strain vectors, while

$$[\mathbf{C}] = \frac{E}{(1+\nu)(1-2\nu)} \begin{pmatrix} 1-\nu & \nu & \nu \\ \nu & 1-\nu & \nu \\ \nu & \nu & 1-\nu \end{pmatrix} \tag{2.2-15}$$

is the matrix relating elastic strains to stresses with E and ν denoting Young's modulus and Poisson's ratio respectively.

The elastic stress components are determined by Hook's law where the elasticity constants are assumed to be isotropic.

The plastic strain component increments, assuming the von Mises yielding criterion, are calculated by the Prandtl-Reuss flow relations:

$$\delta\varepsilon_p = \beta\,\mathbf{S} \tag{2.2-16}$$

where,

$$\mathbf{S} = \sigma - \mathbf{I}\,\sigma_m \tag{2.2-17}$$

are the deviatoric stress components, and $\sigma_m = (\sigma_1+\sigma_2+\sigma_3)/3$, is the hydrostatic stress, **I**, the unit vector and

$$ß = \frac{3}{2}\frac{\delta\varepsilon_{ep}}{\sigma_e} \tag{2.2-18}$$

is the Prandtl-Reuss multiplier with $\delta\varepsilon_{ep}$, and σ_e denoting the so-called effective plastic strain increment and the effective stress respectively. They are expressed as:

$$\delta\varepsilon_{ep} = \sqrt{\frac{2}{3}}\,|\delta\varepsilon_p| \tag{2.2-19}$$

$$\sigma_e = \sqrt{\frac{3}{2}}\,|S| \tag{2.2-20}$$

with a notation that $|v| = (v_1^2 + v_2^2 + v_3^2)^{1/2}$ is the magnitude of the vector **v**.

Equations (2.2-19) and (2.2-20) have been derived by assuming that the plastic deformation is volume-conserving, meaning that, $\sum \delta\varepsilon_{pi} = 0$ and the von Mises yield criterion which states that yielding takes place when σ_e equals the yield strength, σ_y. It is noted that the effective plastic stress and strain should satisfy the equation:

$$\sigma_e = f(\sigma_e/E + \varepsilon_{ep}) \tag{2.2-21}$$

where f denotes the post-yield part of the stress-strain relation, obtained from the uniaxial tension test.

Note that the expressions for effective strain and stress, Equations (2.2-19) and (2.2-20) can be written as

$$\varepsilon_{ep} = \frac{\sqrt{2}}{3}\,[(\varepsilon_{ep1}-\varepsilon_{ep2})^2 + (\varepsilon_{ep2}-\varepsilon_{ep3})^2 - (\varepsilon_{ep3}-\varepsilon_{ep1})^2]^{1/2} \tag{2.2-22}$$

and

$$\sigma_e = \frac{\sqrt{2}}{2}\,[(\sigma_1 - \sigma_2)^2 + (\sigma_2-\sigma_3)^2 + (\sigma_3-\sigma_1)^2]^{1/2} \tag{2.2-23}$$

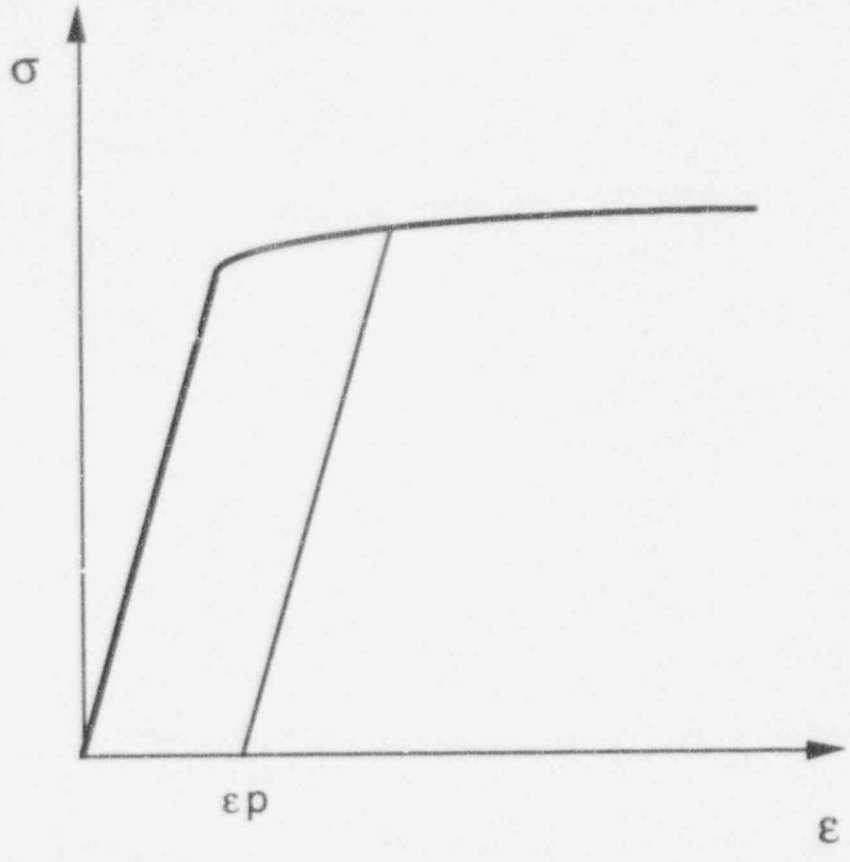

Figure 2.2-1 Isothermal Stress-Strain Curve

For creep deformations Equations (2.2-16) through (2.2-19) are also true, that is, the Prandtl-Reuss flow rule and the conservation of volume are valid. The Prandtl-Reuss equations for creep can be expressed by:

$$\frac{d\varepsilon_c}{dt} = \frac{3}{2\sigma_e}\frac{d\varepsilon_{ec}}{dt}\mathbf{S} \qquad (2.2\text{-}24)$$

where ε_{ec} is the effective creep strain usually described by a phenomenological equation for the creep deformation of a given material, see Appendix A, Section A.3. For the present model what distinguishes creep from plasticity (in macroscopic sense) is that the latter becomes effective when material exceeds the yield point, while the former is active throughout the irradiation and is inherently time dependent.

2.2.2.3 Open Gap Regime

For the open gap modeling we consider a thin cylindrical shell subjected to both internal gas pressure and external coolant pressure. The geometry and the coordinates are shown in Figure 3.4.

For this case, the equilibrium equations are:

$$\sigma_1 = 0 \tag{2.2-25}$$

$$\sigma_2 = \frac{r_i P_i - r_0 P_0}{t} \tag{2.2-26}$$

$$\sigma_3 = \frac{r_i^2 P_i - r_0^2 P_0}{r_0^2 - r_i^2} \tag{2.2-27}$$

where σ_1, σ_2, and σ_3 are the stresses in the radial, circumferential, and the axial direction respectively, and

r_i = inner radius of the cladding

r_0 = outer radius of the cladding

t = $r_0 - r_i$

P_i = fuel rod internal gas pressure

P_0 = coolant pressure

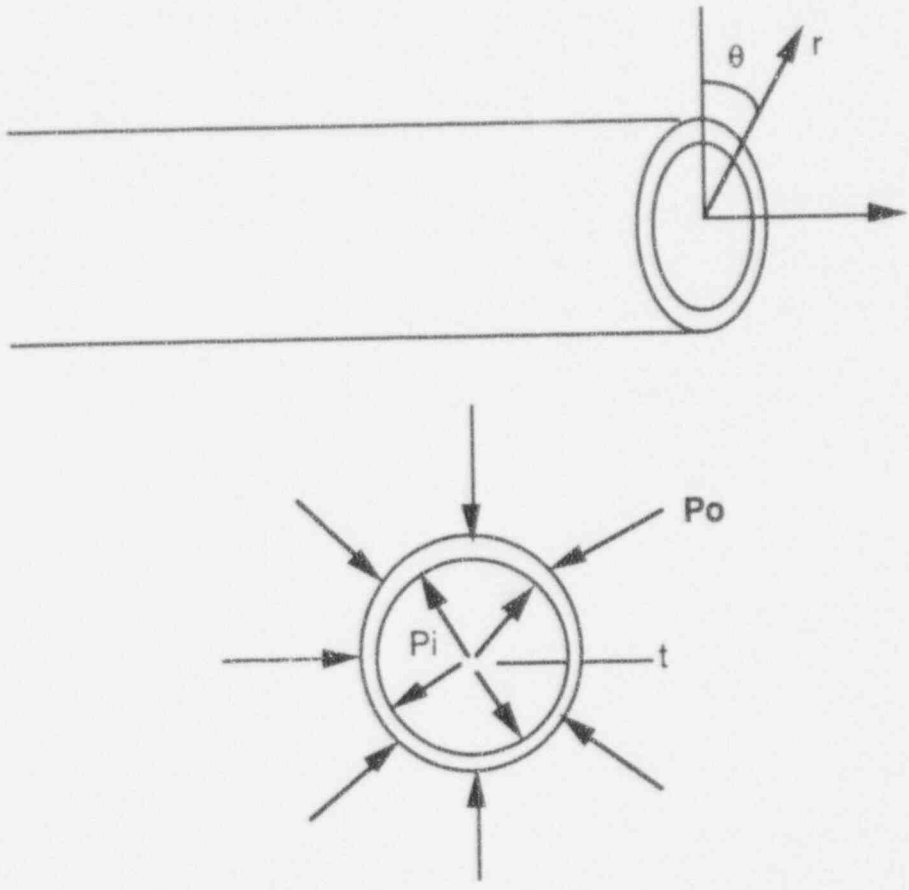

Figure 2.2-2 Geometry of fuel cladding under external and internal pressures.

Substituting Equation (2.2-27) into (2.2-11), a relation between the elastic strain components are found:

$$e_1 = -\frac{\nu}{1-\nu}(e_2 + e_3) \tag{2.2-28}$$

With the aid of Equation (2.2-28) the elastic strain-stress relation, Equation (2.2-11), for a thin wall tube is found:

$$\begin{bmatrix}\sigma_2\\ \sigma_3\end{bmatrix} = \frac{E}{1-\nu^2}\begin{bmatrix}1 & \nu\\ \nu & 1\end{bmatrix}\begin{bmatrix}e_2\\ e_3\end{bmatrix} \tag{2.2-29}$$

or vice versa:

$$\begin{bmatrix}e_2\\ e_3\end{bmatrix} = \frac{1}{E}\begin{bmatrix}1 & -\nu\\ -\nu & 1\end{bmatrix}\begin{bmatrix}\sigma_2\\ \sigma_3\end{bmatrix} \tag{2.2-30}$$

2.2.2.4 Pellet Cladding Mechanical Interaction (PCMI)

Closure of the pellet-clad gap, for example, as a consequence of the expansion of the pellet, would result in a loading of the cladding through which a displacement of the cladding diameter would occur. Calculations for the closed gap regime is carried out using a model of a thin cylindrical shell subject to a given external pressure and a prescribed radial displacement caused by PCMI. Furthermore, upon contact, no-slippage between the pellet and the cladding is assumed.

Thus in the closed gap regime the stresses and strains can be computed by solving the point-elasto-plastic equations subject to the following three boundary conditions:

(1) Upon loading, the inner clad radius, r_i, is increased by a prescribed displacement $u(r_i)$, which is driven by fuel expansion. Thus, the associated hoop strain is given by

$$\varepsilon_2 = \frac{u(r_i)}{r_i} \tag{2.2-31}$$

with

$$u(r) = u(r_i) + (r-r_i)\varepsilon_2 \tag{2.2-32}$$

(2) The thin tube approximation is

$$\sigma_1 = 0 \tag{2.2-33}$$

(3) No-slippage between the cladding and pellet results in:

$$\varepsilon_{3,clad} = \varepsilon_{3,pellet} \tag{2.2-34}$$

where $\varepsilon_{3,pellet}$ is prescribed.

The quantity of interest is the interfacial pellet-cladding contact pressure, P_c, which is derived from Equation (2.2-26) to be

$$P_c = (a-1)\,\sigma_2 + a\,P_0 \tag{2.2-35}$$

where $a = r_0/r_i$.

Note that P_c includes gas pressure and interference loads.

The total cladding strain components during the pellet-cladding contact can be obtained by considering the radial component of the constitutive relation given in Equation (2.2-11) plus the boundary

conditions defined by Equations (2.2-31) through (2.2-33). After some algebra it can be shown that these are:

$$\varepsilon_1 = \frac{-\varepsilon_2(r_i)\nu + a_1 q}{a_1 - \nu} \quad (2.2\text{-}36a)$$

$$\varepsilon_2 = \frac{\varepsilon_2(r_i)(1-\nu) + a_2 q}{a_1 - \nu} \quad (2.2\text{-}36b)$$

$$\varepsilon_3 = \text{given} \quad (2.2\text{-}36c)$$

where,

$$q = (1-2\nu)(\varepsilon_{p1} + \delta\varepsilon_{p1}) - \nu\varepsilon_z + q_T \quad (2.2\text{-}37)$$

$$q_T = (1-2\nu)\,\alpha_{T1} + \nu \sum_{i=0}^{3} \alpha_{Ti} \quad (2.2\text{-}38)$$

$$a_1 = \frac{a+1}{2} \quad (2.2\text{-}39)$$

$$a_2 = \frac{a-1}{2} \quad (2.2\text{-}40)$$

The total strain components given by Equation (2.2-36) can now be used to determine the stress vector, σ, via Equation (2.2-11) and in case of yielding the incremental plastic strain vector, δ_{ep}, and the new yielding stress. The pellet-cladding interfacial pressure is calculated via Equation (2.2-35).

[Proprietary Information Deleted]

2.2.3 Creep Model for Zircaloy

2.2.3.1 General

The overall in-pile Zircaloy creep is predominantly a combination of the following mechanisms: thermal creep, irradiation induced creep, and irradiation enhanced creep.

[Proprietary Information Deleted]

The effective stress and effective strain are given by:

$$\sigma_e = \frac{\sqrt{2}}{2}\left[(\sigma_1-\sigma_2)^2 + (\sigma_2-\sigma_3)^2 + (\sigma_3-\sigma_1)^2 \right]^{1/2} \quad (2.2\text{-}44)$$

and

$$\varepsilon_e = \frac{\sqrt{2}}{3}\left[(\varepsilon_1-\varepsilon_2)^2 + (\varepsilon_2-\varepsilon_3)^2 + (\varepsilon_3-\varepsilon_1)^2 \right]^{1/2} \quad (2.2\text{-}45)$$

where σ_1, σ_2, and σ_3 are the stresses in the radial, circumferential, and axial directions, and similarly, ε_1, ε_2, and ε_3 are the strains in the radial, circumferential, and axial directions.

[Proprietary Information Deleted]

2.2.3.2 ABB Atom Creep Model

[Proprietary Information Deleted]

[Proprietary Information Deleted]

Figure 2.2-3 [Proprietary Information Deleted]

[Proprietary Information Deleted]

[Proprietary Information Deleted]

Figure 2.2-4 [Proprietary Information Deleted]

2.2.3.3 Creep Hardening Rule

Creep data are mostly obtained at constant stress and temperature. The question arises how these data can be applied to the case where load is varying with time. To address this issue several cumulative creep laws (hardening rules) are possible. [Proprietary Information Deleted]

[Proprietary Information Deleted]

[Figure 2.2-5 Proprietary Information Deleted]

[Proprietary Information Deleted]

2.2.4 Fuel Rod Growth

Fuel rod growth in STAV6.2 is an empirical model derived from length change measurements taken on fueled Zircaloy rods

irradiated in Light Water Reactors. The data include the effects of the irradiation growth, cladding creep, and pellet cladding mechanical interaction.

Rod growth is not only a function of macroscopic variables such as stress, temperature, and flux, but also depends on Zircaloy crystallographic texture, dislocation density, grain size, alloying additions and impurities. [Proprietary Information Deleted]

TABLE 2.2-1

Proprietary Information Deleted

[Proprietary Information Deleted]

[Proprietary Information Deleted]

Figure 2.2-6 [Proprietary Information Deleted]

2.2.5 Zircaloy Water-Side Corrosion

2.2.5.1 Introduction

The phenomenon of water-side cladding corrosion is complicated due to various aspects of steam dissociation with a diffusion process across the oxide film towards the metal/oxide interface. The Zircaloy corrosion reaction is essentially a diffusion-controlled reaction, meaning that the velocity with which the reaction proceeds depends on the rate at which the atoms or ions can diffuse through the Zircaloy matrix, Reference 2-16.

Oxygen atoms dissolved into Zircaloy create anion vacancies which in turn allow oxygen diffusion across the oxide film. After a sufficient length of time the metal becomes supersaturated with oxygen and nucleation would occur where an oxide film will form. Once an oxide film has been formed, the oxygen dissolves into the metal and if the rate of transport through the film is faster than the dissolution, supersaturation will occur at the metal/oxide interface, and the oxide film will be formed.

The oxidation process is observed to follow a rate law described by:

$$\Delta w = kt^n \qquad (2.2\text{-}62)$$

where Δw is the oxide weight gain, k the rate constant, t the exposure time, and n the exponent which may vary from 0.3 (cubic) to 0.5 (parabolic) in the first stage of oxidation. During the first stage the oxide layer is black or possess a lustrous appearance. It is very

compact and protective. During the second stage the exponent n is close to 1, that is, the oxidation rate becomes constant in time. At this stage a friable grey oxide covers the Zircaloy material. The change from the first stage to the second stage is called the first transition or break-away in oxidation rate. The precise mechanism for this transition has not yet been well-understood. However, it has been argued that zirconium has a rather high value for the Pilling-Bedworth ratio (the ratio of the molar volumes of ZrO_2 and Zr), about 1.56. As a result, during oxidation of the Zircaloy, the volume change leads to development of compression stresses in the film and the tensile stresses in the metal substrate. When these stresses reach a certain critical value, oxide scale cracks develop which in turn open pathways for the oxidant through the cracks. This leads to a rapid oxidation rate of the alloy.

The process just described can occur in isothermal condition in an autoclave environment. In-reactor corrosion is a more involved process in which heat is flowing across the cladding surface into water that is in turbulent flow past the surface, and a temperature gradient which exists across the thin film of the coolant in contact with the metal. The higher the heat flux, the higher the temperature drop across such a film will be, and thus the higher the temperature of the water in contact with the metal. Thus the thermal and hydraulic modeling should be coupled to oxidation modeling to have a meaningful description of the in-reactor corrosion process.

In addition, it has been found that a second transition in oxidation rate of Zircaloy would occur where the reaction rate k, in Equation (2.2-62), increases after a certain irradiation exposure. It has been argued that the presence of fast neutron flux creates additional defects in the oxide layer which after reaching a certain concentration a new diffusion pathway for oxygen opens up that enhances the oxidation rate.

Cladding corrosion in pressurized water reactors (PWRs) is uniform, whereas in boiling water reactors (BWRs) a nodular type of oxide is formed which gives an effective average oxide layer thickness far above the expected uniform corrosion values.

2.2.5.2 BWR Cladding Corrosion Model

In BWRs clad corrosion is not uniform. Corrosion consists of small nodules scattered within a thin uniform oxide. STAV6.2 includes a number of BWR clad corrosion correlations representing different types of claddings used in different BWRs.

[Proprietary Information Deleted]

TABLE 2.2-2

Proprietary Information Deleted

[Proprietary Information Deleted]

[Proprietary Information Deleted]

Figure 2.2-7 Oxide layer thickness growth as a function of time (effective full power hours) for different cladding materials and environments.

[Proprietary Information Deleted]

[Proprietary Information Deleted]

[Figure 2.2-8 Proprietary Information Deleted]

[Proprietary Information Deleted]

One important quantity in oxidation behavior of Zircaloy is the thermal conductivity of ZrO_2. In the literature, different values of ZrO_2 thermal conductivity have been recommended. For example Maki (Reference 2-17) recommends a value of 4 W/mK for the thermal conductivity of oxide film formed on Zircaloy-2, Kingery et al. (Reference 2-18) data show a value of 2 W/mK at 300°C and other data show that the oxide conductivity depends on oxide structure which is about 0.9 W/mK for nodular oxides, and 4-6 W/mK for other oxide types. [Proprietary Information Deleted]

2.2.5.3 BWR Cladding Crud Deposition Rate

Corrosion products (Crud) released from plant surfaces can deposit on the cladding surface. [Proprietary Information Deleted]

2.2.5.4 PWR Cladding Corrosion

There are a number of oxidation kinetics correlations for Zircaloy based on isothermal experiments. In STAV6.2 for the pre-transition oxidation the Dyce's correlation is considered,

$$\frac{dS}{dt} = \frac{A}{S^2} \exp\left(-Q_1/RT\right) \qquad (2.2\text{-}67)$$

where dS/dt is the corrosion rate, S the oxide layer, T the metal/oxide temperature, R the universal gas constant, and A and Q are constants given in Table 2.2-3.

In PWRs, the heat fluxes affect the metal/oxide temperature. The metal/oxide temperature varies as a function of heat flux, the power history. The temperature change through the oxide layer thickness formed in a given time step in the power history is given by:

$$T = T_0 + f\,(S - S_0) \tag{2.2-68}$$

where $f = \frac{q}{\lambda_{ox}}$, q the heat flux ($W/cm^2$) and λ_{ox} is the oxide thermal λ_{ox}= 2.00 W/mK, S is the current oxide thickness and S_0 is the oxide thickness associated with temperature T_0 in the preceding time step. It can be shown that for the problem under consideration:

$$S = \left[\frac{\Sigma^3 - S_0^3\, ç(\Sigma - S_0)}{1 - ç(\Sigma - S_0)} \right]^{1/3} \tag{2.2-69}$$

where

$$\Sigma = [\, 3(t - t_0)\, A \exp(-Q_1/RT) + S(\,]^{1/3} \tag{2.2-70}$$

and

$$ç = \frac{Q_1 f}{R\, T_0^2} \tag{2.2-71}$$

The first transition is based on the data of Dyce (Reference 2-20) which give the time of transition as a function of temperature and is given by

$$t_t = t_a \exp\left(\frac{Q_a}{RT}\right) \tag{2.2-72}$$

The post-transition model the oxide thickness is assumed to increase linearly with time according

$$\frac{dS}{dt} = C \exp(-Q_2/RT) \tag{2.2-73}$$

where C and Q_2 are constants determined by experiments and are given for the present study in Table 2.2-3. The second transition (in-reactor oxide growth) is modeled by modifying (2.2-73) as follows:

$$\frac{dS}{dt} = C\,[\, 1 + D\,(S - S_c)\,] \exp(-Q_2/RT) \tag{2.2-74}$$

where S_c is the threshold thickness for which the second transition occurs, that is for S<Sc D=0. The variable D is neutron enhancement factor and is assumed to have the following form: $D = u\phi$ where ϕ is the fast neutron flux (>1 MeV) and u is a constant determined by inpile oxide measurements. As can be observed, the enhancement factor is taken to be a linear function of neutron flux. The above relations can be interpreted that a certain oxide thickness is required for the second transition to occur, and the oxide growth is enhanced by both neutron flux and oxide thickness after this transition. The oxide thickness dependence transition phenomenon has been discussed by Johnson (Reference 2-21).

Evaluations of measured data indicate that at long residence times the enhancement in oxidation rate due to neutron flux and oxide thickness levels off. For this reason one can set $E = \text{Min}\,[1 + D\,(S-S_c), E_{max}]$ where the value of E_{max} is adjusted by experimental data.

Equations (2.2-73) and (2.2-74) are solved for every time step of the power history. The analytical solution is given by:

$$S = \xi \quad \frac{e^{F\,G}-1}{G} \tag{2.2-75}$$

where

$$G = \frac{Q_2\,f}{R\,T_0^2} + \frac{D}{1+D\,(S-S_c)} \tag{2.2-76}$$

$$F = C\,[\,1+D\,(S_0-S_c)\,]\,\exp(-Q_2/RT)\,(t-t_0) \tag{2.2-77}$$

The above solutions provide closed form solutions of post-transition oxide layer for a heat flux varying condition without appealing to numerical schemes such as Newton's method for solving the nonlinear equation.

TABLE 2.2-3 CONSTANTS IN OXIDATION CORRELATIONS

Proprietary Information Deleted

2.2.5.5 PWR Cladding Crud Deposition

[Proprietary Information Deleted]

[Proprietary Information Deleted]

Figure 2.2-9 [Proprietary Information Deleted]

2.2.6 Hydrogen Pickup

Hydrogen pickup in Zircaloy cladding emanates from the corrosion reaction and the hydrogen produced by radiolytic decomposition of water in a radiation field.

The corrosion of zirconium-base alloys is generally expressed by the following overall reaction:

$$Zr + 2\,H_2O \rightarrow ZrO_2 + 4\,H \qquad (2.2\text{-}79)$$

and for the absorption of hydrogen into the metal:

$$Zr + H \rightarrow Zr(H)_{SO1} \qquad (2.2\text{-}80)$$

or

$$2\,Zr + 3\,H \rightarrow 2\,ZrH_{1.5} \qquad (2.2\text{-}81)$$

depending on hydrogen concentration and temperature.

where

$Zr(H)_{SO1}$ = solid solution of hydrogen in zirconium.

It has become conventional to describe hydrogen pickup in terms of a fraction of the total quantity of hydrogen released by the corrosion reaction (percent theoretical). The use of the term theoretical pickup fraction is based on the assumption that there is no available source of oxygen and/or hydrogen other than obtained by the corrosion reaction described above. Below we present the correlations used in STAV6.2 to predict cladding hydrogen pickup during reactor service for BWR and PWR fuel rods.

2.2.6.1 BWR Correlation

[Proprietary Information Deleted]

2.2.6.2 PWR Correlation

[Proprietary Information Deleted]

2.2.7 Coolant to Cladding Heat Transfer

STAV6.2 thermal calculations start from the coolant where cladding outer surface is calculated. The heat transfer between the coolant and the cladding will be either single-phase convection, subcooled boiling, or saturated flow boiling.

[Proprietary Information Deleted]

2.2.7.1 **Heat Transfer Model in Pressurized Water Reactors**

Bulk Coolant Temperature

The heat transfer model assumes a closed subchannel in the single-phase forced convection regime and the subcooled boiling (nucleate boiling) regime. The coolant and cladding surface temperature are calculated at the axial midplane of each axial segment of the rod.

Subchannel geometry, coolant inlet temperature, coolant mass flow rate are input to the model. Also, rod power as a function of burnup (or time) at different axial positions is an input to the model. Coolant flow is from the bottom to the the top of the rod. In presence of an oxide layer, the cladding temperature is calculated from the outer surface of the oxide layer.

Bulk coolant temperature in a single closed channel is calculated at a given axial segment by considering the balance of heat (conservation of energy) around a differential element, that is:

$$A\,G(z)\,\frac{dH(z)}{p} = q''(z)dz \qquad (2.2\text{-}89)$$

where A is the flow area of the assembly, G the mass flow rate, dH the enthalpy change, p the total heated perimeter of assembly, and q"(z) the surface heat flux of fuel rod at axial position z.

The bulk coolant temperature, $T_b(z)$ at a given axial position z is calculated by using the identity $dH = C_p dT$, and integrating Equation (2.2-89):

$$T_b(z) = T_{in} + \frac{4}{2\pi D_e}\int_{z}^{} \frac{q'(z)}{GC_p r}dz \qquad (2.2\text{-}90)$$

where T_{in} is the inlet coolant temperature (K), q the linear heat generation rate (W/m), r the cladding outer radius including crud and oxide thickness layers (m), C_p the heat capacity of the coolant (J/kg K), G the coolant mass flux (kg/m^2 s), and D_e the hydraulic diameter defined as:

$$D_e = \frac{\text{flow area}}{\text{wetted perimeter of duct}} \qquad (2.2\text{-}91)$$

or

$$D_e = \frac{4(P^2-\pi r^2)}{2\pi r} \qquad (2.2\text{-}92)$$

with P being the fuel rod center-to-center spacing, the so called pitch (m).

If T_b exceeds the saturation temperature, T_{sat}, then one simply sets:

$$T_b(z) = T_{sat} \qquad (2.2\text{-}93)$$

With the aid of Equation (2.2-90) the cladding outer surface temperature is calculated at the midplane of each axial segment along a fuel rod.

It should be mentioned that in computations all the variables in Equation (2.2-90) except C_p and r are given as the program input. The coolant heat capacity C_p is calculated for every axial segment by a steam properties generator subroutine STEAM (Reference 2-23), and r is calculated by the corrosion and cladding creep models of STAV6.2 described in Sections 2.2.3 and 2.2.5 respectively.

Metal-Oxide Surface Temperature

Two different mechanisms for coolant-to-cladding heat transfer mechanisms are considered: forced convection and nucleate boiling. [Proprietary Information Deleted]

[Proprietary Information Deleted]

2.2.7.2 Heat Transfer Model in Boiling Water Reactors

As mentioned earlier for BWRs the coolant is assumed to be at the saturation temperature at the specified operating pressure at all axial segments.

[Proprietary Information Deleted]

2.3 Fuel Rod Void Volumes

Fuel rod void volumes computed by STAV6.2 consist of the plenum volume, pellet-cladding gap, central hole volume (if it exists), and the inner pellet volumes of dishing and chamfer.

The gas mixture filling the void volumes consists of fill gas, usually helium, and fission gases xenon and krypton. The mixing of these gases are considered to be instantaneous.

2.3.1 Pellet-Cladding Gap Heat Transfer

2.3.1.1 General

Heat is transferred across the pellet-cladding gap by gaseous conduction and thermal radiation. However, upon the fuel clad contact, another heat transfer mode contributes to the gap conductance which leads to an enhancement of heat transfer. Gaseous conductance in the gap depends on the ratio of the mean free path of the gas to the gap width (Knudsen number). When the Knudsen number exceeds 0.01 a discontinuity between the gas temperature immediately adjacent to a bonding surface and the surface temperature would occur.

A continuous heat transfer can be considered if the real gap is extended into the solid surfaces by certain distances termed temperature jump lengths. The temperature jump lengths are usually estimated from the kinetic theory of gases. The jump lengths depend on the thermodynamic properties of the gas mixture and quantities that take into account the gas-solid interaction effects called the accommodation coefficients. The accommodation coefficients can be determined for the gases and the solid surfaces of interest experimentally.

The gap conductance model considered here includes analytical expressions for the gap conductance that takes into account the stochastic variation of surface roughness of the pellet and the clad. Furthermore, the effect of fuel cracking and relocation that makes the pellet surface uneven is treated. This model is presented fully in (Reference 2-26) and will be repeated in the following sections.

2.3.1.2 The Model

The fuel rod is considered to be a cylindrically symmetric system comprising of an inner cylinder being the nuclear fuel (pellet) enclosed in a metallic tube (cladding) with sealed ends, and a space (gas gap plus a plenum) for fuel expansion and accommodation of fission gas products.

The heat transfer across the fuel-cladding gap can be considered to take place by the following modes:

1. Solid-to-solid *radiation* heat transfer between the portions of the surface that are not in contact, that is through the interstitial volume.

2. Conduction heat transfer through the interstitial gas.

3. Solid-to-solid conduction heat transfer through the pellet-clad contact points. The actual contact area is dependent upon surface morphology, the applied load, and the mechanical properties of contacting materials.

The bulk heat transfer coefficient across the gap is formulated as follows:

$$h = h_r + h_g + h_c \qquad (2.3\text{-}1)$$

where h_r is the radiation heat transfer coefficient, h_g is the gas heat transfer coefficient, and h_c is the heat transfer coefficient due to pellet-clad contact.

The radiation heat transfer coefficient is given by:

$$h_r = K \frac{T_f^4 - T_c^4}{T_f - T_c} \qquad (2.3\text{-}2)$$

$$\text{with } K = \sigma \frac{\varepsilon_f \cdot \varepsilon_c}{\varepsilon_f + \varepsilon_c - \varepsilon_c \varepsilon_f}$$

where σ is the Stefan-Boltzmann constant, ε_f and ε_c are the emissivities of the fuel and the cladding, and T's are the temperatures at the respective surfaces, in degrees Kelvin.

The Solid Cylinder Pellet

Gaseous conductance in the gap depends on the ratio of the mean free path of the gas and the gap width, the Knudsen number. When the Knudsen number exceeds 0.01 a discontinuity between the gas temperature immediately adjacent to the bonding surface and the surface temperature would occur. A continuous heat transfer can be considered if the real gap is extended into solid surfaces by certain distances called temperature jump distances.

The heat transfer coefficient for a mixture of gases, h_g, is given by:

$$h_g = \sum_{i=1}^{n} h_i \qquad (2.3\text{-}3)$$

where h_i is the gas heat transfer coefficient for a single gas, and n is the number of gas components. As can be seen, these coefficients are combined in "parallel" to give the total gas mixture heat transfer coefficient. The heat transfer coefficient h_i in turn may be written as:

$$h_i = \frac{K_i^*}{G_i^*} \tag{2.3-4}$$

where G_i^* is the effective gap size for gas species i, defined below, and K_i^* is the effective thermal gas conductance of species i in the mixture. K_i^* can be calculated using the method of Brokaw, (Reference 2-27) which provides an averaging technique for calculating thermal conductivity of monoatomic and polyatomic gas mixtures, namely:

$$K_i^* = \frac{K_i}{1+\sum_{j=1}^{n}\psi_{ij}(x_j/x_i)} \tag{2.3-5}$$

where K is the thermal conductivity of constituent gas, x the mole fraction, and ψ_{ij} the weighting factor which is a function molecular weights, temperature, and viscosities (see Section A.4 in Appendix A.)

The effective gap, G_i^*, includes the variation of surface roughness of the pellet R_1 and of the cladding R_2. In general G^* is a function of (R_1 + R_2) and a quantity that we call thermal gap G_T defined as:

$$G_{iT} = G_{mp}+g_i \tag{2.3-6}$$

where G_{mp} is the mean plane gap (see Figure 2.3-1) defined by

$$G_{mp} = G_0+R_e$$

G_0 = As-fabricated design gap

$$R_e = \sqrt{5}\sqrt{R_1^2+R_2^2},$$

and g is the temperature jump distance given by (Reference 2-28)

$$g_i = \left(\frac{1}{\alpha_1}+\frac{1}{\alpha_2}-1\right)\frac{4}{1+\gamma_i}\frac{K_i}{\mu_i C_v}\lambda_i \tag{2.3-7}$$

where α_1 and α_2 are the accommodation coefficients for the fuel pellet and the cladding respectively, and γ_i (= C_p/C_v) is the ratio of gas specific heats, μ_i the viscosity, and λ_i the mean free path of the gas species i.

The accommodation coefficient is the fractional approach of the impinging molecules that come into thermal equilibrium with the solid before rebounding. A more precise definition of α is given by

$$\alpha = \frac{E_i - E_r}{E_i - E_w}$$

where E_i is the incident gas molecule flux, E_r the flux reemitted, and E_w is the flux that would leave the surface if the molecules were in complete Maxwellian equilibrium at temperature T. Thus if the scattered molecules are in complete thermal equilibrium with the surfaces, $E_r=E_w$ and $\alpha=1$.

From transport theory of gases we have the following relation for the thermal conductivity of polyatomic gases, Euken's formula (Reference 2-29):

$$K_i = \frac{9\gamma_i - 5}{4} \mu_i C_v \qquad (2.3\text{-}8)$$

The mean free path of the gas assuming smooth rigid elastic spherical molecules is derived by Chapman and Cowling (Reference 2-29). It is given by

$$\lambda_i = C \sqrt{T/M_i} \left(\frac{\mu_i^*}{P}\right) \qquad (2.3\text{-}9)$$

where λ_i is the mean free path (m) of gas i, C = 114.94, T the gas temperature (K), M_i the molecular weight of the species i, P the total gas pressure (Pa), and μ_i^* the effective viscosity (Pa.s) of gas species i which is calculated as follows:

$$\mu_i^* = \frac{\mu_i}{x_i + \sum_{j=1}^{n} \psi_{ij} x_j} \qquad (2.3\text{-}10)$$

Subsütuting Equation (2.3-8) and (2.3-9) into (2.3-7) yields

$$g_i = C \frac{9\gamma_i - 5}{1+\gamma_i} \left(\frac{1}{\alpha_1} + \frac{1}{\alpha_2} - 1\right) \sqrt{T/M_i} \left(\frac{\mu_i^*}{P}\right) \qquad (2.3\text{-}11)$$

with C = 114.94.

In Section A.4 of Appendix A the values for the accommodation coefficients, the g's, the thermal conductivities, the molecular weights, and the viscosities of gases used in the model are tabulated.

To calculate the effective gap G* the irregularities in pellet and clad surface roughness need to be described mathematically. Let w(r) be a distribution function characterizing the profile of the solid material surfaces with the following properties:

$$\int w(r)dr = 1$$

$$\int rw(r)dr = 0$$

[Proprietary Information Deleted]

[Proprietary Information Deleted] Upon calculation of G*, Equation (2.3-3) and (2.3-4) are used to determine the heat transfer coefficient in the gap. This completes the treatment of the gas conductance in the gap for the solid pellet. The gap heat transfer for the cracked pellet is treated in the next section.

The Cracked Pellet

Upon sufficient rise in rod power, large temperature gradient develops across the fuel pellet which produces cracks in the pellet. These cracks expend some of the free area of the gap, meaning that they cause the fuel perimeter to increase, the occurrence of pellet relocation. Pellet relocation changes the gas heat transfer coefficient and thus needs to be included in the gap heat transfer modeling.

[Proprietary Information Deleted]

Contact Conductance

When two solid surfaces come into contact, they touch one another only at limited number of points due to their surface irregularities. This implies that the actual area of contact between two solid surfaces is only a small fraction of the total surface area. A simple model that envisages the surface area of contact consists of cylinders of equal size, uniformly distributed over the apparent area of the contact was proposed by Todreas and Mikic (Reference 2-30) and has been adapted for our calculations in the STAV6.2 computer code. The expression for the contact gap conductance derived by Todreas and Mikic is given by:

$$h_{con} = f\,(P_c/H)^n \qquad (2.3\text{-}18)$$

where P_c is the interfacial pressure, H is the Meyer hardness

$$f = \frac{Ç\,\kappa_m}{\sqrt{R_1^2+R_2^2}} \qquad (2.3\text{-}19)$$

with

$$\kappa_m = \frac{2\kappa_1\kappa_2}{\kappa_1+\kappa_2}$$

the mean thermal conductivity of the fuel, κ, that of the cladding, κ_2, and

$$Ç = 77.40\,R_2^{0.528} \qquad (2.3\text{-}20)$$

The exponent in Equation (2.3-18) is given by

$n=1/2$ if $\frac{P_c}{H} < 0.001$

$n=1$ otherwise

The above constants in the correlations come from a fit to the Ross and Stoute data (Reference 2-31), plus the data of Rapier et al (Reference 2-32). This contact conductance model is also used in the FRACAS models in the FRAPCON code (Reference 2-33).

The Meyer hardness is a function of temperature, it decreases rapidly with increasing temperature, beginning at 2000 MPa at room temperature to 200 MPa at 827 K (Reference 2-18).

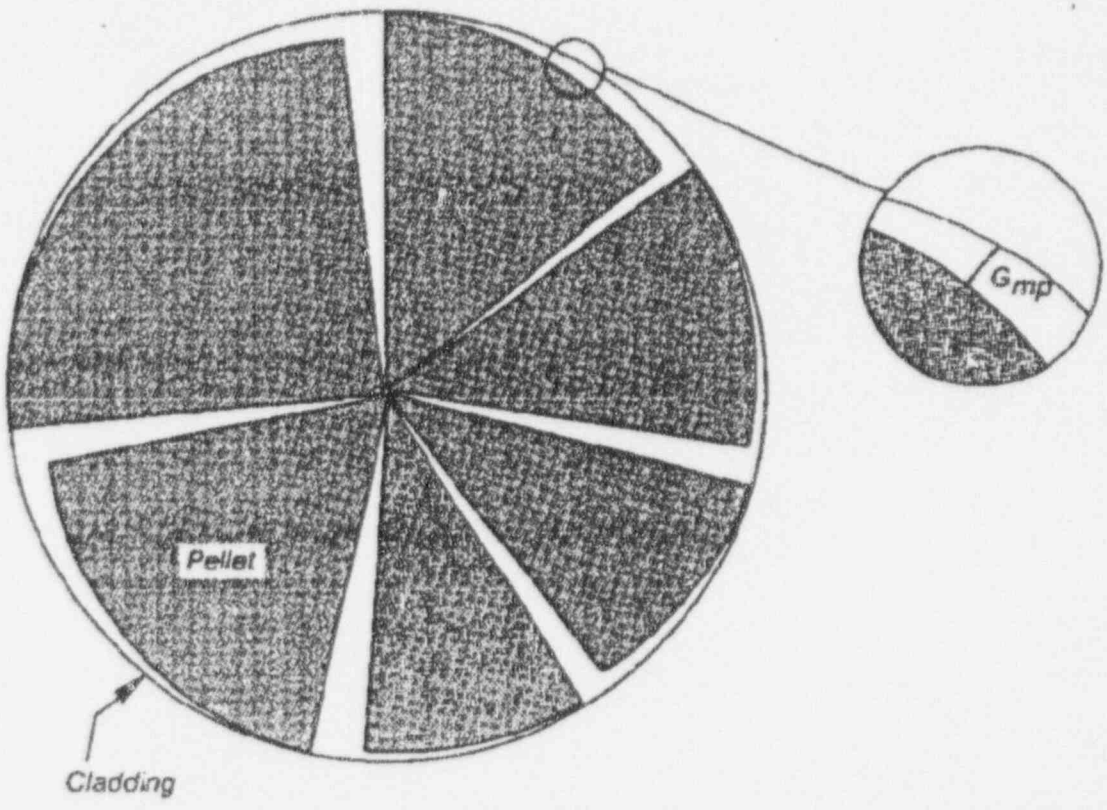

Figure 2.3-1 Model Representation of Pellet Relocation

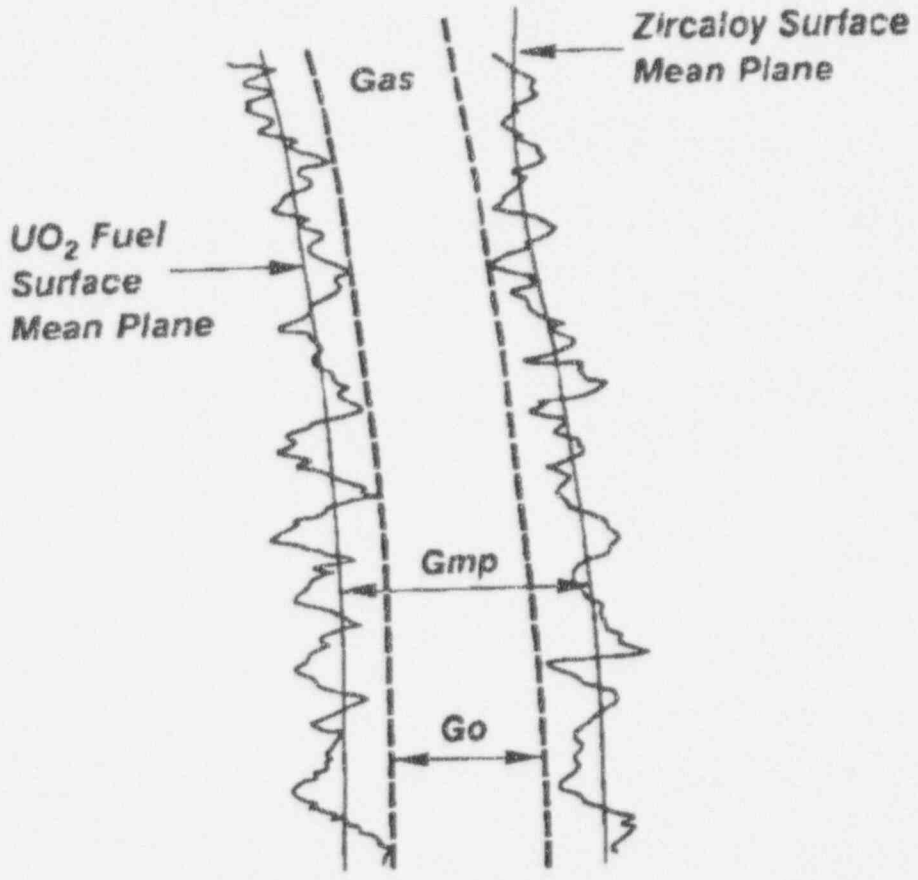

Figure 2.3-2 Schematic Representation of the Gas Gap in Fuel Rod

2.3.2 Rod Internal Gas Pressure

After the completion of fuel rod temperature and deformation calculations, the pressure of the gas in the fuel rod is computed. To calculate the gas pressure, the temperature and volume of the gas are necessary quantities. The rod internal gas pressure model is based on the following assumptions:

1. The ideal gas law holds

$$PV = NRT \qquad (2.3\text{-}21)$$

where, P is the pressure (Pa), V the volume (m^3), N the number of gas moles, R the gas constant (= 8.3143 J/moles K), and T the temperature (K), and

2. Gas pressure is constant throughout the fuel rod.

Fuel rod internal pressure is calculated from the ideal gas law (Equation (2.3-21)) modified to permit different volumes of gas at different temperatures as expressed by:

$$P = \frac{NR}{\sum_{i=0}^{n} \frac{V_i}{T_i}} \qquad (2.3\text{-}22)$$

where the sum is over the different volumes and their corresponding temperatures.

The free volumes and their associated temperatures considered in the computation of fuel rod internal gas pressure are summarized in Table 2.3-1.

TABLE 2.3-1 VOLUMES INCLUDED IN GAS PRESSURE CALCULATION

Proprietary Information Deleted

2.4 References

2-1 Z. Weiss, "Generalization of Amouyal-Benoist's Method for Calculating Disadvantage Factors and Flux Distributions in Two Region Cells," Nucl. Sci. and Eng., Vol. 22, pg. 60-77 (1965).

2-2 I. D. Palmer, K. W. Hesketh and P. A. Jackson, "A Model for Predicting the Radial Power Distribution in Fuel Pin," IAEA Specialist Meeting on Water Reactor Fuel Element Performance Computer Modelling, Preston, 24-229, March 1982.

2-3 A.R. Massih, S. Persson and Z. Weiss, "Modelling of (U, Gd)O_2 Fuel Behaviour in Boiling Water Reactors," J. Nucl. Mater., Vol. 188 , pg. 323-330 (1992).

2-4 M. Oguma, "Cracking and Relocation Behavior of Nuclear Fuel Pellets during Rise in Power," Nucl. Eng. & Design Vol. 76, pg. 35, (1983).

2-5 K. Forsberg and A. Massih, "A Model for Calculation of Fuel-pellet Gap Conductance," IAEA Technical Meeting on Fuel Element Computer Modeling in Steady-State Transient and Accident Conditions, Preston, England, 19-22 September 1988.

2-6 B. Danielsson, "Totala fissionsutbyte för Kr och Xe som funktion av utbränning," Studsvik Technical Report in Swedish, K4-79/71 (1979).

2-7 J. A. Turnbull, "The Effect of Grain Size on the Swelling and Gas Release Properties of UO_2 during Irradiation," J. Nucl. Mater., Vol. 60, pg. 62 (1974).

2-8 K. Forsberg and A.R. Massih, "Diffusion Theory of Fission Gas Migration in Irradiated Nuclear Material," J. Nucl. Mater., Vol. 135, pg 140, (1985).

2-9 R. J. White and M. O. Tucker, "A New Fission-gas Model," J. Nucl. Mater., Vol. 118, pg. 1 (1983).

2-10 A. R. Massih and B. Grapengiesser, "Modelling the Behavior of $(U,Gd)O_2$ Fuel - Comparison with Experiment," Enlarged Halden Programme Group Meeting on Fuel Performance Experiments and Analyses, Strömstad, Sweden, June 1984.

2-11 K. Forsberg and A. R. Massih, "Fission Gas Release under Time Varying Conditions," J. Nucl. Mater., Vol. 127, pg. 141 (1985).

2-12 C. Vitanza, E. Kolstad, and U. Graziani, "Analysis of Fission Gas Release Tests at High Burnup," ANS Topical Meeting on LWR Fuel Performance, Portland Oregon, April 29-May 3, 1979.

2-13 R. A. Lorenz, "ANS-5.4 Fission Gas Release Model III. Low Temperature Releases," ANS Topical Meeting on LWR Fuel Performance, Portland Oregon, April 29-May 3, 1979.

2-14 A. Mendelson, *Plasticity: Theory and Applications,* Chapter 9, Macmillan, New York, 1968.

2-15 F.A. Nichols, "Theory of the Creep of Zircaloy during Neutron Irradiation," J. Nucl. Mater., Vol. 30, pg. 249-270, (1969) .

2-16 K. Forsberg and A. R. Massih, "A Model for Uniform Zircaloy Clad Corrosion in Pressurized Water Reactors," IAEA Meeting on Fundamental Aspects of Corrosion of Zirconium Base Alloys in Water Reactor Environments, Portland, Oregon, September 11-15, 1989.

2-17 H. Maki, "Heat Transfer Characteristics of Zircaloy-2 Oxide Film," J. Nucl. Sci. and Tech., Vol. 10, pp 170-175 (1973).

2-18 D. L. Hagrman and G. A. Reymann, *MATPRO-version II- A handbook of materials properties for use in the analysis of light water reactor fuel behavior*, NUREG/CR-0497, 1979.

2-19 T. Kelén and J. Arvesen, "Temperature Increments from Deposits on Heat Transfer Surfaces," ATOMENERGI Report AE-459 (1972).

2-20 I. H. Dyce, "Corrosion of Zircaloy Fuel Cladding," Nuclear Engineering, Vol. 9, 253-255 (1964).

2-21 A. B. Johnson, Jr., "Thickness-film Effects in the Oxidation and Hydriding of Zr Alloys," IAEA Meeting on Fundamental Aspects of Corrosion of Zirconium Base Alloys in Water Reactor Environments, Portland, Oregon, September 11-15, 1989. (Pacific Northwest Laboratory, Report PNL-SA-17065.)

2-22 J. A. Dean, *Handbook of Chemistry*, 12th Edition, McGraw-Hill, 1979.

2-23 L. Haar, J.S. Gallagher and G.S. Kell, *NBS/NRC Steam & Tables*, Hempshire, Washington (1984).

2-24 L.S. Tong and J. Weisman, *Thermal Analysis of Pressurized Water Reactors*, Chapter 4, American Nuclear Society, La Grange Park, 1979.

2-25 F. Garzarolli et al, "Review of PWR Fuel Rod Waterside Corrosion Behavior," EPRI NP-2789, December 1982.

2-26 K. Forsberg, and A.R. Massih, "A Model for Calculation of the Fuel-clad Gap Conductance," IAEA Meeting on Water Reactor Fuel Element Modelling in Steady-State Transient and Accident Conditions, Preston, England 19 - 22 September 1988.

2-27 A. L. Lindsay and L. A. Bromley, "Thermal Conductivity of Gas Mixtures," Ind. and Eng. Chem., Vol. 42, pg. 1508, (1950).

2-28 E.H. Kennard, *Kinetic Theory of Gases*, McGraw-Hill, New-York, 1938.

2-29 S. Chapman and T.G. Cowling, *The Mathematical Theory of Non-Uniform Gases*, (Cambridge University Press, Cambridge, 1939.

2-30 G. Jacobs and N. Todreas,, "Thermal Contact Conductance in Reactor Fuel Elements," Nucl. Sci. Eng., Vol. 50, pg. 283, (1973).

2-31 A. M. Ross and R. L. Stoute, "Heat Transfer Coefficients Between UO_2 and Zircaloy-2," Report CRFD-1075, (1962).

2-32 A.C. Rapier, T.M. Jones and J.E. McIntosh, "The Thermal Conductance of Uranium-Dioxide/Stainless-Steel," Int. J. Heat Transfer, Vol. 6, pg. 379, (1963).

2-33 G.A. Bernal et al, "FRAPCON-2 A Computer Code for the Calculation of Steady-State Thermal-Mechanical Behavior of Oxide Fuel Rods," Report NUREG/CR-1845 (1981).

3 STAV6.2 COMPUTER CODE QUALIFICATION

3.1 INTRODUCTION

This section presents the verification and validation of the ABB fuel performance code STAV6.2. It includes qualification of all the models described in Section 2 through separate and integrated experimental benchmarkings. Benchmarking for BWR applications is presented since the current U.S. application is solely for BWRs. The extensive qualification bases of the STAV6.2 code also include qualification against PWR fuel performance data. The qualifications presented here include: xenon and krypton production, high and low temperature fission gas release, helium release, pellet-cladding mechanical interaction, Zircaloy cladding creepdown, axial growth, waterside corrision and hydrogen pickup, pellet cladding gap heat transfer, centerline temperatures (beginning of life and during irradiation), and end of life free volume. The benchmarking calculations and results are presented in a similar order to that of Section 2, which describes the STAV6.2 code models.

The detailed qualification work presented in this section, both for BWR applications, demonstrate the applicability of the STAV6.2 for boiling water reactor fuel design.

3.2 TEMPERATURE COMPARISONS

3.2.1 Beginning-of-Life Centerline Temperature

3.2.1.1 Database and Rod Characteristics

The benchmarking calculations for the beginning-of-life centerline temperatures were carried out using Halden reactor experimental rods. The rods, forming the data base for this particular verification are listed in Table 3.1.

The diametral gap, fill gas, prepressurization and active length of these rods varied according to Table 3-1. The variation in fuel rod design generates a set of benchmarking data which covers the heat transfer conditions at different burnups for ordinary commercial fuel rods for which the pellet-cladding gap is continuously closing and the fission gases are released. Complete sets of information on the rods can be found in References 3-1 through 3-4.

3.2.1.2 Results

The STAV6.2 calculated values of centerline temperature are compared to measured values for individual fuel rods in Figures 3-1 through 3-14. [Proprietary Information Deleted]

[Proprietary Information Deleted]

3.2.2 Burnup Dependent Centerline Temperature

3.2.2.1 Rod Characteristics and Irradiation Data

The data base for the burnup dependent in-life fuel centerline temperature benchmarking, including a summary of burnup specific and geometric data, is presented in Table 3-2.

IFA-432

The nine rods in the IFA-432 assembly were designed to provide fuel temperature data as a function of burnup and also to study the effects of varying pellet-clad gap size, fuel density and fuel stability. The Rods 1, 2, 3 and 5 were selected in the fuel pellet centerline temperature benchmarking of STAV6.2.

Moreover, the rods were designed to simulate BWR-6 type fuel with Zircaloy-2 cladding. The diametral gap size varied from 60 to 382 μm and the rods were prepressurized to 1 atmosphere with helium gas. The four evaluated rods had an active length of 578 mm and an enrichment of 10%.

The fuel centerline temperature was measured with thermocouples inserted in the upper and lower parts of the rods. An exception was Rod 2 which had an ultrasonic thermometer inserted in its upper part instead of a thermocouple.

During most of its irradiation time, the IFA-432 assembly was positioned so that the peak powers in the fuel were in the 40 to 50 kW/m range. Reliable experimental data are available to rod burnup levels of 30-40 MWd/kgU. Further details concerning geometric data, instrumentation and irradiation histories, for the rods in the IFA-432 assembly, are given in Reference 3-5.

IFA-509

[Proprietary Information Deleted]

3.2.2.2 STAV6.2 Input

Input data to STAV6.2 were taken from References 3-5 and 3-6.

Because of prepuncture leakage of gas, the measured fission gas release in the IFA-432 Rods 2, 3 and 5 was very low. [Proprietary Information Deleted]

The irradiation input data for the IFA-432 rods were prepared manually from tabulated power histories given in Reference 3-5. These power data were estimated to be accurate to ±10% at the 2σ (95%) confidence level in the same reference. For the IFA-509 rod, the power history was averaged manually from diagrams provided in Reference 3-6.

3.2.2.3 Results

The STAV6.2 calculated temperatures were compared to measured temperatures which were manually averaged from tabulated or plotted temperature histories given in References 3-5 and 3-6.

Individual plots showing rod power history, measured and predicted centerline temperature as a function of rod average burnup and predicted versus measured temperature are depicted in Figures 3-17 through 3-21. Figure 3-22 shows the total outcome of the evaluation in a plot of predicted fuel pellet centerline temperature versus measured. [Proprietary Information Deleted]

3.3 GASEOUS FISSION PRODUCT RELEASE

3.3.1 Helium Release

3.3.1.1 Model

The gas within a fuel rod consists of fill gas, typically helium, trace amounts of impurity or sintering gases adsorbed or trapped within the fuel. As burnup proceeds increasing amounts of fission gases are released to the fuel rod free volume.

Helium, krypton and xenon are the important fission product gases produced and released during reactor operation. The helium release model STAV6.2 is based on the approximation that equal amounts of helium and krypton are released.

3.3.1.2 Qualification

[Proprietary Information Deleted]

3.3.2 Xenon and Krypton Production

3.3.2.1 Model

[Proprietary Information Deleted]

3.3.2.2 Qualification

The xenon and krypton production models have been verified utilizing measured equivalent volumes of helium and krypton obtained by post irradiation examination [Proprietary Information Deleted]

[Proprietary Information Deleted]

3.3.3 Athermal Fission Gas Release

3.3.3.1 Introduction

The fission gas release model in STAV6.2 considers the fractional gas release to consist of two additive components, thermal and athermal gas release. The athermal fission gas release is caused by knock-out and recoil processes in nuclear fuel during fissioning, and as such it is fission rate dependent but not temperature dependent (athermal process). On the other hand the athermal release, in Light Water Reactors (LWRs) during normal operation, is highly temperature dependent and is governed primarily by thermal diffusion, grain boundary saturation and re-solution of gas atoms. The thermal release is substantially larger than the athermal release.

In LWR fuel there is a considerable buildup of plutonium at the pellet periphery with increasing fuel burnup. Therefore, at higher burnups, an increasing fraction of the fissioning will take place at the pellet periphery which enhances the athermal release.

3.3.3.2 Model Calibration

[Proprietary Information Deleted]

3.3.4 Thermal Fission Gas Release

3.3.4.1 BWR Fuel Designs

Table 3-6 summarizes the BWR data base in terms of end-of-life discharge rod average burnup and peak power level. The helium fill pressure is also included. The position of the rod within the assembly is shown by the rod identification in Table 3-6 and the assembly map provided in Figure 3-31.

As described in Section 2, STAV6.2 considers the fission gas release process to consist of two additive components, thermal and athermal fission gas release. The calibration of the athermal release model was evaluated in Section 3.3.3. The thermal release, which occurs

during normal operation, is highly temperature dependent. It is governed primarily by thermal diffusion, grain boundary saturation and resolution of gas atoms. This model is calibrated against measured release data by determining the best value of the resolution factor, the h_4 factor in Section 2, which affects the probability that fission gas atom on the grain boundaries will resolve back into the UO_2 matrix.

Summary of BWR Data Base

[Proprietary Information Deleted]

STAV6.2 Input Densification

[Proprietary Information Deleted]

Evaluation Outcome and Discussion of BWR Rod Results

[Proprietary Information Deleted]

3.3.4.2 Thermal Fission Gas Release Sensitivity Study

In this section the results of three steady state analytical calculations of N(t) based on the diffusion and re-solution model, References 3-18 and 3-19 and the present model are compared. These expressions are summarized as follows.

Analytical solution of Equation 2.1-29 can be obtained for short and long time limits in the case where the ratios $\beta_e = \beta(t) / D(t)$ and $b(t)\lambda / D(t) = h_1$ are time independent. It was shown in Reference 3-20 that for short times the areal density of the intergranular gas is given by

$$N(\tau) = \frac{2\beta_e}{h_1}\left(\tau + \frac{1}{h_2 h_3}\right.$$

$$\left. \frac{h_2 \exp(h^2{}_3\tau)\operatorname{erfc}(h_3\tau^{1/2}) + h_3 \exp(h^2{}_2\tau)\operatorname{erfc}(-h_2\tau^{1/2})}{h_2 h_3 (h_2 + h_3)}\right) + 0(\tau\infty),$$

$$h_2 = -\frac{h_1}{2} + \left(\frac{h_1^2}{4} + \frac{h_1}{a}\right)^{1/2}$$

$$h_3 = \frac{h_1}{2} + \left(\frac{h_1^2}{4} + \frac{h_1}{a}\right)^{1/2}, \quad \text{for } \frac{Dt}{a^2} < \frac{1}{\pi^2}$$

$$\text{and } \tau = \int_0^t D(t_o)dt_o$$

For long times

$$N(\tau) = \frac{2\beta_e a}{(3+h_1 a)}\left[\tau - \frac{a^2}{5(3+h_1 a)}\right] + \sum_{m=1}^{\infty} \frac{4\beta_e a^3 e^{-(u_m/a)^2\tau}}{u_m^2\,[u_m^2 + ah_{1\Delta}\,(3+ah_1)]},$$

$$\text{for } \frac{Dt}{a^2} < \frac{1}{\pi^2}$$

where

$$u_m = \arctan\left(\frac{ah_1\,u_m}{u_m^2 + ah_1}\right) + m \cdot \pi$$

These short time and long time equations for $N(\tau)$ are the result of exact calculations within the regions of their applicability.

Other treatments of diffusion-resolution models have provided analytical expressions for N(t), Reference 3-19. For example, Olander, by making the simplifying assumption that in the narrow region width λ adjacent to the grain boundary the concentration profile is time independent, Reference 3-18, analytically calculates N(t). Applying the diffusion equation, Olander obtains the following expression for the intergranular gas density.

$$N(y) = \frac{2D^2\beta}{b^3\lambda^3}\left[1 - \frac{2}{\pi^{1/2}}\,y^{1/2} + y - e^y \operatorname{erfc}(y^{1/2})\right]$$

$$- \frac{2\beta D}{b^2\lambda}\left[1 - \frac{2}{\pi^{1/2}}\,y^{1/2} - e^y \operatorname{erfc}(y^{1/2})\right]$$

$$- \frac{\beta\lambda}{b}\,[1 - e^y \operatorname{erfc}(y^{1/2})] \quad \text{for } bt > 5 \text{ and } \frac{Dt}{a^2} \ll 1$$

where

$$y = \left(\frac{b\lambda}{D^{1/2}}\right)^2 t$$

This expression for N(y) was derived with the assumption that bt >> 1 and $\frac{Dt}{a^2} << 1$, where the lower limit of the former is taken to be bt > 5. It is noted that such a restriction was not imposed in the derivation of the short and long time functions N(τ) above.

Similarly a calculation based on the kinetic equation for N(τ) proposed by Speight gives for short times (Reference 3-19).

$$N(y) = \frac{\beta\pi D^2}{4(b\lambda)^3}\left\{1-4\left(\frac{y}{\pi}\right)^{1/2}+8\left(\frac{y}{\pi}\right)-2\exp\left[-4\left(\frac{y}{\pi}\right)^{1/2}\right]\right\}$$

for $\frac{Dt}{a^2} < \frac{1}{\pi^2}$.

[Proprietary Information Deleted]

3.4 CLAD CREEP DOWN

Clad creep is a time dependent permanent deformation process occuring under an applied stress. It can involve several mechanisms including slip, twinning and grain boundary sliding, and is stress, temperature, time and fast neutron flux (>1 MeV) dependent. The creep rate reduces rapidly with time after initiation as resistance to deformation builds up by strain (or irradiation) hardening. This early stage, primary creep, may last for durations varying between a few hours to about 1000 hours, depending on fabrication, prior history of the material, stress and temperature. The later stages of creep comprise a so-called steady-state period, secondary creep, during which the strain rate remains constant because any further hardening is balanced by thermal recovery.

3.4.1 BWR Clad Creep

The STAV6.2 BWR clad creep model has been calibrated against a data base consisting of [Proprietary Information Deleted] Figure 3-42 shows the measured hoop creep strain as a function of irradiation time for all of the these rods.

[Proprietary Information Deleted]

3.4.2 Pellet-Clad Mechanical Interaction

3.4.2.1 Introduction

Upon pellet-clad contact, pressure and friction forces start to act on the cladding wall and a displacement of the cladding diameter occurs. [Proprietary Information Deleted]

3.4.2.2 Model Calibration

[Proprietary Information Deleted]

3.5 ROD GROWTH

Rod growth is a complex phenomenon which is not only a function of mac roscopic variables such as stress, temperature and fast neutron flux MeV), but also depends on Zircaloy crystallographic texture, disloc. ion density, grain size, alloying additions and impurities. [Proprietary Information Deleted]

[Proprietary Information Deleted]

3.6 WAT ER SIDE CLADDING CORROSION AND HYDRIDING

3.6.1 BWR Environment

3.6.1.1 Corrosion

In BWRs the corrosion of beta-quenched Zircaloy-2 cladding (by ABB referred to as LK-II type of cladding) is not uniform. Corrosion consists of small nodules scattered within a thin uniform oxide. In-reactor cladding nodular corrosion is independent of temperature whereas the uniform corrosion is strongly temperature dependent. Because of the relatively low temperature in a BWR, the uniform oxide layer thickness is very low, typically a few microns, but the formation of nodules increases the average oxide layer thickness. The STAV6.2 model for BWR waterside corrosion is described in Section 2.2.5.2.

[Proprietary Information Deleted]

3.6.1.2 Cladding Hydriding

During operation of reactors, Zircaloy cladding tubes pick up hydrogen. The hydrogen pickup emanates from several sources of which the most important are:

- Hydrogen produced in the corrosion reaction

$$Zr + 2H_2O \longrightarrow ZrO_2 + 4H$$

- H_2 dissolved in the water steam
- Hydrogen produced by the radiolytic decomposition of H_2O in a radiation field

$$H_2O \longrightarrow H + OH$$

When the hydrogen concentration in Zircaloy exceeds its terminal solubility, zirconium hydride precipitation occurs. Excessive hydriding of Zircaloy reduces the ductility causing hydrogen embrittlement.

[Proprietary Information Deleted]

3.7 END-OF-LIFE ROD FREE VOLUME

The final verification of STAV6.2 for BWR applications is made by comparing the measured end-of-life rod free volume data with the predicted value for the same rods used for fission gas release given in Table 3-6. The end-of-life free volume is an integral test of clad creep down, fuel densification and swelling, rod growth and indirectly the fission gas release model since all these entities contribute to the dimensional changes of the rod which determine its free volume at end-of-life. [Proprietary Information Deleted]

[Proprietary Information Deleted]

3.8 PELLET CLADDING GAP CONDUCTANCE

The results of the STAV6.2 gap conductance model calculations are compared with the experimental data of Garnier and Begej, References 3-21 and 3-22. The experimental data were obtained from out-of-reactor measurements of gap conductance using laser pulse technique. The measurements were carried out under a variety of gas temperatures, pressures, gas mixtures, surface roughnesses, and gap sizes. The gas temperature varied from 293 to 873K, the gas pressure ranged from 0 to 14 MPa, the contact pressure ranged from 0 to 50 MPa, the fuel surface roughness ranged from 0.25-14.4 μm, and the cladding surface roughness ranged from 0.17 to 4.5 μm. Pure helium, pure argon, helium/argon mixture, and different helium/xenon mixtures were used in these experiments.

The accommodation coefficients used in the model for this comparison were taken from the work of Thomas and Loyalka on engineering surfaces, References 3-23 and 3-24.

Proprietary Information Deleted

3.9 SUMMARY

Based on extensive analyses presented in this report, it is demonstrated that STAV6.2 can be used for boiling water reactor fuel rod design and licensing applications.

3.10 REFERENCES

3-1 K. O. Vilpponen, N. T. Førdestrømmen, Temperature Behaviour in Xe and He Filled Fuel Rods, (Status IFA-509), Paper presented at the Enlarged Halden Group Meeting, Hankø, Norway, 1979.

3-2 K. O. Vilpponen, N. T. Førdestrømmen, "Thermal Response of Fuel Rods to Different Operating Conditions," Halden Report, HPR 240, 1980.

3-3 E. Kolstad (Editor), "Reactor Fuel Performance Modelling Workshop," Vääksy, Finland 14th - 18th June, 1982, Halden Report, HWR 81.

3-4 D. O. Sheppard, H. Devold, "Fission Gas Release, Thermal and Mechanical, Performance of IFA-513 (Status Report)," Halden Report, HWR 12, 1981.

3-5 D. D. Lanning, "Irradiation History and Final Post-irradiation Data for IFA-432," NUREG/CR-4717.

3-6 E. Patrakka, H. U. Staal, E. Kolstad, S. Granata, "3-Rod Diameter Rig IFA-509 - Data Report on Rod No. 3, Halden Report," HWR 93, 1983.

3-7 D. G. Franklin, G. E. Lucas, A L Bement, "Creep of Zirconium Alloys in Nuclear Reactors," ASTM Publication Code Number (PCN), 04-815000-35.

3-8 E. Kolstad, "The 3 Rod Diameter Experiments IFA-404(I) and IFA-404(2)," EHPG Meeting, Geilo, HPR 190, 1975.

3-9 "Test Case Descriptions, OECD Halden Reactor Project," Reactor Fuel Performance Modelling Meeting, Tallukka, Finland, 15th - 17th June, 1982.

3-10 L. Hallstadius, "Fabrication, Pre-irradiation Characterization, and Irradiation History for TVO I Rods," Batelle Report, HBEP-51 (3P17), 1988.

3-11 L. A. Goldsmith, P. D. Kennedy, A. J. Manley, G. McKee, I. Robinson and B. Scogings, "NDT Examinations of Nine BWR Fuel Rods Irradiated in TVO-1 - Task 3," Batelle Report, HBEP-55 (3P21), 1989.

3-12 S. Birath and G. Lysell, "Fission Gas Determination on Fuel Rods from OII," Studsvik Report, NF(P)-83-13, 1983

3-13 T. Jonsson, "EBU av 2 bränsleSTAV6.2ar bestrålade i Barsebäck 2, Delrapport 1. Fissionsgasfrigörelse," Studsvik Report in Swedish, NF(P)-87/29, 1987.

3-14 B. Danielsson and G. Lysell, "EBU kraftreaktorbränsle Ringhals 1, uttaget 1982," Studsvik Report in Swedish, NF(P)-84/60, 1984.

3-15 Reference Deleted

3-16 Reference Deleted

3-17 Reference Deleted

3-18 D. R. Olander, *Fundamental Aspects of Nuclear Fuel Elements,* (Chap. 15, U.S. Department of Energy Technical Information Center, 1976).

3-19 R. J. White and M. O. Tucker, "A New Fission-gas Model," J. Nucl. Mater., Vol. 118, pg. 1, 1983.

3-20 K. Forsberg and A.R. Massih, "Diffusion Theory of Fission Gas Migration in Irradiated Nuclear Material," J. Nucl. Mater., Vol. 135, pg. 140, 1985.

3-21 J.E. Garnier and S. Begej, "Ex-Reactor Determination of Thermal Gap Conductance Between Uranium Dioxide and Zircaloy-4, Stage II: High Gas Pressure," Rep. NUREG/CR-0330, PNL-3232, Vol. 2, U.S. Nuclear Regulatory Commission, 1980.

3-22 J.E. Garnier and S. Begej, "Ex-Reactor Determination of Thermal Gap Conductance Between Uranium Dioxide and Zircaloy-4, Stage I: Low Gas Pressure," Rep. NUREG/CR-0330, PNL-2696 Vol. 1, U.S. Nuclear Regulatory Commission, 1979.

3-23 L. B. Thomas and S.K. Loyalka, "Determination of Thermal Accommodation Coefficients of Helium, Argon, and Xenon on a Surface of Zircaloy-2 at About 25°C," Nucl. Technol., Vol. 57, pg. 213, 1982.

3-24 L.B. Thomas and S.K. Loyalka, "Determination of Thermal Accommodation Coefficients of Inert Gases on a Surface of

Vitreous UO2 at About 35°C," Nucl. Technol., Vol. 59, pg. 63, 1982.

3-25 G Neuer and T.N. Minh, "Experimentelle Untersuchung des Wärmedurchgangs im Spalt zwischen Brennstoff und Hülle von Leichtwasser-reaktor-Brennstäben, Atomkernenergie Kerntechnik," Vol. 47, pg. 229, 1985.

3-26 K. Lassmann and F. Hohlefeld, "The Revised URGAP Model to Describe the Gap Conductance Between Fuel and Cladding," Nucl. Eng. Des., Vol. 103, pg. 215, 1987.

3-27 R. Jansson, K. Lassmann, A. R. Massih, "Comparison Between the Fuel-to-Cladding Gap Conductance Models URGAP and GTEMP with Out-of-Pile Experiments", Transaction of two international seminars on the mathematical/mechanical modelling of reactor fuel elements, Commision of European Communities, Nuclear Science and Technology, EUR 13660 EN, 1991.

TABLE 3-1 BEGINNING-OF-LIFE CENTERLINE TEMPERATURE BENCHMARKING DATABASE

Proprietary Information Deleted

TABLE 3-2 BURNUP DEPENDENT CENTERLINE TEMPERATURE BENCHMARKING DATA BASE

Reactor	Assembly	Rod	Rod Type	Diametral Gap μm	Helium Fill Pressure MPa	End-of-Life Rod Average Burnup MWd/kgU
OECD/ Halden	IFA-432	1	BWR	222	0.1	30
	IFA-432	2	BWR	382	0.1	39
	IFA-432	3	BWR	82	0.1	39
	IFA-432	5	BWR	232	0.1	40

Proprietary Information Deleted

TABLE 3-3 THROUGH 3-11

PROPRIETARY INFORMATION DELETED

FIGURES 3-1 THROUGH 3-16

PROPRIETARY INFORMATION DELETED

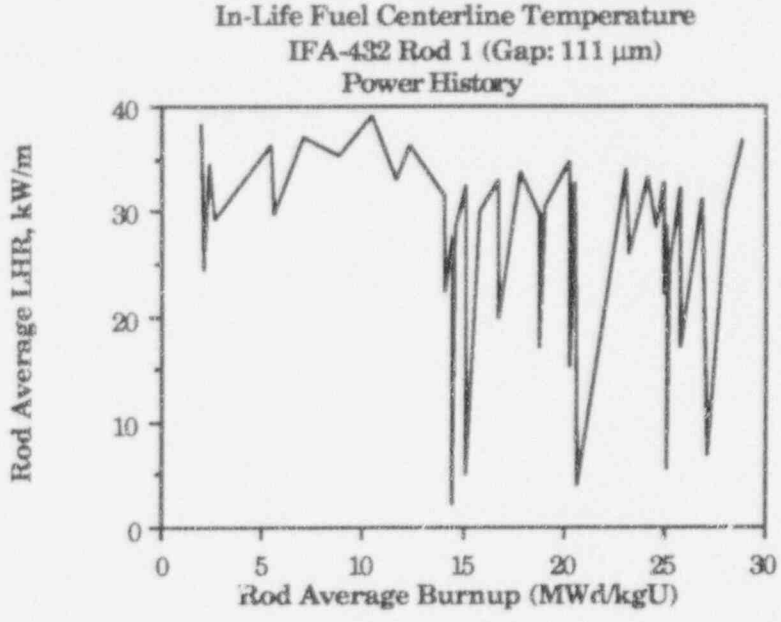

Figure 3-17a **In Life Fuel Centerline Temperature, IFA-432 Rod 1 (Gap: 111 μm)**

[Proprietary Information Deleted]

Figure 3-17b **In Life Fuel Centerline Temperature, IFA-432 Rod 1 (Gap: 111 μm)**

[Proprietary Information Deleted]

Figure 3-17c **In Life Fuel Centerline Temperature, IFA-432 Rod 1 (Gap: 111 μm)**

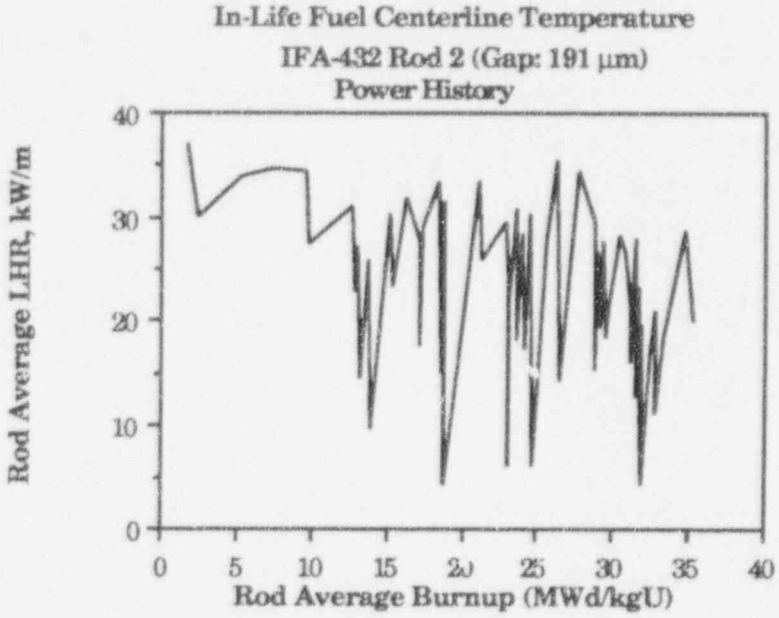

Figure 3-18a **In Life Fuel Centerline Temperature: IFA-432 Rod 2 (Gap: 191 μm)**

[Proprietary Information Deleted]

Figure 3-18b **In Life Fuel Centerline Temperature: IFA-432 Rod 2 (Gap: 191 μm)**

[Proprietary Information Deleted]

Figure 3-18c **In Life Fuel Centerline Temperature: IFA-432 Rod 2 (Gap: 191 μm)**

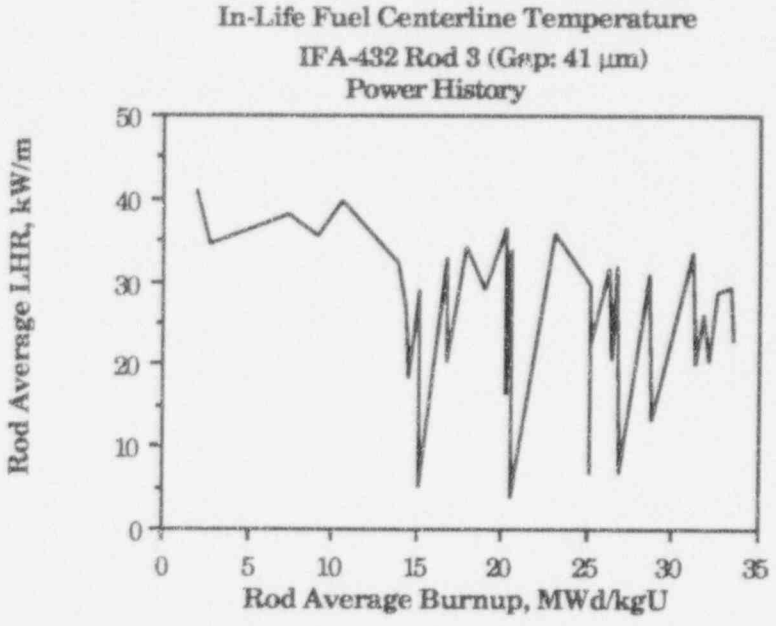

Figure 3-19a **In Life Fuel Centerline Temperature: IFA-432 Rod 3 (Gap: 41 μm)**

[Proprietary Information Deleted]

Figure 3-19b **In Life Fuel Centerline Temperature: IFA-432 Rod 3 (Gap: 41 μm)**

[Proprietary Information Deleted]

Figure 3-19c **In Life Fuel Centerline Temperature: IFA-432 Rod 3 (Gap: 41 μm)**

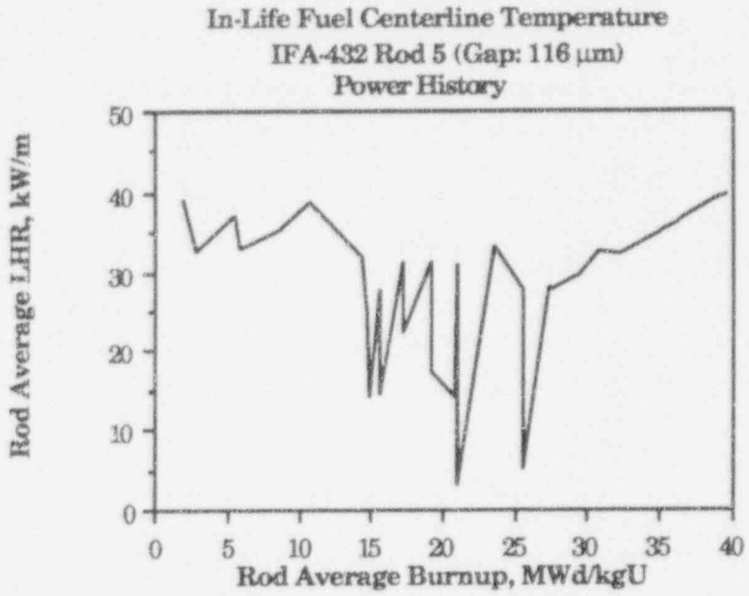

Figure 3-20a **In Life Fuel Centerline Temperature: IFA-432 Rod 5 (Gap: 116 μm)**

[Proprietary Information Deleted]

Figure 3-20b **In Life Fuel Centerline Temperature: IFA-432 Rod 5 (Gap: 116 μm)**

[Proprietary Information Deleted]

Figure 3-20c **In Life Fuel Centerline Temperature: IFA-432 Rod 5 (Gap: 116 μm)**

FIGURE 3-21 THROUGH 3-26

PROPRIETARY INFORMATION DELETED

[Proprietary Information Deleted]

Figure 3-27 **BWR Xenon and Krypton Production Measured Ratio of Released Xe Over Kr versus Burnup**

[Proprietary Information Deleted]

Figure 3-28 BWR Athermal Fission Gas Release Model Calibration Data Base

[Proprietary Information Deleted]

Figure 3-29 BWR Athermal Fission Gas Release Model Best Estimate Predicted versus Measured

[Proprietary Information Deleted]

Figure 3-30 BWR Athermal Fission Gas Release Model Upper Bound Predicted versus Measured

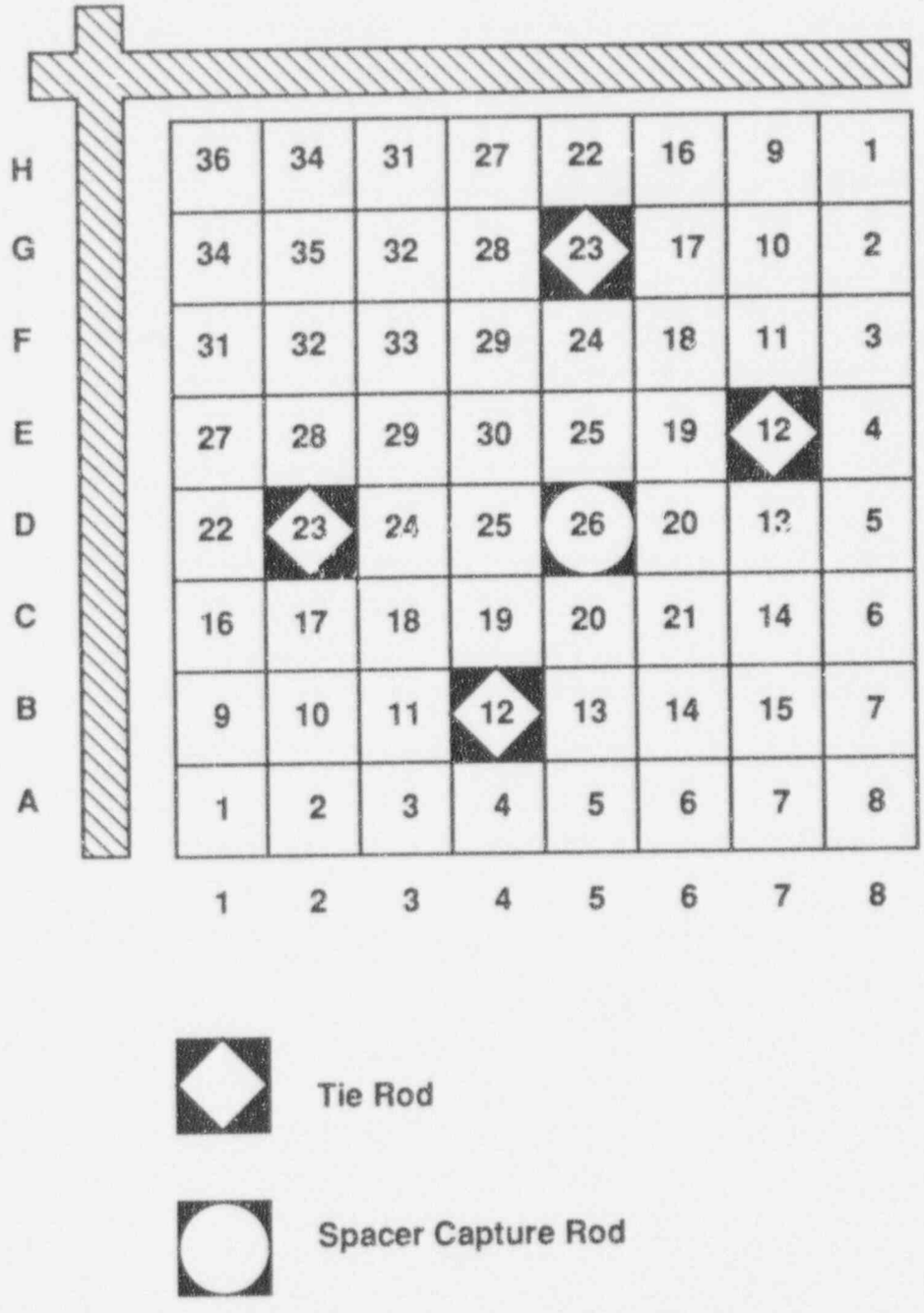

Figure 3-31 Rod Location Map

[Proprietary Information Deleted]

Figure 3-32 BWR Fission Gas Release Model Verification Data Base

[Proprietary Information Deleted]

Figure 3-33 BWR Fission Gas Release Nominal Predicted versus Measured

[Proprietary Information Deleted]

Figure 3-34 BWR Fission Gas Release Conservatively Predicted versus Measured

[Proprietary Information Deleted]

Figure 3-35 Evolution of saturation of fission gases in grain boundaries calculated by different models.

[Proprietary Information Deleted]

Figure 3-36 Evolution of saturation of fission gases in grain boundaries calculated at different temperatures. In this calculation b=1. E-5 /s and λ= 2.E-8 m are used.

FIGURES 3-37 THROUGH 3-42

PROPRIETARY INFORMATION DELETED

[Proprietary Information Deleted]

Figure 3-43a BWR Clad Creep Strain, Best Estimate Model Prediction

[Proprietary Information Deleted]

Figure 3-43b BWR Clad Creep Strain, Upper Bound Model Prediction

[Proprietary Information Deleted]

Figure 3-43c BWR Clad Creep Strain, Lower Bound Model Prediction

[Proprietary Information Deleted]

Figure 3-44 BWR Clad Creep Strain Measured - Predicted versus Irradiation Time

FIGURES 3-45 THROUGH 3-51

PROPRIETARY INFORMATION DELETED

[Proprietary Information Deleted]

Figure 3-52 BWR Rod Growth Model Calibration Database

[Proprietary Information Deleted]

Figure 3-53 BWR Clad Waterside Corrosion Model Verification Data Base

FIGURES 3-45 THROUGH 3-51

PROPRIETARY INFORMATION DELETED

[Proprietary Information Deleted]

Figure 3-63 Cladding Hydriding Model Calibration Data Base

[Proprietary Information Deleted]

Figure 3-64 BWR End-of-Life Rod Free Volume Nominal Predicted versus Measured

[Proprietary Information Deleted]

Figure 3-65 Helium Gas Gap Thermal Conductance: Predicted Versus Measured.

[Proprietary Information Deleted]

Figure 3-66 Argon Gas Gap Thermal Conductance: Predicted Versus Measured.

[Proprietary Information Deleted]

Figure 3-67 Helium, Argon Gas Mixture Gap Thermal Conductance: Predicted Versus Measured.

[Proprietary Information Deleted]

Figure 3-68 Helium, Xenon Gas Mixture Gap Thermal Conductance: Predicted Versus Measured.

[Proprietary Information Deleted]

[Figure 3-69 Proprietary Information Deleted]

4 VIK-2 COMPUTER CODE DESCRIPTION

The computer program VIK-2 calculates stresses in a light water reactor (LWR) fuel rod at beginning of life. Both fully recrystallized Zircaloy cladding and cold work stress relief Zircaloy cladding can be treated. The code consists of a number of subroutines, each calculating the stress due to the different sources. The stresses are calculated at the the clad inner and outer radius at specific locations. Depending on the origin of the stress and on geometrical and material discontinuities in the structure each stress is classified in a certain stress category. The calculation of the effective and the allowed stresses can be done in agreement with the ASME Section III Article NB-3000. The effective stress according to ASME III is calculated by using the Tresca formula. The safety factor is calculated by dividing the allowed stress by the maximum effective stress.

The VIK-2 models use classical continuum mechanics. In the upcoming sections the models used in the code are described, and the relevant algebraic expressions are provided. Most of the derivations of the equations are in the literature. References are given to these works. Figure 1-2 of Section 1 provides an overview of the VIK-2 calculations.

4.1 VIK-2 MODELS

4.1.1 Clad Internal and External Pressure

The stresses caused by loading of a fuel rod with internal gas pressure and external coolant pressure are calculated from the classical equation of Reference 4-2. [Proprietary Information Deleted]

[Proprietary Information Deleted]

[Proprietary Information Deleted]

[Figure 4-1 Proprietary Information Deleted]

[Proprietary Information Deleted]

4.1.2 Stress at the Bottom End Plug

Stresses caused by the internal rod pressure and external coolant pressure at the bottom end plug of a fuel rod are calculated in VIK-2. [Proprietary Information Deleted]

[Proprietary Information Deleted]

[Figure 4-2 Proprietary Information Deleted]

[Proprietary Information Deleted]

4.1.3 Clad Ovality Stress

The initial deviation in the shape of the cross-section of a hollow cylinder from perfect circle (with an initial ovality), when the tube is subjected to a uniform external over pressure, gives rise to tangential and axial stresses which may eventually lead to the collapse of the tube. [Proprietary Information Deleted]

[Proprietary Information Deleted]

[Proprietary Information Deleted]

[Figure 4-3 Proprietary Information Deleted]

[Proprietary Information Deleted]

4.1.4 Radial Temperature Gradient Stress

The stresses caused by a radial temperature distribution within the clad can be calculated using standard methods of the theory of elasticity. [Proprietary Information Deleted]

4.1.5 Asymmetric Pellet-Clad Gap Temperature and Stress

If the fuel pellet is located eccentrically in the cladding tube, azimuthal variation will exist in the temperature field across the fuel rod. This in turn gives rise to asymmetry in both the clad temperature and clad stresses.

VIK-2 includes a model for calculating the effect of the fuel pellet being asymmetrically located in the clad on the clad temperature distribution. It considers the effect of an axisymmetric gas gap conductance which becomes a function of the azimuthal angle, ϕ, measured with respect to the displacement vector, s, from the tube's center. [Proprietary Information Deleted]

4.1.5.1 Mathematical Formalism

[Proprietary Information Deleted]

4.1.5.2 Thermal Model

[Proprietary Information Deleted]

[Proprietary Information Deleted]

[Figure 4-4 Proprietary Information Deleted]

[Proprietary Information Deleted]

4.1.5.3 Thermal Stresses

[Proprietary Information Deleted]

4.1.6 Springs

The axial stress in the clad caused by the internal and external springs is equal to the resultant of the internal and external spring force divided by the clad cross-section area, i.e., the axial stress becomes

$$\sigma_3 = \frac{F}{A} \tag{4.1-68}$$

where,

$$F = f_i - f_e \tag{4.1-69}$$

$$A = \pi (b^2 - a^2) \tag{4.1-70}$$

f_i = internal spring force [N]

f_e = external spring force [N]

a = clad inner radius [m]

b = clad outer radius [m]

4.1.7 Rod Bending

The stress components in the clad caused by the flow induced vibrations are calculated. [Proprietary Information Deleted]

[Proprietary Information Deleted]

[Figure 4-5 Proprietary Information Deleted]

[Proprietary Information Deleted]

[Proprietary Information Deleted]

[Figure 4-6 Proprietary Information Deleted]

4.1.8 Clad Wall Stresses from Spacer Springs and Supports

The stresses in the clad caused by the spacer consists of spacer membrane, spacer bending and spacer beam bending stresses. Membrane and bending stresses are caused by the spacer springs, and spacer beam bending arises from the bending in the portion of the rod between the spacer end supports. [Proprietary Information Deleted]

[Proprietary Information Deleted]

[Figure 4-7 Proprietary Information Deleted]

[Proprietary Information Deleted]

[Proprietary Information Deleted]

[Figure 4-8 Proprietary Information Deleted]

[Proprietary Information Deleted]

[Proprietary Information Deleted]

[Figure 4- 9 Proprietary Information Deleted]

[Proprietary Information Deleted]

4.1.9 Temperature Gradient at the Bottom End Plug

Thermal strain is generated in the bottom end plug due to the heat transfer from the fuel pellet. This strain in turn loads the cladding on the circumferential weld between the clad and the bottom end plug.

[Proprietary Information Deleted]

4.1.10 End Plug Angle (BWR)

With the most unfavourable tolerances on the tie plate, the non-straightness of the hole in the tie plate and the end plug pin inserted in it, may induce a bending moment in the fuel rod. [Proprietary Information Deleted]

[Proprietary Information Deleted]

[Figure 4-10 Proprietary Information Deleted]

4.2 EQUIVALENT CLADDING STRESSES

4.2.1 General

Both fully recrystallized BWR-type Zircaloy cladding and stress relief PWR-type Zircaloy cladding can be treated by VIK-2. The code consists of a number of subroutines. Each subroutine calculates the stress due to the different sources. The stresses are calculated at the clad inner and outer radius at three axial locations;

- at the bottom plenum
- at the spacer
- between two spacers

Depending on the origin of the stress and on geometrical and material discontinuities in the design each stress is classified as general primary membrane (P_m), local primary membrane and bending stress ($P_L + P_b$) or primary and secondary membrane and bending stress (S_{mb}). The calculation of the effective and the allowed stresses for each category and for the different locations can be done according to "The American Society of Mechanical Engineers", ASME Section III Article NB-3000 (Reference 4-10). The effective stress according to ASME III is calculated by the Tresca formula. The safety factor is then calculated by dividing the allowed stress by the maximum effective stress.

The effective stress according to Tresca is given by

$$\sigma_e = \max (|\sigma_1 - \sigma_2| , |\sigma_2 - \sigma_3| , |\sigma_1 - \sigma_3|) \qquad (4.2.1)$$

where σ_1, σ_2 and σ_3 are the stresses in orthogonal directions.

4.2.2 End Plug Stress Concentration

The effective stress at the end plug is calculated in the manner described in Section 4.1.2 [Proprietary Information Deleted]

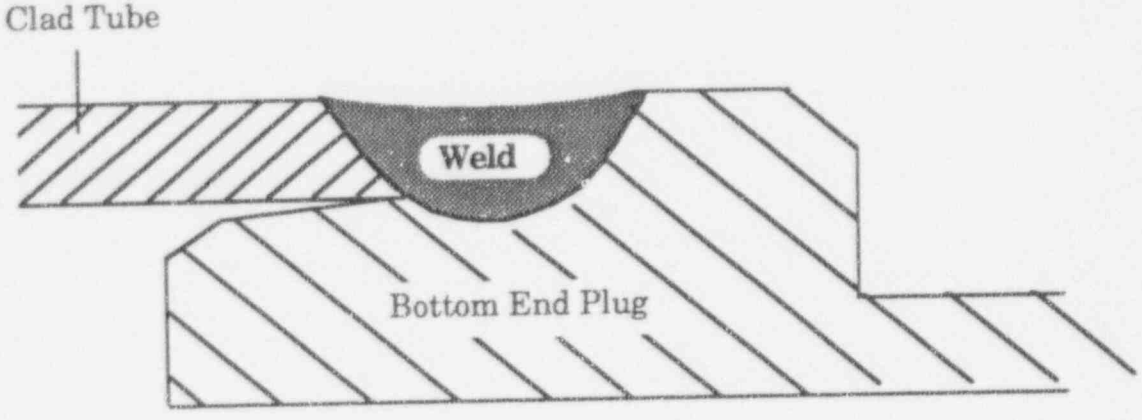

Figure 4-11 Weld at bottom end plug

[Proprietary Information Deleted]

[Figure 4-12a Proprietary Information Deleted]

[Proprietary Information Deleted]

[Figure 4-12b Proprietary Information Deleted]

4.2.3 Allowable Stresses

The design conditions based on ASME III, Article NB-3000 are:

Stress Category	P_m	$P_L + P_b$	$P_L + P_b + P_{mb}$
Allowed Stress	S_1	S_2	S_3

Stress Category

Depending on the origin of the stress and on discontinuities on the design edach stress is classified as:

P_m = primary membrane

$P_L + P_b$ = primary membrane + primary bending

$P_L + P_b + P_{mb}$ = primary and secondary membrane + bending

For each category the effective stress is determined according to the Tresca formula:

$$\sigma_{eff} = \max (|\sigma_1 - \sigma_2|, |\sigma_2 - \sigma_3|, |\sigma_3 - \sigma_1|)$$

where σ_1, σ_2, and σ_3 are stresses in orthogonal directions.

Allowed Stresses

The effective stress from each category is compared with the corresponding allowed stress:

$S_1 = 1.0\ S_m$

$S_2 = 1.5\ S_m$

$S_3 = 3.0\ S_m$

where

$$S_m = \min \begin{pmatrix} R_{p0.2}(20\,^\circ C) / 1.5 \\ R_{p0.2}(T) / 1.5 \\ R_m(20\,^\circ C) / 3 \\ R_m(T) / 3 \end{pmatrix}$$

$R_{p0.2}$ and R_m are the yield and tensile strength at operating temperature T. [Proprietary Information Deleted]

4.3 REFERENCES

4-1 MATPRO-Version II (Revison 2), A Handbook of Materials Properties for Use in the Analysis of light Water Reactor Fuel Rod Behaviour, NUREG/CR-0497, Tree-1280, Rev. 2, August, 1981.

4-2 S. P Timoshenko and J. N. Goodier, *Theory of Elasticity,* Third Edition, Chapter 4, McGraw-Hill Book Company, 1970.

4-3 S. P Timoshenko and S. Woinowsky-Krieger *Theory of Plates and Shells,* Chapter 15, McGraw-Hill, New York, 1970.

4-4 S. P Timoshenko,*Strength of Material,* Third Edition, Chapter V, D. von Nostrand, Princeton, New Jersey, 1950.

4-5 H. S. Carslaw and J. C. Jeager, *Conduction of Heat in Solids,* Second Edition, Chaper VII, Oxford University Press, London, 1959.

4-6 W. H. Jens and P. A. Lottes, "Analysis of Heat Transfer, Burnout, Pressure Drop and Density Data for High Pressure Water," ANL-4627, Argonne National Laboratory, 1951.

4-7 Z. Zudans, T.C. Yen and W.H. Steigelmann, *Thermal Stress Techniques in the Nuclear Industry,* Elsevier, New York, 1965.

4-8 L. D. Landau and E. M. Lifshitz, Course of Theoretical Physics Vol 7, *Theory of Elasticity,* Second Edition, Section 25, Pergamon Press, Oxford, 1970.

4-9 R.J. Roark and W.C. Young, *Formulas for Stress and Strain,* Fifth Edition, Chapter 12, McGraw-Hill, New York, 1975.

4-10 Boiler and Pressure Vessel Code, ASME III, Section III, Article NB 3000 - Design, 1989.

5 VIK-2 CODE QUALIFICATION

5.1 INTRODUCTION

VIK-2 is a static program for calculation of stresses at one fixed time point. Since most of the VIK-2 formulation is based on classical stress-strain analysis, little code qualification is necessary.

The VIK-2 input parameters are described below in Section 5.2. Examples of the typical VIK-2 analysis of a Boiling Water Reactor (BWR) fuel rod and of two Pressurized Water Reactor (PWR) fuel rods are given in Section 5.3 and Section 5.4, respectively.

5.2 VIK-2 INPUT DESCRIPTION

The input parameters with the different options, the parameter format for each card type and the line number where the input card should be specified are given below to assist in interpreting sample cases provided in Sections 5.3 and 5.4.

Proprietary Information Deleted

5.3 EXAMPLE OF BWR ANALYSIS

5.3.1 BWR Input Example

Case 1 presented here is a BWR fuel rod for a SVEA-96 fuel assembly. The sample calculation is done in compliance the German KTA 3103 part B code. The intent is only to illustrate the application of the VIK-2 code.

The German KTA 3103 Part B code defines stress categories in the same way as the American ASME Section III Article NB-3000 (see Section 4.2.3) except that the von Mises effective stress is used:

$$\sigma_{eff} = \frac{1}{\sqrt{2}}\left[(\sigma_1 - \sigma_2)^2 + (\sigma_2 - \sigma_3)^2 + (\sigma_3 - \sigma_1)^2\right]^{1/2}$$

and that the allowable stresses are:

$S_1 = \min (0.90\ R_{p0.2},\ 0.5\ R_m)$

$S_2 = \min (1.35\ R_{p0.2},\ 0.7\ R_m)$

$S_3 = \min (2.70\ R_{p0.2},\ 1.0\ R_m)$

$R_{p0.2}$ and R_m are the yield and tensile strength at operating temperature. [Proprietary Information Deleted]

TABLE 5.3-1 CASE 1 - SVEA-96 BWR EXAMPLE INPUT

Proprietary Information Deleted

[Proprietary Information Deleted]

5.3.2 BWR Output Example

[Proprietary Information Deleted]

5.4 EXAMPLES OF PWR ANALYSIS

5.4.1 PWR Input Examples

TABLE 5.4-1 CASE 2 - 16x16 PWR ROD WITH ONE PLENUM EXAMPLE INPUT

Proprietary Information Deleted

[Proprietary Information Deleted]

TABLE 5.4-2 CASE 3 - 16x16 PWR ROD WITH TWO PLENA EXAMPLE INPUT

Proprietary Information Deleted

[Proprietary Information Deleted]

5.4.2 PWR Output Examples

PWR Case 2 (3 pages) and Case 3 (3 pages) example output are given below.

[Proprietary Information Deleted]

6 COLLAPS-II COMPUTER CODE DESCRIPTION

This section describes the algorithms used in the COLLAPS-II code. COLLAPS-II computes ovality of the fuel cladding tube as a function of time during reactor operation. The calculation method is based on a natural, reference-independent, geometrical description of arc deformation. The solution is obtained from integral equations instead of the traditional differential equations.

A brief overall summary of the COLLAPS-II code is also given in Section 7.1.

6.1 INTRODUCTION

6.1.1 Background

Fuel rod failure due to cladding creep collapse into an axial gap that may result from fuel densification must be considered. It is well-known that a tube with any initial deviation from a circular shape gives rise to bending stresses in the tube wall, causing further deformation from its initial circular shape. Portions of the tube wall will have bending stresses greater than the mean hoop stress, and at an elevated temperature these portions will creep at rates higher than the mean creep rate, causing further ovality deformation. The increase in tube deformation increases the bending stresses producing still greater creep rates which may cause the tube to enter an unstable mechanical state. In time, this may lead to a complete collapse of the tube.

It should be noted that this collapse mode can occur in any tube undergoing creep deformation even though the external overpressure is below the elastic critical collapse pressure of the tube. In general, however, collapse does not occur in fuel pins. This is because the occurrence of large axial pellet-pellet gaps is rare. The excellent resintering stability of modern fuel essentially eliminates significant gap formation. Also, the neutron flux in the fuel rod plenum region is substantially lower than in the region of the cladding along the active fuel length. Thus, very low creep rates are experienced in this region.

Conservative assumptions are used in the collapse analysis for operating BWR fuel rods. These assumptions are summarized below:

(1) Large axial gap,

(2) 95% limit on initial clad ovality cumulative probability function,

(3) Minimum clad wall thickness,

(4) Combination of worst case of fast neutron flux, clad temperature,

(5) Net pressure determined from external pressure minus initial internal pressure, and

(6) Neglect the end effects of a closed tube.

The computer program COLLAPS-II was developed for this purpose. The mathematical formulation of the COLLAPS-II program is presented here.

6.1.2 Basic Assumptions and Definitions

The following eight items are the basic assumptions and definitions incorporated in COLLAPS-II:

[Proprietary Information Deleted]

6.1.3 The Stress Resultants

[Proprietary Information Deleted]

6.1.4 Axial Strain ε_z

[Proprietary Information Deleted]

6.2 INTEGRATION OF EQUILIBRIUM EQUATIONS

In the mechanical equilibrium state, the stress resultants in any section of the arc must be equal to the internal loads obtained from the solution of the equilibrium equations, which provide the distribution of the local moments $M(\zeta)$ and the normal and tangential forces $N(\zeta)$, $Q(\zeta)$ along the arc.

In the statically determined systems, these distributions are defined by the external loads and the geometry of the arc. Such a situation would arise for example in an arc with one end free and the other end clamped.

For the problem under consideration, by virtue of symmetry, the arc representing one quadrant of the tube has to be considered as partly clamped at both ends (points A and B) as shown in Figure 6-3 and 6-4. From the four unknown reactions, M_1, M_2, N_1 and N_2 ($Q_1 = Q_2 = 0$) only three can be found from the overall static equilibrium conditions, thus the problem is indeterminate.

The classical way to set up the equilibrium conditions for the arc is to consider first an infinitesimally short piece of the arc and to establish the equilibrium conditions in the form of three differential equations which have to be satisfied by the three generalized stresses, M, N and Q.

The aim of the algorithms developed in this section is to integrate the equilibrium equations for a specified (thus assumed as known) shape of the midsurface line of that arc plus the value of one of the indeterminate reactions. For this, the moment at point B has been selected.

6.2.1 Equilibrium Equations as a Stress Transfer Matrix

[Proprietary Information Deleted]

6.2.2 Computation of the Generalized Stresses at Mesh-points

[Proprietary Information Deleted]

6.2.3 Boundary Conditions

[Proprietary Information Deleted]

6.3 CALCULATION OF THE NEUTRAL LINE SHAPE FROM GENERALIZED STRAINS

6.3.1 Problem Formulation

Let the curvature $\kappa = \kappa_0 + \beta$ and Jacobian $J = J_0(\zeta)\,[1 + e(\zeta)]$ of a flat curve be two independent functions of the parameter ζ, associated with points lying on that curve. The problem is to find the global description of the curve, $X(\zeta)$, $Y(\zeta)$ - in any chosen coordinate system X, Y.

The coordinates X, Y and Jacobians J, J_0 are expressed in units of the reference radius R_m, while the curvatures κ, κ_0 and β are expressed in units of $1/R_m$.

6.3.2 Existence of the Solution

[Proprietary Information Deleted]

6.3.3 Computation of the Slope Increments $\Delta\phi$

[Proprietary Information Deleted]

6.3.4 Computation of Coordinate Increments ΔX, ΔY

[Proprietary Information Deleted]

6.4 CALCULATION OF THE INDETERMINATE REACTION, M_B

We are now in a position to define the algorithm for the calculation of the indeterminate reaction M_b, the moment at the right end of one quadrant of the arc. M_b is derived in this section from the condition that the total slope increment for the quadrant of the neutral line is equal to $\pi/2$.

6.4.1 The Expression for the Total Slope Increment

[Proprietary Information Deleted]

6.4.2 Evaluation of the Integral I(M)

[Proprietary Information Deleted]

6.4.3 The Additional Boundary Condition

With the use of integral I(M) given by Equation (6.4-13), we are now in the position to write the last missing boundary condition from which the indeterminate bending moment M_1 at $\zeta=0$ is evaluated.

[Proprietary Information Deleted]

6.5 Creep and Solution of the Time-Dependent Collapse Problem

Relations between the generalized strains (the Jacobian J and curvature κ) and the generalized stresses (the bending moments M, M_p and the membrane forces N, N_p) were established in Sections 6.1 - 6.4. For the calculation of the mechanical equilibrium between loads and the cladding deflection, this information was sufficient. The COLLAPS-II calculation begins with an iterative evaluation of this equilibrium state, as described in Section 6.6.

The time dependent solution requires simultaneous updating of fictitious loads M_p, N_p due to creep, and determination of stresses parallel and transverse to the tube for the given moments M, M_p and forces N, N_p. This information then becomes the basis for the calculation of the creep strain increments needed for the updating of M_p and N_p, which are initially set to zero.

The following computations are discussed in detail:

(a) Calculation of elastic stresses from known M, M_p, N, N_p.

(b) Evaluation of associated creep rates and the choice of the time increment Δt.

(c) Calculation of creep strain increments and their integration across the cladding wall to arrive at new values of fictitious loads N_p and M_p.

6.5.1 Elastic Stresses

[Proprietary Information Deleted]

Then

$$\sigma_\theta = \frac{E}{1 - \nu^2} \ (\varepsilon_\theta + \nu \ \varepsilon_z) \tag{6.5-1}$$

$$\sigma_z = \frac{E}{1 - \nu^2} \ (\varepsilon_z + \nu \ \varepsilon_\theta) \tag{6.5-2}$$

from which, according to the von Mises hypothesis, the effective stress is:

$$\sigma_e = \frac{\sqrt{2}}{2} \ [\ (\sigma_\theta^2 + (\sigma_\theta - \sigma_z)^2 + \sigma_z^2 \ ]$$

6.5.2 Strain Increments Due to Creep

The effective creep rate can be generally expressed as

$$d\varepsilon_{ce}/dt = F \ (\sigma, T, \phi) \tag{6.5-3}$$

where F denotes the applied creep correlation function. For Zircaloy, the time dependence of effective creep strain is described by

$$\varepsilon_e = A \ [1-\exp(-t/\tau) \ ]+ Bt \tag{6.5-4}$$

$$\frac{d\varepsilon_{ce}}{dt} = \frac{A}{\tau} \exp(-t/\tau) + B \tag{6.5-5}$$

where A, t, and B are functions of:

T = temperature, K

ϕ = neutron flux (>1 MeV), 10^{20} n/m^2h

σ_e = the effective von Mises stress, MPa

where

$$\varepsilon_e = \frac{\sqrt{2}}{3}\left[(\varepsilon_{cr}-\varepsilon_{c\theta})^2 + (\varepsilon_{c\theta}-\varepsilon_{cz})^2 + (\varepsilon_{cz}-\varepsilon_{cr})^2 \right]^{1/2} \quad (6.5\text{-}6)$$

and ε_{cr}, $\varepsilon_{c\theta}$, and ε_{cz} are the strains in the radial, circumferential, and axial directions.

[Proprietary Information Deleted]

Calculation of creep increments follows now from the Prandtl-Reuss flow rules given by:

$$\frac{d\varepsilon_{c\theta}}{dt} = K(\sigma_\theta - \sigma_m)$$

$$\frac{d\varepsilon_{cz}}{dt} = K(\sigma_z - \sigma_m) \quad (6.5\text{-}7)$$

$$\frac{d\varepsilon_{cr}}{dt} = K(0 - \sigma_m)$$

where

$$K = \frac{3}{2}\,\frac{d\varepsilon_{ce}/dt}{\sigma_e}$$

$$\sigma_m = \frac{(\sigma_\theta + \sigma_z)}{3}$$

6.5.3 The Automatic Time Step Selection

[Proprietary Information Deleted]

6.5.4 Data Preparation for the Next Time-step

[Proprietary Information Deleted]

6.5.5 The Geometry of the Undeflected Line

[Proprietary Information Deleted]

6.6 SUMMARY

6.6.1 Summary of the COLLAPS-II Method

Let us recapitulate the algorithms presented:

[Proprietary Information Deleted]

6.6.2 Comparison of COLLAPS-II and CEPAN Method

6.6.2.1 General

[Proprietary Information Deleted]

6.6.2.2 Derivation of the Strain-Displacement Relations in Local Reference System

A graphical demonstration of the strain-displacement relations is only useful for illustrative purposes. Therefore, an analytical derivation of the strain-displacement relations will be given here.

[Proprietary Information Deleted]

6.6.2.3 The Mathematical Problem of Cylindrical Shell Calculation

The governing equations for a cylindrical shell are summarized in this section. The creep loop is left "open" since it depends on the stipulated creep model.

[Proprietary Information Deleted]

6.7 COLLAPSE CRITERIA

The precise description of the actual process for a complete collapse of a thin oval cylinder is a difficult problem. Nevertheless, in practice a number of conservative criteria have been formulated to predict this collapse. When one of these criteria is encountered during computation the COLLAPS-II computer program signals an appropriate message.

6.7.1 Instantaneous Collapse

[Proprietary Information Deleted]

6.7.2 Creep Collapse Criterion

[Proprietary Information Deleted]

6.7.3 Maximum Ovality Criterion

[Proprietary Information Deleted]

6.8 References

6-1 Supplement 1 to the Technical Report on Densification of General Electric Reactor Fuels, US AEC Reg Staff, Dec 14, 1973.

6-2 O. C. Zienkiewicz, *The Finite Element Method*, p. 363, McGraw-Hill, London, 1977.

6-3 V. I. Smirnov, *A Course of Higher Mathematics*, Vol II, p. 356, Pergamon Press, Oxford, 1964.

6-4 S. Timoshenko, J. M. Gere, *Theory of Elastic Stability*, McGraw-Hill, 1963, (Chapter 7: "Buckling of rings, curved bars and arces", page 278, Chapter 10: "Bending of thin shells", page 440, Chapter 11: "Buckling of shells", page 457).

6-5 I. B. Fiero, "CEPAN Method for Analysing Creep Collapse of Oval Cladding," Vol I, EPRI Report, EPRI NP-3966, April 1985.

6-6 D. G. Franklin, G. E. Lucas, and A. L. Bement, "Creep of Zirconium Alloys in Nuclear Reactors," Appendix IV, ASTM, STP 815, Philadelphia, 1983.

6-7 S. P. Timoshenko, *Strength of Materials:* Part II, D van Nostrand Company, New York, 1964.

TABLE 6-1 M-MATRIX ELEMENTS FOR LINEAR LAGRANGIAN INTERPOLATION

PROPRIETARY INFORMATION DELETED

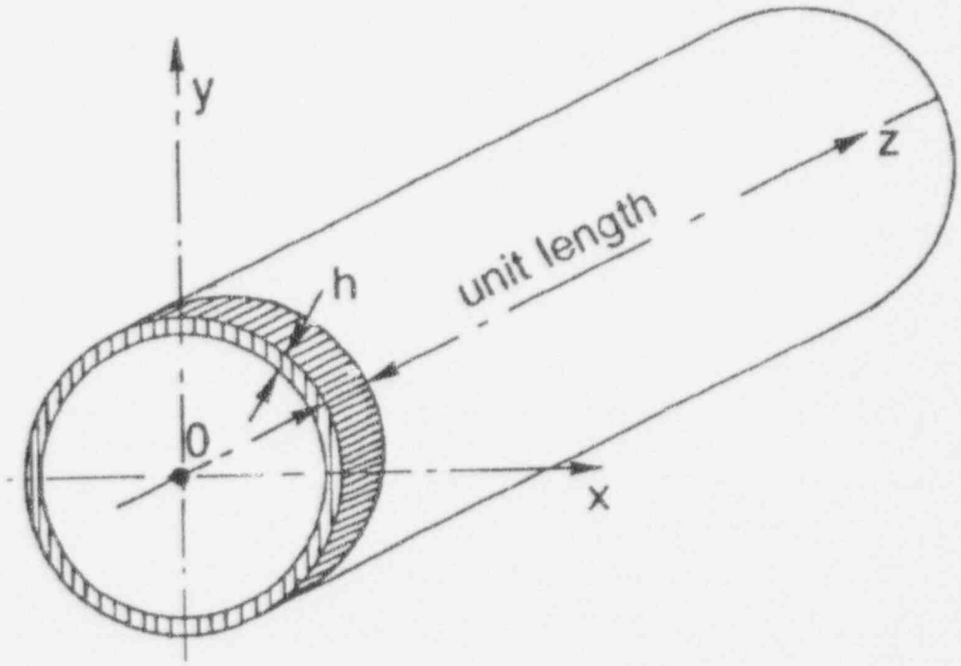

For an infinite cylindrical shell the problem reduces to an arc.

Figure 6-1 Coordinate System

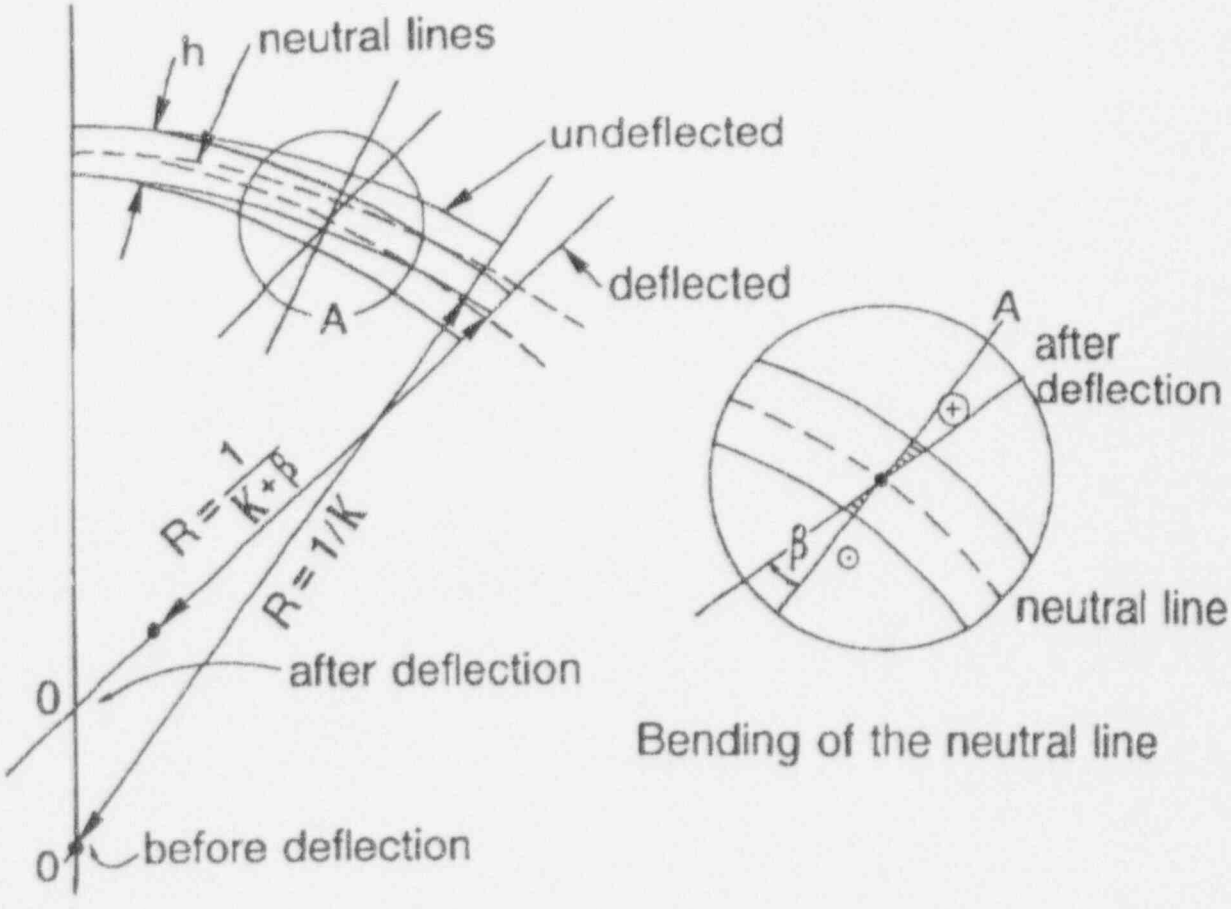

Figure 6-2 Bending of the Neutral Line

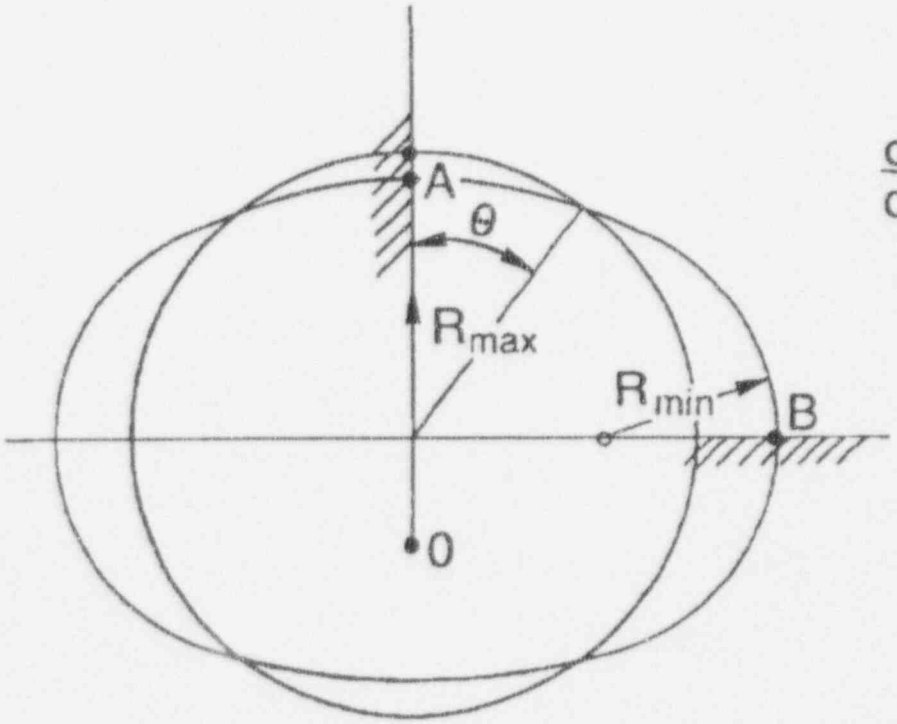

$$\frac{dx}{d\theta} = 0 \quad \text{for } \theta = 0$$

$$\theta = \frac{\pi}{2}$$

Figure 6-3 Definition of Boundary Conditions at Both Ends of the Arc: At A and B curvature should have a zero derivative with respect to the angle θ.

[Proprietary Information Deleted]

Figure 6-4 **Derivation of Equilibrium Conditions of an arc of Finite Length in Local Coordinate System.**

[Proprietary Information Deleted]

Figure 6-5 Definition of Local and Global Characteristic Corrdinate Increments

[Proprietary Information Deleted]

Figure 6-6 **From the conditions of $\frac{d\chi}{d\zeta} = 0$ at point A, B follows that Q_1 and $Q_B = 0$.**

[Proprietary Information Deleted]

Figure 6-7 **Definition of the Slope $\phi(\zeta)$ Function and of Slope Increments per Segment.**

[Proprietary Information Deleted]

Figure 6-8 **Global Cartesian Coordinates of a Mesh-point and Local Variation of these Coordinates.**

[Proprietary Information Deleted]

Figure 6-9 **Relationship Between Global and Local Increments of Coordinates of an Arc of Finite Length.**

7 COLLAPS-II CODE QUALIFICATION

7.1 INTRODUCTION

The computer code COLLAPS-II predicts fuel rod cladding ovality as a function of irradiation time. The code considers the cladding as a long thin cylindrical shell, which is subject to creep under the action of a uniform external pressure. The cross section of the tube is assumed to have a slight initial deviation from circularity. This initial deviation can increase by creep deformation at an increasing rate with time, until the cylinder collapses.

This section briefly reviews the model, provides the cladding creep correlations used in COLLAPS-II, and provides the results of a detailed evaluation of the program. Furthermore, detailed comparisons are made with the NRC approved codes CEPAN and BUCKLE-II.

The COLLAPS-II code computes the ovality variations in a long, slightly oval cylinder due to both elastic and creep deformation. The term ovality, Ω, is defined as the difference between the maximum and the minimum radius in an oval cross section divided by two, that is

$$\Omega = \frac{R_{max}-R_{min}}{2} \qquad (7.1\text{-}1)$$

where R_{max} and R_{min} are the maximum and minimum radius respectively.

[Proprietary Information Deleted]

7.1.1 Model Overview

[Proprietary Information Deleted]

7.1.2 Numerical Solution

[Proprietary Information Deleted]

7.2 CREEP MODEL FOR ZIRCALOY

7.2.1 General

The overall in-pile Zircaloy creep is predominantly a combination of the following mechanisms: thermal creep, irradiation induced creep, and irradiation enhanced creep.

The time dependence of effective creep strain is described by

$$\varepsilon_e = A\,[1-\exp(-t/\tau)\,] + Bt \tag{7.2-1}$$

$$\frac{d\varepsilon_e}{dt} = \frac{A}{\tau}\exp(-t/t) + B \tag{7.2-2}$$

where A, t, and B are functions of:

T = temperature, K

ϕ = neutron flux (>1 MeV), 10^{20} n/m^{2}h

σ_e = the effective von Mises stress, MPa, given by,

$$\sigma_e = \frac{\sqrt{2}}{2}\,[\,(\sigma_1-\sigma_2)^2 + (\sigma_2-\sigma_3)^2 + (\sigma_3-\sigma_1)^2\,]^{1/2} \tag{7.2-3}$$

$$\varepsilon_e = \frac{\sqrt{2}}{3}\,[\,(\varepsilon_1-\varepsilon_2)^2 + (\varepsilon_2-\varepsilon_3)^2 + (\varepsilon_3-\varepsilon_1)^2\,]^{1/2} \tag{7.2-4}$$

where σ_1, σ_2, and σ_3 are the stresses in the radial, circumferential, and axial directions; and similarly, ε_1, ε_2, and ε_3 are the strains in the radial, circumferential, and axial directions. Note that the index c, denoting creep, has been dropped for convenience.

The clad creep strain components can be calculated using the Prandtl-Reuss flow relations given by

$$\varepsilon_i\,(\Delta t) = \frac{3}{2}\,\frac{\varepsilon_e\,(\Delta t)}{\sigma_e}\,S_i\,\Delta t \tag{7.2-5}$$

where

$$S_i = \sigma_i - \frac{1}{3}\sum_{i=1}^{3}\sigma_i \tag{7.2-6}$$

with i = 1, 2, 3

The function A in Equations (7.2-1) and (7.2-2), defines the total accumulated primary creep after a sufficiently long time $t>>\tau$ has elapsed, whereas the function B defines the secondary creep rate.

[Proprietary Information Deleted]

7.2.2 ABB Atom Correlation (NCREEP = 1)

[Proprietary Information Deleted]

7.2.3 Hagrman Correlation (NCREEP = 2)

Hagrman, Reference 7-5, has developed a correlation which is based primarily on end-of-life examination of Zircaloy-4 pressurized water cladding and on out-of-pile measurements of cladding deformations as a function of time. In this correlation the cladding creep strain is a function of cladding temperature, cladding stress, fast neutron flux, and time with:

$$A = 3.47\times10^{-7}\,\sigma\exp(-U/T) \tag{7.2-12}$$

$$1/\tau = 1.87\times10^{-7}\sigma^2\exp(-U/T) \tag{7.2-13}$$

$$B = \frac{3.865\times10^{13}}{T^7}\exp(-5000/T)\,\sigma\,\phi^{0.65} \tag{7.2-14}$$

where,

$$U = 214.27+T\,[\,-0.5324 + T(1.17889\times10^{-4}+3.3486\times10^{-7}\,T\,)\,] \tag{7.2-15}$$

Figure 7-2 shows the calculated creep strain as a function of time for hoop stresses of 50 MPa and 100 MPa at a temperature of 350 °C and fast neutron flux of 2.5×10^{21} /m^{2}h for the Hagrman correlation.

7.2.4 CEPAN Correlation (NCREEP = 3)

ABB uses a correlation for PWR application in the CEPAN code, Reference 7-6, which applies to Zircaloy-4 under biaxial and in-reactor conditions,

$$A = 1.54383\times10^{-5}\,\phi^{0.85}\,\sigma^{1.5}\exp\left(\frac{-3019.63}{T}\right) \tag{7.2-16}$$

$$B = 8.07379\times10^{-9}\,\phi^{0.85}\,\sigma^{1.5}\exp\left(\frac{-3019.63}{T}\right)$$

$$+1.3\times10^{-9}\sinh(0.0130534\sigma)\exp\left[\frac{(38248.6-23.3579\sigma)}{T} - 59.867212\right] \tag{7.2-17}$$

$$1/\tau = 3.6\times10^{-3} \tag{7.2-18}$$

Figure 7-3 shows the calculated creep strain as a function of time for hoop stresses of 50 MPa and 100 MPa at a temperature of 350 °C and fast neutron flux of 2.5×10^{21} /m^2h for the CEPAN correlation.

7.2.5 Creep Hardening Rules

7.2.5.1 Definitions

Creep data are mostly obtained at constant stress and temperature. The application issue that typically arises is how these data can be applied to the case where load is varying with time. The two cumulative creep laws (hardening rules) are defined.

Time Hardening Rule

The time hardening rule assumes that the creep rate depends upon the time from the beginning of the creep process as shown in Figure 7-4. According to the time hardening rule when the state of creep changes, i.e. the temperature, the stress, and the fast neutron flux, the corresponding creep curve is shifted vertically to reach the new state at the same time point.

Strain Hardening Rule

The strain hardening rule assumes that in going from one load level to another the creep rate depends on the existing strain in the material as shown in Figure 7-5. According to the strain hardening rule, the creep states with the same accumulated strain are comparable. This means that when a creep state changes, the next creep curve is reached by shifting horizontally until the associated curve with the same accumulated creep strain is reached.

[Proprietary Information Deleted]

7.2.5.2 Creep Hardening in COLLAPS-II

[Proprietary Information Deleted]

7.3 Qualification of COLLAPS-II

The code COLLAPS-II has been used to study the collapse behavior of a cladding tube under varying conditions of loads and geometry. The code has been compared with the Nuclear Regulatory Commission approved codes CEPAN (Reference 7-6) and BUCKLE-II (Pankaskie, Reference 7-7) for a number of parametric studies. In addition the cladding ovality in mechanical equilibrium (no creep) has been verified by the exact analytical solution of this problem. [Proprietary Information Deleted]

[Proprietary Information Deleted]

7.3.1 Selection of Initial Parameters

A number of parameters controlling the program have to be selected by the user before a given physical situation can be calculated. These parameters are gathered on a special input file, and once being set, are always automatically introduced as "background input".

The most important parameters are:

[Proprietary Information Deleted]

[Proprietary Information Deleted]

7.3.2 Discussion of the Effect of Meshing

7.3.2.1 The Effect of DEPSM, the Maximum Allowed Creep Increment

[Proprietary Information Deleted]

7.3.2.2 The Effect of NG, the Number of Gaussian Points

The number of Gaussian points slightly affects the time-to-collapse. This effect is shown below:

Proprietary Information Deleted

where the standard case is marked by the symbol (*).

[Proprietary Information Deleted]

7.3.2.3 The Effect of NOD, the Number of Circumferential Nodal Points

The time to collapse also depends on the number of circumferential nodal points, as can be seen from the table below:

[Proprietary Information Deleted]

7.3.3 The Ovality in Mechanical Equilibrium

[Proprietary Information Deleted]

7.3.4 Comparison of Collapse Times

[Proprietary Information Deleted]

7.3.4.1 The Effect of Neutron Flux

By varying only the fast neutron flux (> 1 MeV) and keeping the remaining parameters constant, the results in Table 7-5 are obtained.

In Figure 7-10 time-to-collapse versus fast neutron flux is plotted.

7.3.4.2 The Effect of External Pressure

In this section the effect of the external pressure on the time-to-collapse is evaluated. The selected pressures and corresponding collapse times are listed in Table 7-6.

Figure 7-11 shows time-to-collapse as a function of external tube pressure. [Proprietary Information Deleted]

7.3.4.3 The Effect of Temperature

The effect of varying the temperature on the time-to-collapse in the standard case is shown in Table 7-7.

These values are also displayed in Figure 7-12.

7.3.4.4 The Effect of Initial Ovality

The results of varying initial ovality on the time-to-collapse are in Table 7-8.

[Proprietary Information Deleted]

7.3.4.5 The Effect of the Outer Radius

In this section the effect of the outer clad radius on the collapse time is evaluated. The selected outer radii and corresponding collapse times are listed in Table 7-9.

Figure 7-14 shows the results listed in Table 7-9.

7.3.4.6 The Effect of Wall Thickness

[Proprietary Information Deleted]

The results are also shown in Figure 7-15.

7.3.4.7 Concluding Remarks

[Proprietary Information Deleted]

7.4 SUMMARY

[Proprietary Information Deleted]

7.5 References

7-1 Y. S. Pan, "Creep Buckling of Thin-Walled Circular Cylindrical Shells Subject to Radial Pressure and Thermal Gradients," J. Applied Mechanics, pg. 209 - 216, March 1971

7-2 Y. C. Fung, *Foundations of Solid Mechanics,* Prentice-Hall, Englewood Cliffs, New Jersey, 1965

7-3 S. P. Timoshenko and S Woinowsky-Krieger, *Theory of Plates and Shells,* Second Edition, McGraw-Hill, New York, 1979.

7-4 S. P. Timoshenko, *Strength of Materials:Part II,* D van Nostrand Company, New York, 1964

7-5 D. L. Hagrman, MATPRO-Version II, "A handbook of material properties for use in the analysis of LWR fuel rod behavior," NUREG/CR-0497, TREE-1280, 1979.

7-6 I. B. Fiero, CEPAN Method of Analyzing Creep Collapse of Oval Cladding Vol I. General Description, EPRI Report, EPRI NP-3966, 1985.

7-7 P. J. Pankaskie, "BUCKLE, an Analytical Computer Code for Calculating Creep Buckling of Tubes under External Pressure," Battelle Pacific Northwest Laboratories, Richland, Washington, 1974.

TABLE 7-1 STANDARD CASE DATA

Proprietary Information Deleted

TABLE 7-2 COLLAPS-II VARIABLE STUDY

Proprietary Information Deleted

The standard case is marked by the symbol (*).

TABLE 7-3
MECHANICAL EQUILIBRIUM OVALITIES VERSUS INITIAL OVALITY

Proprietary Information Deleted

Remark: Ovalities are expressed in units of 10^{-3}
(a), Membrane forces are included
(b), (c) Membrane forces are excluded

TABLE 7-4

TUBE'S FINAL OVALITY VERSUS INITIAL OVALITY IN MECHANICAL EQUILIBRIUM

Proprietary Information Deleted

TABLE 7-5
COLLAPSE TIME VERSUS FAST NEUTRON FLUX

Proprietary Information Deleted

The standard case is marked by the symbol (*).

TABLE 7-6
COLLAPSE TIME VERSUS PRESSURE

Proprietary Information Deleted

The standard case is marked by the symbol (*).

TABLE 7-7
COLLAPSE TIME VERSUS TEMPERATURE

Proprietary Information Deleted

The standard case is marked by the symbol (*).

TABLE 7-8
COLLAPSE TIME VERSUS INITIAL OVALITY

Proprietary Information Deleted

The standard case is marked by the symbol (*).

TABLE 7-9
COLLAPSE TIME VERSUS OUTER RADIUS R_O

Proprietary Information Deleted

The standard case is marked by the symbol (*).

TABLE 7-10
COLLAPSE TIME VERSUS WALL THICKNESS

Proprietary Information Deleted

The standard case is marked by the symbol (*).

[Proprietary Information Deleted]

Figure 7-1 **BWR Zircaloy cladding creep deformation at different constant stress levels as a function of time for a constant fast neutron flux (≥ 1 MeV) of 2.5×10^{21} n/m^{2}h, using the ABB Atom creep correlation.**

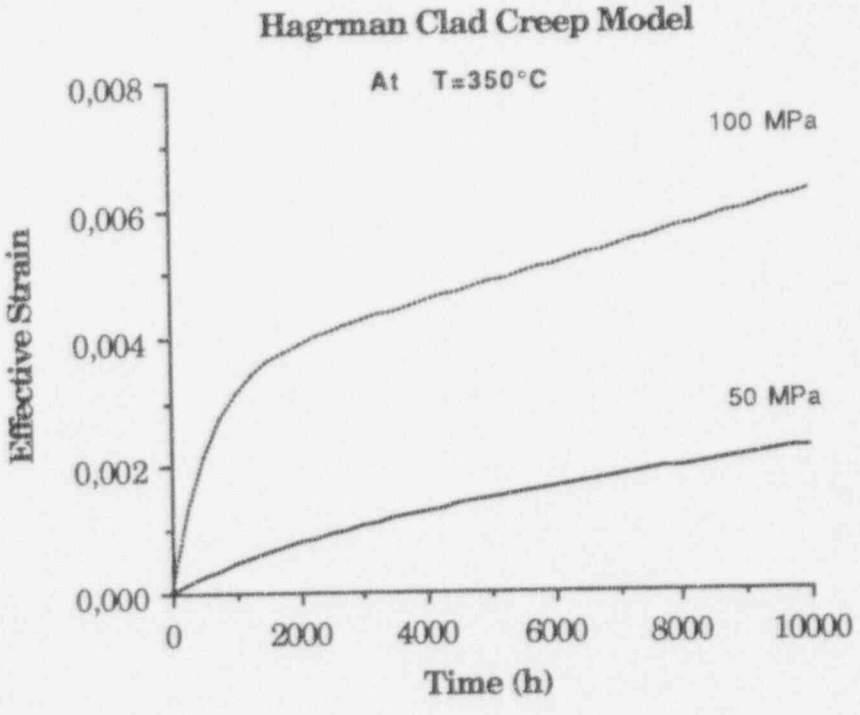

Figure 7-2 Zircaloy-4 cladding creep deformation as a function of time at different constant stress levels for a constant fast neutron flux (≥ 1 MeV) of $2.5 \times 10^{21} n/m^2 h$, using Hagrman's correlation.

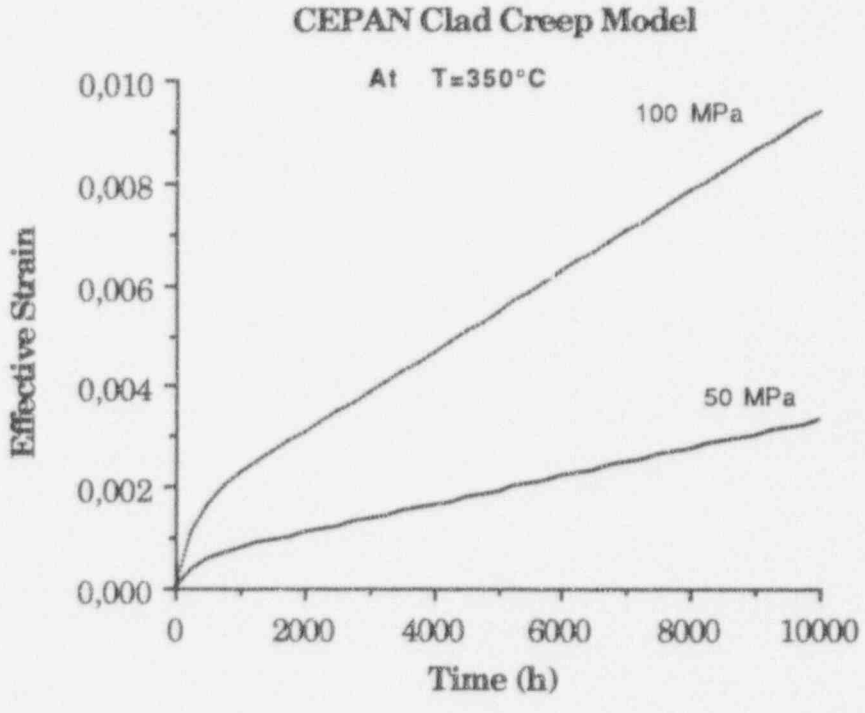

Figure 7-3 Zircaloy-4 cladding creep deformation as a function of time at different constant stress levels for a constant fast neutron flux (≥ 1 MeV) of 2.5×10^{21} n/m^{2}h, using CEPAN's correlation.

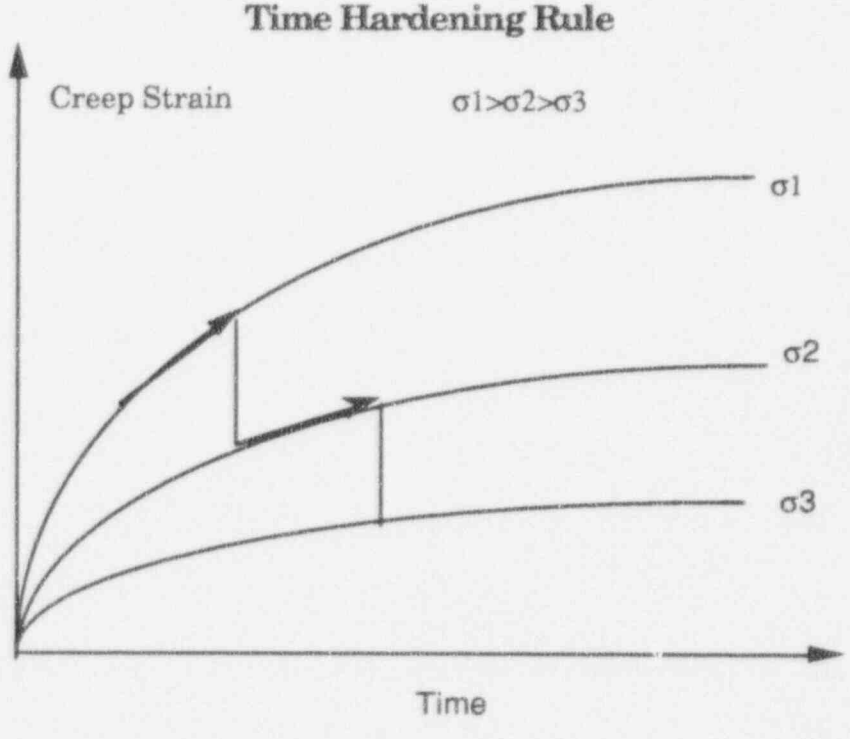

Figure 7-4 Creep strain under load variation obeying time hardening law.

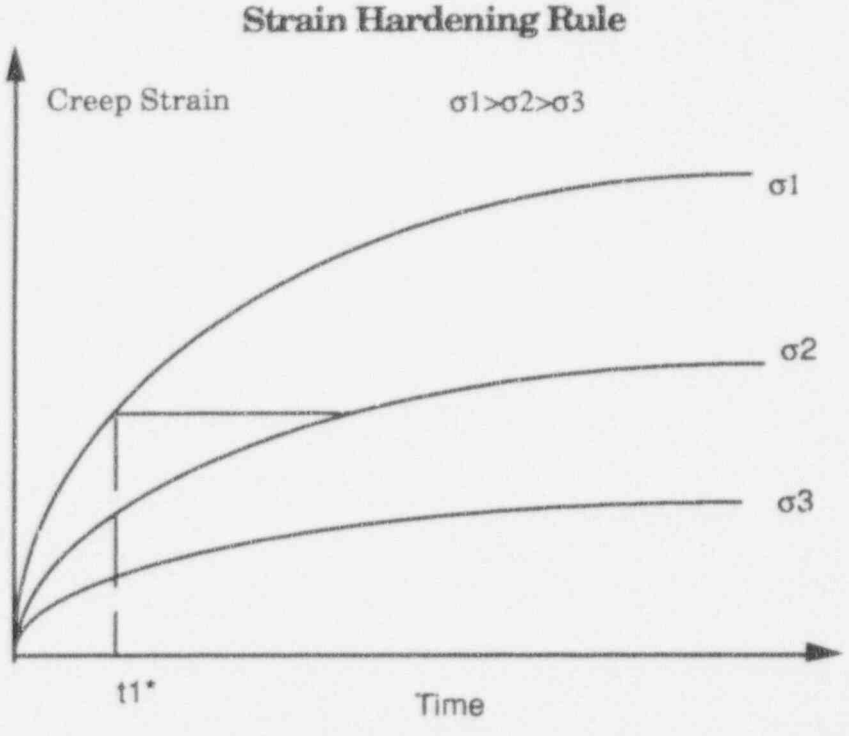

Figure 7-5 **Creep strain under load variation obeying strain hardening law.**

[Proprietary Information Deleted]

Figure 7-6 Resolution of Collapse Time

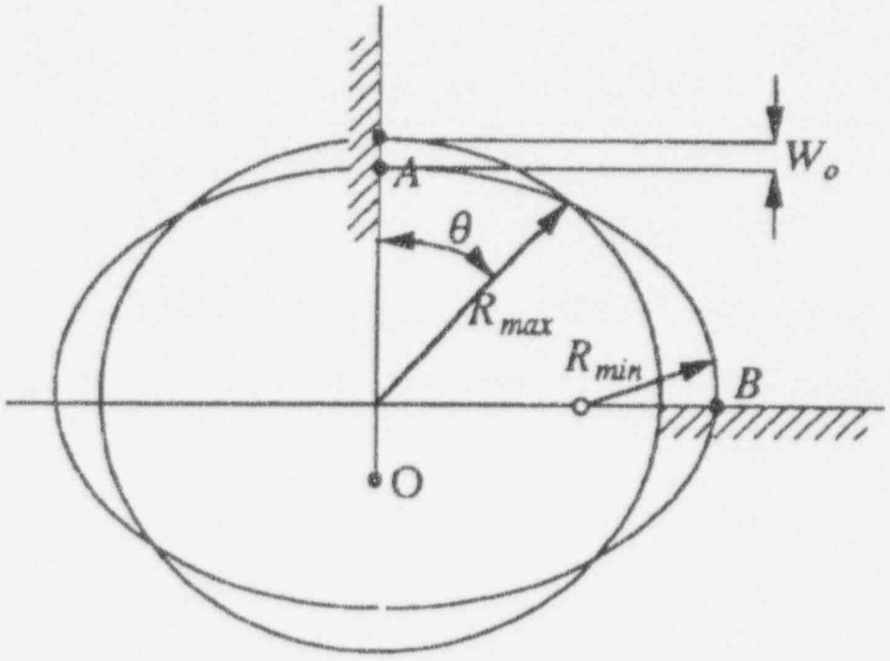

$$R(\theta) = R_m + W_0 \cos 2\theta$$

$$\delta \equiv \frac{W_0}{R_m}$$

$$\frac{R(\theta)}{R_m} = 1 + \delta \cos 2\theta$$

This gives:

$$R_{max} = R_m (1 + \delta)$$

$$R_{min} = R_m (1 - \delta)$$

$$\delta = \frac{R_{max} - R_{min}}{2 R_m}$$

$$R_m = \frac{R_{max} + R_{min}}{2}$$

Figure 7-7 Cross Section of Deformed Tube with Initial Ovality

[Proprietary Information Deleted]

[Figure 7-8 Proprietary Information Deleted]

[Proprietary Information Deleted]

[Figure 7-9 Proprietary Information Deleted]

[Proprietary Information Deleted]

Figure 7-10 Collapse Time versus Fast Flux - Standard Case

[Proprietary Information Deleted]

Figure 7-11 Collapse Time versus Pressure - Standard Case

[Proprietary Information Deleted]

Figure 7-12 Collapse Time versus Temperature - Standard Case

[Proprietary Information Deleted]

Figure 7-13 Collapse Time versus Ovality - Standard Case

[Proprietary Information Deleted]

Figure 7-14 Collapse Time versus Outer Radius - Standard Case

[Proprietary Information Deleted]

Figure 7-15 Collapse Time versus Wall Thickness - Standard Case

[Proprietary Information Deleted]

[Figure 7-16 Proprietary Information Deleted]

APPENDIX A

THERMAL PROPERTIES

A THERMAL PROPERTIES

A.1 Fuel Rod Pellet Thermal Properties

A.1.1 Thermal Conductivity

The thermal conduction in UO_2 consists of the sum of two contributions, conduction through lattice vibrations (phonons) and conduction by electronic processes (Reference A-1).

$$K(T) = K_{ph} + K_{el} \tag{A-1}$$

where K(T) is the total thermal conductivity of the solid, K_{ph} is the phonon thermal conductivity, and K_{el} is the electronic thermal conductivity.

The thermal conductivity due to phonons is expressed by the Debye formula for dielectric solids (Reference A-2):

$$K_{ph} = \frac{1}{3} C v l \tag{A-2}$$

where C is the heat capacity of the phonons, v is the phonon velocity, and l is the phonon mean free path. The phonon mean free path depends on various phonon scattering processes: collisions between different phonons, collision of phonon with crystal boundary, and by lattice imperfections. The phonon-phonon interaction makes l to be proportional to the inverse of temperature 1/T, whereas the interaction of phonons with lattice imperfections relates l with the defect concentration. Thus the thermal resistivity (inverse of thermal conductivity) due to phonons can be expressed by:

$$\frac{1}{K_{ph}} = R_0 + \sum_{i=1}^{n} A_i x_i + B\,T \tag{A-3}$$

where R_0 is the resistivity of the perfect crystal lattice at absolute zero temperature, $A_i x_i$ is the resistivity associated with the defect type i, with concentration x_i, and B T is the phonon-phonon interaction contribution to resistivity.

The lower limit of l ($\propto$ 1/T) limits the phonon conductivity up to a temperature T_0 around 2,000 K (Reference A-3).

The electronic conductivity, K_{el}, of UO_2 can be expressed using Hyland's recommendation (Reference A-1):

$$K_{el} = \frac{1}{4}\left[\frac{u}{e}\right]^2 \frac{\sigma(T)}{T} \quad \text{(A-4)}$$

where u (in eV) is the energy required to create charge carriers, e is the electron charge, and $\sigma(T)$ is the intrinsic electrical conductivity expressed by (Reference A-4).

$$\sigma(T) = \sigma_0 \exp(-Q/T) \quad \text{(A-5)}$$

In conclusion, present models lead to the following five parameter description of UO_2 thermal conductivity:

$$K = \frac{1}{A+BT} + \frac{C}{T}\exp(-Q/T) \qquad T < T_0 \quad \text{(A-6)}$$

$$K = \frac{1}{A+BT_0} + \frac{C}{T}\exp(-Q/T) \qquad T \geq T_0 \quad \text{(A-7)}$$

where T_0 is determined experimentally.

UO_2 Fuel

In STAV6.2 the parameters of the thermal conductivity of the dense UO_2 material, defined as K_0 are taken from the work of Reymann (Reference A- 5),

$$K_0 = \frac{1}{0.1149+0.00025\,T} + 0.01216\exp(0.001867\,T) \quad T<1650°C \quad \text{(A-8)}$$

$$K_0 = 1.91 + 0.01216\exp(0.001867\,T) \quad T\geq 1650°C \quad \text{(A-9)}$$

where

K_0 = thermal conductivity of dense material (W/m°C)

T = temperature (°C)

[Proprietary Information Deleted]

[Proprietary Information Deleted]

[Figure A-1 Proprietary Information Deleted]

Gadolinia Fuel

Thermal conductivity of unirradiated gadolinia-urania has been a subject of several measurements (References A-7 through A-11). In these studies the laser-flash technique is used to measure the thermal diffusivity of the material. In this method a short-duration (about 1 ms) of heat pulse from a laser is deposited on one face of the slab sample and then the temperature rise as a function of time in the opposite face of the sample is monitored. Diffusivity, h, is then calculated from thickness of the slab sample and half-time of temperature rise.

Having determined h the thermal conductivity, κ, is calculated using the relation:

$$\kappa = h\, C_p\, \rho \qquad \text{(A-13)}$$

where ρ is the material density and C_p is the heat capacity of the material at constant pressure. In References A-7, A-9, A-10, and A-11 heat capacities were calculated by combining the data of UO_2 and Gd_2O_3 using the thermodynamic rules of mixture. On the other hand, in Reference A-8, the DOE work, calorimetric measurements were made to determine specific heat of the UO_2-Gd_2O_3 samples as a function of temperature.

[Proprietary Information Deleted]

[Proprietary Information Deleted]

[Figure A-2 Proprietary Information Deleted]

[Proprietary Information Deleted]

[Figure A-3 Proprietary Information Deleted]

[Proprietary Information Deleted]

[Figure A-4 Proprietary Information Deleted]

[Proprietary Information Deleted]

[Figure A-5 Proprietary Information Deleted]

[Proprietary Information Deleted]

[Figure A-6 Proprietary Information Deleted]

A.1.2 Heat Capacity

The heat capacity is an auxiliary calculation performed in STAV6.2 for input into transient analysis fuel response calculations. The fuel pellet specific heat capacity of a solid at room temperature and above are well described by Einstein's model (Reference A-2)

$$C_V = \frac{A\theta^2 \exp(\theta/T)}{T^2 [\exp(\theta/T)-1]^2} \quad \text{(A-16)}$$

where,

C_V = specific heat capacity at constant volume (J/kgK)

A = 290.7 (J/kgU)

θ = the Einstein temperature = 535.285 (K)

In reactor applications, the specific heat at constant pressure is of interest. The relationship between the two is given by:

$$C_p = C_V + \left(\frac{\alpha^2 V}{\beta}\right) T \quad \text{(A-17)}$$

where α is the temperature coefficient of linear expansion, V the volume, and β the isothermal compressibility.

For UO_2

$$C_p = C_V + b\,T \quad \text{(A-18)}$$

with $b = 2.43 \times 10^{-2}$.

Above the temperatures of about 1500 K, the specific heat data show a rapid rise not described by Equation (A-18). This rise is attributed to the energy necessary to form *Frenkel pairs* (equal numbers of vacancies and interstitials) and even *Schottky pairs* (equal numbers of positive and negative ions), Reference A-12. The enthalpy of formation of these defects is given by (Reference A-5):

$$H_D = k \exp(-E_D/RT) \quad \text{(A-19)}$$

where

H_D = defect energy contribution to the enthalpy

E_D = activation energy for Frenkel pairs

= 1.577×10^5 (J/mol)

R = 8.3143 (J/mol K)

k = 8.745×10^7 (J/kg)

The derivative of Equation (A-19) with respect to temperature gives the specific heat for defect formation:

$$C_D = \frac{kE_D}{RT^2} \exp(-E_D/RT) \qquad \text{(A-20)}$$

Combining Equations (A-16), (A-18) and (A-20) gives the specific heat for UO_2 in the temperature range of 273 K to 2800 K:

$$C = Cp + C_D$$

$$C = \frac{A\theta^2 \exp(\theta/T)}{T^2 [\exp(\theta/T)-1]^2} + b\,T + \frac{kE_D}{RT^2} \exp(-E_D/RT) \qquad \text{(A-21)}$$

According to Reymann's analysis (Reference A-5) the standard error of this correlation is ±3 J/kg. In Figure A-7 the heat capacity of UO_2 fuel as a function of temperature is plotted.

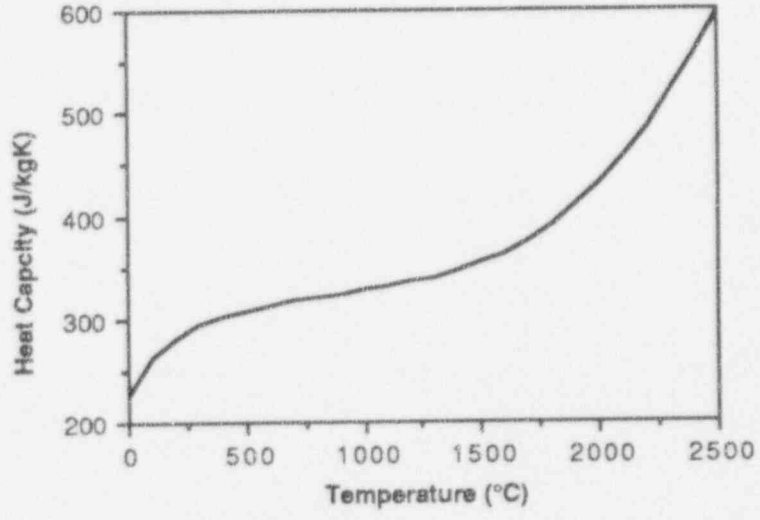

Figure A-7 Heat capacity of UO_2 as a function of temperature.

A.1.3 Thermal Expansion

Since there is a large temperature gradient along the pellet radius, an integral of the pellet thermal expansion coefficient over pellet radius is necessary. A simple linear expansion model for a solid pellet with an infinite number of radial cracks is considered. This reduces to an integral of the coefficient of expansion:

$$(\alpha T)_{pellet} = \frac{\int_0^{R_0} \alpha_T(r)dr}{\int_0^{R_0} dr} = \frac{1}{R_0}\int_0^{R_0} \alpha_T(r)dr \qquad \text{(A-22)}$$

where,

$(\alpha T)_{pellet}$ = pellet thermal expansion, dimensionless

$\alpha_T(r)$ = UO_2 thermal expansion coefficient at radius r

R_0 = pellet outer radius

For annular pellets, the thermal expansion of the hole is added to Equation (A-22).

A coefficient of linear thermal expansion is defined by:

$$\alpha = \frac{1}{L}\frac{dL}{dT} \qquad \text{(A-23)}$$

where L is the length, and dL/dT its derivative with respect to temperature. For temperatures below melting the fractional linear thermal expansion is expressed by a correlation derived by Olsen in MATPRO (Reference A-5):

$$\frac{\Delta L}{L} = -4.972\text{x}10^{-4} + 7.107\text{x}10^{-6}\,T + 2.581\text{x}10^{-9}\,T^2 + 1.140\text{x}10^{-13}\,T^3$$

$$+ 2.581\text{x}10^{-9}\,T^2 + 1.140\text{x}10^{-13}\,T^3 \qquad \text{(A-24)}$$

where,

$\frac{\Delta L}{L}$ = fractional linear thermal expansion ($\alpha_T(r)$ in Equation A-22)

T = temperature, °C

Figure A-8 shows the plot of ΔL/L versus temperature.

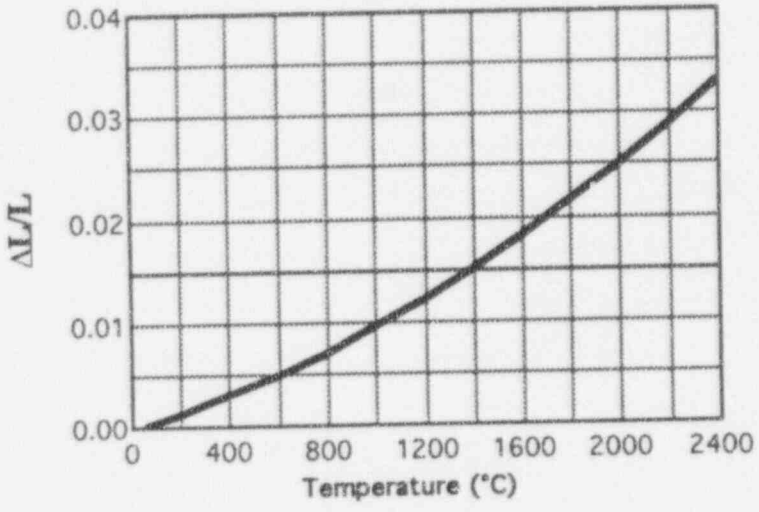

Figure A-8 Temperature dependence of fractional linear thermal expansion of UO_2.

Thermal expansion of UO_2-Gd_2O_3 fuel has been measured by Wada, Noro, and Tsukui (Reference A-11). Their observation was that the thermal expansion coefficient of a UO_2-Gd_2O_3 solid solution can be regarded to be about the same as that of the pure UO_2 in the relatively wide composition range of Gd_2O_3 concentration. [Proprietary Information Deleted]

A.2 Fuel Rod Cladding Thermal Properties

A.2.1 Thermal Conductivity

Thermal conductivity of Zircaloy is primarily a function of temperature. Miller (Reference A-5) has surveyed Zircaloy thermal conductivity data obtained by various workers. The data included both Zircaloy-2 and Zircaloy-4 with various textures and heat treatments. The differences between the materials appeared to be of the same magnitude as the statistical scatter in the data. The data in the range of 20°C to 800°C fit the linear relation:

$$\lambda = 12.6 + 0.0118\,T \qquad \text{(A-25)}$$

where,

λ = thermal conductivity, W/m K

T = temperature, °C

Figure A-9 shows a plot of thermal conductivity (Equation A-25) versus temperature. The uncertainty in the model is about ±1.01 W/mK.

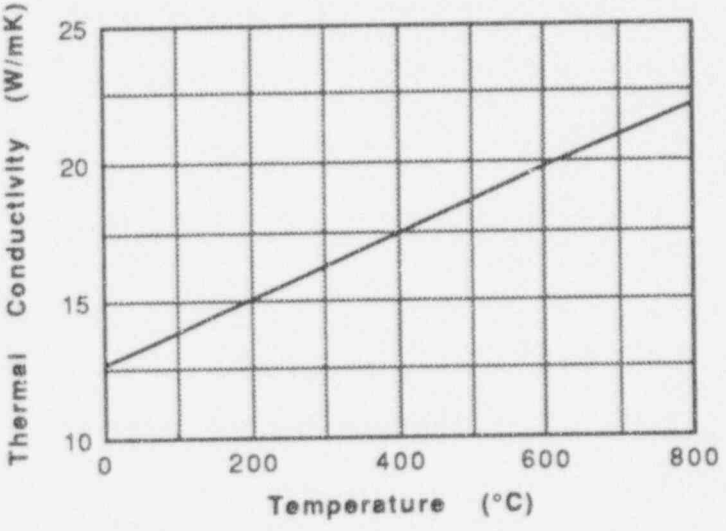

Figure A-9 Thermal conductivity of Zircaloy as a function of temperature in α-phase material.

A.2.2 Heat Capacity

The heat capacity is an auxiliary calculation performed in STAV6.2 for input into transient analysis fuel response calculations. The heat capacity (or specific heat) at constant volume is defined:

$$C_V = \left(\frac{\partial H}{\partial T}\right)_V \qquad \text{(A-26)}$$

where H is the enthalpy and T the temperature. In temperatures above the room-temperature C_V obeys the Dulong and Petit's law, that is, $C_V = 3R$, where R is the universal gas constant R = 8.314 J/mol K. A simple thermodynamic relation gives the heat capacity at constant pressure:

$$C_p = C_V + 9\,\alpha^2\,B\,V\,T \qquad \text{(A-27)}$$

where α is the temperature coefficient of linear thermal expansion, V the volume, and B the bulk modulus.

Zircaloy undergoes a second order phase transition at about 1093 K, from a hexagonal phase (α-phase) to a body centered cubic phase (β-phase). This produces a singularity (a large increase) in the heat capacity in the transition region. In fuel rod design we only model the heat capacity in the α-phase. The model is based on the data provided by Hagrman (Reference A-5).

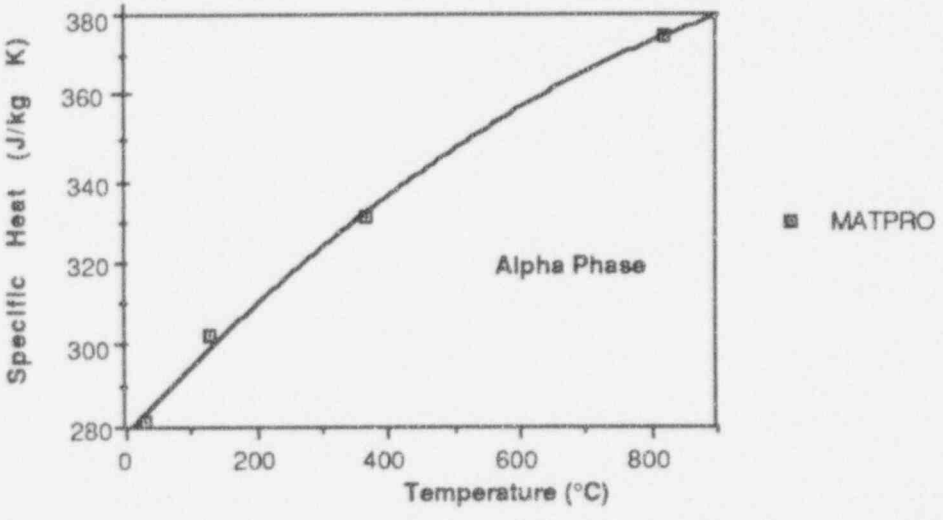

Figure A-10 Zircaloy specific heat as a function temperature, based on the MATPRO data (Reference A-5).

The quadratic fitting of data, Figure A-10, is expressed by:

$$C_p = 278.29 + 0.17117\,T - 6.4925\times10^{-5}\,T^2 \qquad \text{(A-28)}$$

where,

C_p = heat capacity at constant pressure, J/kgK

T = temperature, °C.

Hagrman estimates the standard error of C_p reflecting the systematic error for a random sample of Zircaloy claddings to be ±10 J/kgK (3%) in the α-phase.

A.2.3 Thermal Expansion

The thermal expansion model for Zircaloy cladding is that given by Reymann (Reference A-5). Thermal expansion varies linearly with temperature in the alpha phase ($300 < T < 1073K$) according to:

$$\frac{\Delta L}{L_0} = 4.44 \times 10^{-6} T - 1.24 \times 10^{-3} \quad \text{(A-29)}$$

and

$$\frac{\Delta D}{D_0} = 6.72 \times 10^{-6} T - 2.02 \times 10^{-3} \quad \text{(A-30)}$$

where

$\frac{\Delta L}{L_0}$ = Linear axial strain caused by thermal expansion (unitless)

L_0 = Length at a reference temperature (m)

$\frac{\Delta D}{D_0}$ = Diametral strain caused by thermal expansion (unitless)

D_0 = Diameter of cladding at a reference temperature (m)

T = Temperature (K)

The correlations are obtained by fitting the data of Bunnell et al. (Reference A-13) and adjusting them to give zero expansion at 300°K which is taken to be the reference temperature.

These correlations are plotted in Figure A-11.

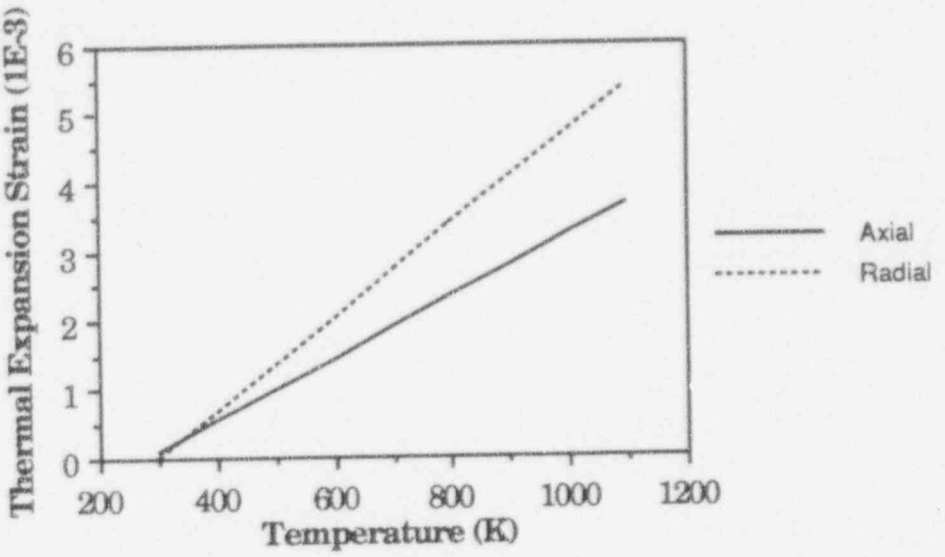

Figure A-11 Thermal expansion of Zircaloy as a function of temperature in axial and radial directions

A.3 Fuel Rod Cladding Elastoplastic Material Properties

In this section the expressions for elastoplastic behavior of Zircaloy cladding are described. The correlations are adopted from the works of Hagrman and Reymann (Reference A-5), and are qualified for ABB BWR type claddings.

In general the elastic moduli are defined by the Hook's law as elements of the fourth-rank tensor which relate the second-rank tensors stress and strain below the yield point. In algebraic form they are expressed:

$$\varepsilon_{ij} = S_{ijkl}\,\sigma_{kl} \qquad \text{(A-31)}$$

$$\sigma_{ij} = C_{ijkl}\varepsilon_{ij} \qquad \text{(A-32)}$$

where S_{ijkl} is the compliance tensor and C_{ijkl} is the elastic stiffness, often called just the elastic constants. Both S_{ijkl} and C_{ijkl} are fourth-rank tensors. For Zircaloy with hexagonal crystal symmetry the components of C_{ijkl} are given by Hagrman (Reference A-5). In STAV6.2 for describing stress-strain relation in the elastic region, the cladding is assumed to be an isotropic material with only two elastic moduli, Young's modulus and the shear modulus.

A.3.1 Zircaloy Cladding Elastic Moduli

Zircaloy cladding elastic moduli mainly depend on temperature, the fast neutron fluence, the amount of cold work and the oxygen content. The following relations are selected (Reference A-5) for the fuel rod design.

The isotropic Young and Shear moduli are modeled by the following relations respectively:

In the α-phase ($T < 1113$ K)

$$E = (1.088\times10^{11} - 5.475\times10^{7}T + C_{E1} + C_3)/C_2 \quad \text{(A-33)}$$

$$G = (4.04\times10^{10} - 2.168\times10^{7}\,T + C_{G1} + C_3)/C_2 \quad \text{(A-34)}$$

in the β-phase ($T > 1113$ K)

$$E = 9.21\times10^{11} - 4.05\times10^{7}\,T \quad \text{(A-35)}$$

$$G = 3.49\times10^{10} - 1.66\times10^{7}\,T \quad \text{(A-36)}$$

where

E = Young modulus for Zircaloy with random texture (Pa)

G = Shear modulus for Zircaloy with random texture (Pa)

T = cladding temperature (K)

C_{E1}, C_{G1} = parameters accounting for the effect of oxidation.

C_2 = parameter accounting for the effect of fast neutron fluence.

C_3 = parameter accounting for the effect of cold work.

The relations used for calculations of C_{E1}, C_{G1}, C_2 and C_3 are

$$C_{E1} = (6.61\times10^{11} + 5.912\times10^{8}T)\Delta \quad \text{(A-37)}$$

$$C_{G1} = (7.07\times10^{11} - 2.315\times10^{8}T)\Delta \quad \text{(A-38)}$$

$$C_2 = 0.88 + 0.12\exp(-\frac{\phi}{10^{25}}) \quad \text{(A-39)}$$

$$C_3 = -2.6\times10^{10}\,Ç \quad \text{(A-40)}$$

where

Δ = kg oxygen/kg Zircaloy, is the average oxygen concentration minus oxygen concentration of as-received cladding.

ϕ = fast neutron fluence, ≥ 1 MeV (neutrons/m^2)

Ç = cold work (unitless ratio of areas)

The standard error for Young's modulus is 6.4×10^9 Pa and for Shear modulus is 9×10^9 Pa.

Using these correlations the temperature dependence of each elastic modulus is plotted in Figure A-12.

[Proprietary Information Deleted]

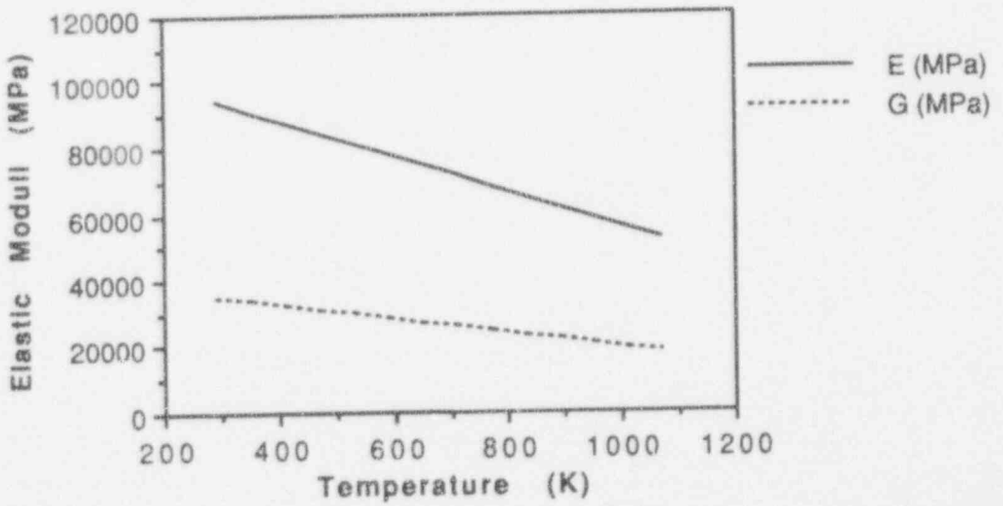

Figure A-12 The elastic moduli of Zircaloy as a function of temperature for unirradiated material with Δ=1200 ppm and Ç=0.

The effect of fast neutron flux on Zircaloy Young's modulus is illustrated in Figure A-13. Figure A-14 illustrates the same effect for the shear modulus.

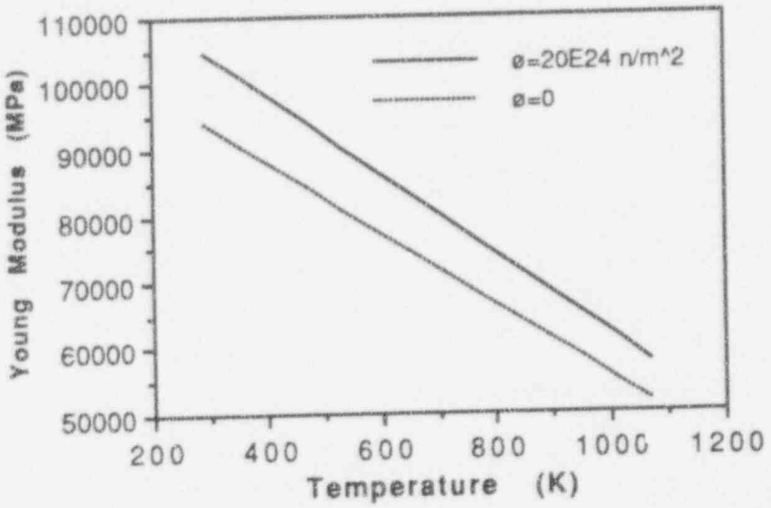

Figure A-13 **Temperature dependence of Young's modulus for irradiated and unirradiated Zircaloy, with Δ=1200 ppm and Ç=0.**

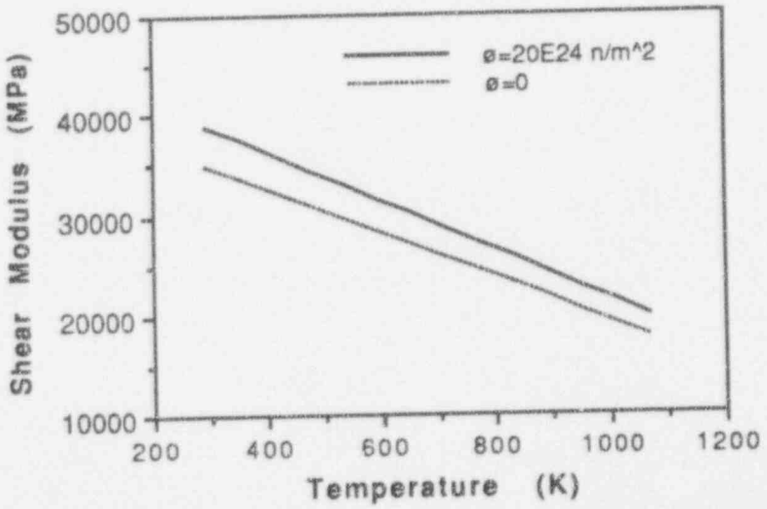

Figure A-14 **Temperature dependence of shear modulus for irradiated and unirradiated Zircaloy, with Δ=1200 ppm and Ç=0.**

A.3.2 Poisson's Ratio

Poisson's ratio for isotropic cladding, ν, is given by

$$\nu = \frac{E}{2G} - 1 \qquad \text{(A-41)}$$

where

ν = Poisson's ratio for isotropic cladding,

G = Shear modulus for Zircaloy with random texture (Pa),

E = Young's modulus for Zircaloy with random texture (Pa).

Figure A-15 shows the temperature dependence of the Poisson's ratio for an unirradiated material.

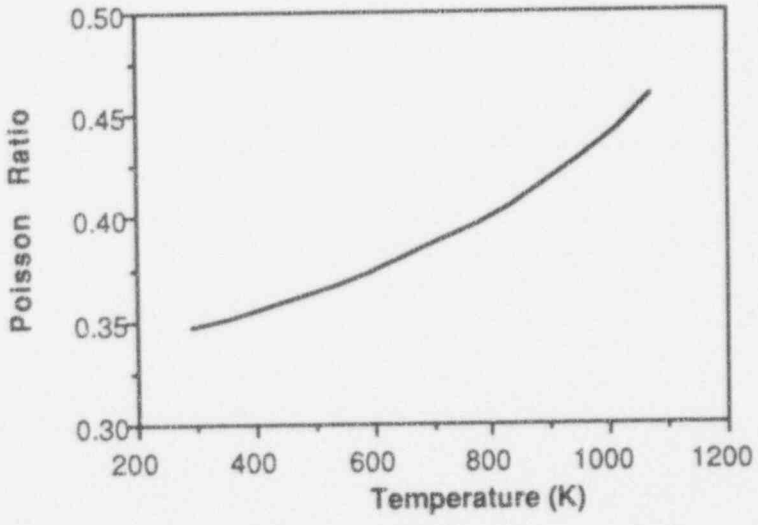

Figure A-15 Temperature dependence of Poisson ratio for unirradiated Zircaloy, with Δ=1200 ppm and Ç=0.

A.3.3 Plastic Stress-Strain Relationships for STAV6.2

[Proprietary Information Deleted]

[Proprietary Information Deleted]

[Figure A-16 Proprietary Information Deleted]

A.3.4 Determination of Yield Strain and Strength

[Proprietary Information Deleted]

[Proprietary Information Deleted]

[Figure A-17 Proprietary Information Deleted]

[Proprietary Information Deleted]

[Proprietary Information Deleted]

[Figure A-18 Proprietary Information Deleted]

A.3.5 Calculation of BOL Zircaloy Yield And Tensile Strength In VIK-2

[Proprietary Information Deleted]

[Proprietary Information Deleted]

Figure A-19 Yield and tensile strengths versus temperature for unirradiated fully recrystallized Zircaloy.

A.4 Fuel Rod Void Gas Properties

A.4.1 Gas Data Used in the Gap Heat Transfer Model

As described in Section 2, the relationship for calculating the thermal conductivity of a monatomic gas mixture is based on the work of Brokaw. K_i^*, the effective conductivity of species, is be calculated by an averaging technique for calculating thermal conductivity of monoatomic and polyatomic gas mixtures, namely:

$$K_i^* = \frac{K_i}{1 + \sum_{j=1}^{n} \psi_{ij}(x_j/x_i)} \qquad \text{(A-64)}$$

where K_i is the thermal conductivity of constituent gas, x the mole fraction, and ψ_{ij} the weighting factor which is a function of molecular weights, temperature, and viscosities

The weighting factor ψ_{ij} is calculated by

$$\psi_{ij} = \phi_{ij}\left[1 + 2.41\,\frac{(M_i - M_j)\,(M_i - 0.142\,M_j)}{(M_i + M_j)^2}\right] \qquad \text{(A-65)}$$

and

$$\phi_{ij} = \frac{\left[1 + \left(\frac{k_i}{k_j}\right)^{1/2} \left(\frac{M_i}{M_j}\right)^{1/4}\right]^2}{2^{3/2}\left(1 + \frac{M_i}{M_j}\right)^{1/2}} \qquad \text{(A-66)}$$

and

n = Number of components in mixture

M_i = Molecular weight of the chemical species i

x_i = Mole fraction of the chemical species i

k_i = Thermal conductivity of the chemical species i

The thermal conductivity equations of the individual rare gases are based on the correlative work of Gandhi and Saxena (Reference A-14).

The thermal conductivities of the gases of interest are listed in Table A-1 and Figure A-20. [Proprietary Information Deleted]

TABLE A-1 GAS PROPERTIES

Gas	Molecular weight	Thermal Conductivity $k=aT^b$ (W/m K)	
		a	b
Helium	4.003	3.366×10^{-3}	0.668
Argon	39.994	3.421×10^{-4}	0.701
Xenon	131.30	4.0288×10^{-5}	0.872
Krypton	83.7	4.726×10^{-5}	0.923
Nitrogen	28.06	2.091×10^{-4}	0.846
Hydrogen	2.016	1.6355×10^{-3}	0.8213

TABLE A-2 ACCOMMODATION COEFFICIENTS

Proprietary Information Deleted

TABLE A-3 TEMPERATURE VARIATION OF GAS VISCOSITIES

Proprietary Information Deleted

TABLE A-4 PRESSURE VARIATION OF G

Proprietary Information Deleted

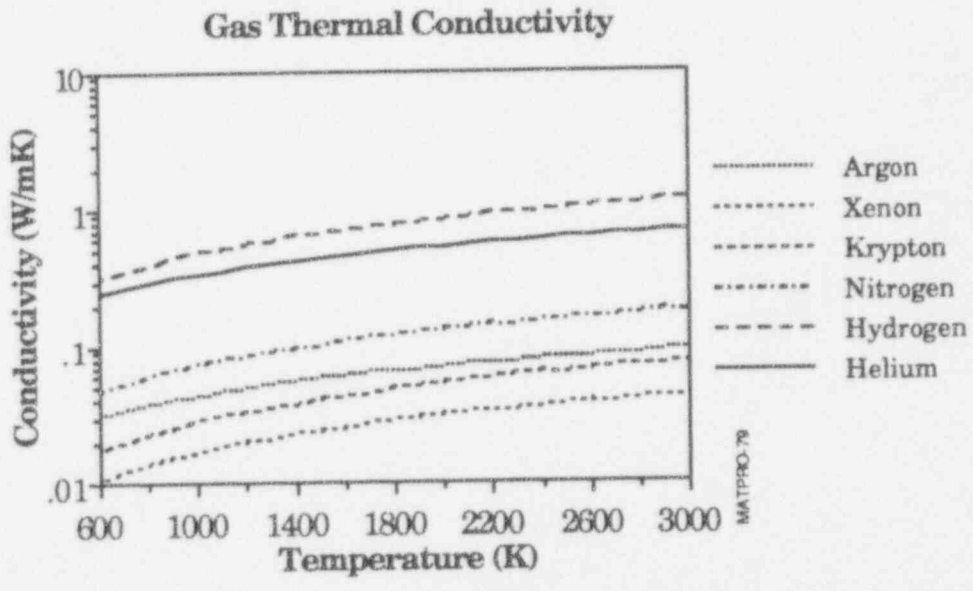

Figure A-20 Fuel Rod Gases Thermal Conductivity with Temperature.

A.5 References

A-1 G. J. Hyland, "Thermal Conductivity of Solid UO_2: Critique and Recommendation," J. Nucl. Mater., Vol. 113, pg. 125-132, 1983.

A-2 C. Kittle, *Introduction to Solid State Physics, 5th Edition*, John Wiley & Sons, New York 1976.

A-3 H. E. Schmidt, Die Warmeleitfaehisgkeit von Uran und Uran-Plutonium Dioxyd bei hohen Temperatren Hi. Temp. Hi. Press. Vol. 3, pg. 345-353, 1971.

A-4 J. C. Killeen, "The Effect of Niobium Oxide Additions on the Electrical Conductivity of UO_2," J. Nucl. Mat., Vol. 88, pg. 185-192, 1980.

A-5 D. L. Hagrman and G. A. Reymann, *MATPRO-version II- A handbook of materials properties for use in the analysis of light water reactor fuel behavior* , NUREG/CR-0497, 1979.

A-6 D. G. Martin, "A Re-appraisal of the Thermal Conductivity of UO_2 and Mixes (U,Pu) oxide fuels," J. Nucl. Mater., Vol. 110, pg. 73-94, 1982.

A-7 S. Fukushima et al, "The Effect of Gadolinium Content in Thermal Conductivity of Near Stoichiometric (U,Gd)O_2 Solid Solution", J. Nucl. Mater., Vol. 105, pg. 201, (1982).

A-8 L. W. Newman, "Development and Demonstration of an Advanced Extended Burnup Fuel Assembly Incorporating Urania - Gadolinia," DOE/ET/34212-36 (BAW-1681-2), August 1982.

A-9 R. H. Watson, "Properties of Urania-Gadolinia System (Part II)," EPRI NP-5862-LD, June 1988.

A-10 R.A. Busch, "Properties of Urania-Gadolinia System (Part I)," Draft, NFIR-RP-03-06D, December 1986.

A-11 T. Wada, K. Noro, and K. Tsukui, "Behavior of UO_2-Gd_2O_3 Fuel," Proceedings of the International Conference on Fuel Performance, British Nuclear Energy Society, 15-19 October 1973, London, England.

A-12 K. Clausen et al., "Observation of Oxygen Frenkel Disorder in Uranium Dioxide above 200 K by use of Neutron Scattering Techniques," Phys. Rev. Lett., Vol. 52, pg. 1238-1241, (1984).

A-13 L.R. Bunnell et al., "High Temperature Properties of Zircaloy-Oxygen Alloys," EPRI NP-524, 1977.

A-14 Gandhi and Saxena, J. Chemical and Engineering Data, Vol. 13, pg. 3, 1968.

A-15 Touloukian, *Thermophysical Properties of Matter*, Plenum, New York, 1976.

APPENDIX B

DISCUSSION OF (U,Gd) O_2 FUEL BEHAVIOUR

ABB

B DISCUSSION OF (U,GD) O_2 FUEL BEHAVIOUR

B.1 Introduction

Over the years ABB has utilized gadolinia as a burnable absorber in standard fuel assemblies for the design of reload cores for both pressurized water reactors (PWRs) and boiling water reactors (BWRs). A typical ABB BWR fuel assembly contains up to about eight Gd-bearing fuel rods. Gadolinia is mixed homogeneously in UO_2 with typical gadolinia contents in the range of 2 to 8 wt%. These rods are essential for optimization of in core fuel management schemes. Therefore for fuel rod thermal-mechanical computations, performed regularly for licensing of fuel reloads, the assessment of $(U,Gd)O_2$ fuel is an essential part of design analysis.

In early life of nuclear fuel operation the gadolinium isotopes ^{155}Gd and ^{157}Gd with neutron absorption cross sections of 61300 b and 255000 b respectively, in thermal energies, transmute to ^{158}Gd with a neutron absorption cross section of 2.4 b. Because of these high absorption cross sections, $(U,Gd)O_2$ "burns" gadolinium practically on fuel surface while fuel interior is completely shielded from thermal neutrons. This effect leads to a gradual shift in time of the interface between burned and unburned gadolinium from fuel pellet surface towards its centre. In this description the fuel pellet is divided into a number of annular rings, where the integral equations for neutron transport are solved in each annulus.

Introducing gadolinia in UO_2 also affects the material properties of the fuel. When Gd_2O_3 is homogeneously mixed with UO_2 the Gd atoms replace the position of U atoms in the fluorite crystal structure of UO_2. Since a Gd atom is lighter than a U atom the theoretical density of $(U,Gd)O_2$ decreases with an increase in gadolinia concentration. However, this effect is partially compensated by the reduction of the lattice parameter which tends to decrease with gadolinia concentration, thereby increasing the $(U,Gd)O_2$ density. Furthermore, the introduction of Gd in UO_2 lowers the thermal conductivity of UO_2 (due to the scattering of phonons with Gd atoms) leading to a higher fuel temperature than UO_2 fuel for the same level of linear heat generation rate.

Also the doping of UO_2 with trivalent atoms such as Gd^{3+} can affect the oxygen vacancy concentration in the material. Matzke (References B-1 and B-2) through ion-bombardment experiments has shown that the effective diffusion coefficient of Xe atoms usually decreases when trivalent ions such as Y^{3+} and La^{3+} are added to the UO_2 material thereby lowering the release rate of Xe atoms. In

analogy with Y^{3+} and La^{3+}, Gd^{+3} ions can also increase the concentration of oxygen vacancies leading to a lower effective diffusion of fission product gases in nuclear fuel.

This appendix describes the modelling of the behaviour of (U, Gd)O_2 fuel during irradiation. The model has been incorporated in the STAV6.2 code. The neutronics part of the model considers neutron energy spectrum in 25 energy groups for the calculation of the cross sections of the nuclei ^{235}U, ^{238}U, ^{155}Gd, ^{157}Gd and ^{239}Pu. Section B.2 presents the neutronics model and the governing equations.

An empirical model to account the effect of Gd^{+3} atoms on fission product gas diffusion has been used to predict the fission gas release of Gd-bearing fuel rods irradiated in BWRs.

B.2 Microburnups Physics

In this section the theory of microscopic burnup (burnup across fuel pellet) is formulated and applied to the initial burnup of a fuel pin with Gd as a burnable absorber. The theory is used for the calculation of power distribution in fuel pellet.

B.2.1 Governing Equations

Let us consider a certain distribution of m isotopes in a region $\tilde{x}$. The number density for isotope j in a medium at time t is specified by a function $N_j(\tilde{x}, t)$. The total macroscopic cross section for the system under consideration $\Sigma_t(\tilde{x}, E, t)$ is given by

$$\Sigma_t(\tilde{x}, E, t) = \sum_{j=1}^{m} \sigma_j(E)\, N_j(\tilde{x}, t) \qquad \text{(B-1)}$$

where $\sigma_j(E)$ is the microscopic cross section of the isotope j which is either annihilated or created during the burnup process.

Provided $\Sigma_t(\tilde{x}, E, t)$ is known the instantaneous neutron flux distribution $\psi = \psi(\tilde{x}, \Omega E, t)$ is determined by solving the Boltzmann equation:

$$\tilde{\Omega} \cdot \nabla \psi + \Sigma_t \psi = \int \Sigma_S(\tilde{x}, E' \rightarrow E, \tilde{\Omega}' \rightarrow \tilde{\Omega}, t)\psi \, dE' d\tilde{\Omega}' + S(\tilde{x}, E, t) \qquad \text{(B-2)}$$

where Σ_S is the scattering cross section and S is the neutron source term.

The subsequent integration of ψ over angles Ω yields

$$\phi(\tilde{x}, E, t) = \int \psi(\tilde{x}, \tilde{\Omega}, E, t)\, d\Omega \tag{B-3}$$

However, due to the presence of neutrons in region $\tilde{x}$, the number density of isotopes, $N_j \equiv N_j(\tilde{x},t)$ obeys a kinetic law (depletion law) given by

$$\frac{\partial N_j}{\partial t} = - N_j R_j(\tilde{x}, t) + \sum_{k \neq j} N_k Y_{kj} R_k(\tilde{x}, t) \tag{B-4}$$

where Y_{kj} is the yield of isotope j when a neutron absorbed by isotope k, and

$$R_j(\tilde{x}, t) = \int_0^\infty \sigma_j(E') \phi(\tilde{x}, E', t)\, dE' \tag{B-5}$$

Equations (B-2) through (B-4) comprise a system of coupled nonlinear equations with m+1 unknowns. Before outlining our strategy for solving this system of equations let us recount the assumptions made when writing down the Equation (B-2).

(i) In the time interval between successive collisions, the cross-sections remain constant, this surmises that when the density function $N_j(\tilde{x}, t)$ is given the neutron flux distribution is established instantaneously.

(ii) The neutron source $S(\tilde{x}, E, t)$ is isotropic. More specifically, the neutron source only emanates from nuclear fission in region $\tilde{x}$:

$$S(\tilde{x}, E, t) = \sum_j \chi(E) \int_0^\infty N(\tilde{x}, E, t)\, \sigma_j^f(E') \phi(\tilde{x}, E, t)\, dE' \tag{B-6}$$

where $\chi(E)$ is the spectrum of the fission neutrons, it is the energy distribution of the neutrons produced by a fission.

(iii) The isotopes are created and annihilated instantaneously in the same spot, that is, the effect of diffusion of isotopes within

the grain is neglected, also the natural decay of isotopes is neglected. These last two assumptions were made when writing Equation (B-4).

The main task of a microburnup program is to find $N_j(\tilde{x}, t)$ for $t > 0$ when the initial distribution $N_j(\tilde{x}, 0)$ is given. Thus the problem is an initial value problem.

B.2.2 Geometry and Boundary Conditions

The fuel assembly is envisaged to consist of pin cells. Each unit cell contains one fuel rod surrounded by moderator (water). The pin-cell with the burnable absorber (Gd_2O_3) fuel consists of three regions, the fuel, the Zircaloy cladding, and the moderator. The fuel is subdivided into n regions (annuli) for computing the isotope concentration $N_j(\tilde{x}_i, t)$, j=1,..., m and i=1, ..., n. The cladding and the moderator are lumped into a single region. The burnable isotopes considered are ^{155}Gd, ^{157}Gd, ^{235}U, ^{238}U and ^{239}Pu. Fission products and other isotopes are not considered and neutron thermalization in the fuel is neglected. The latter assumption means that there is no source term in the fuel, i.e., $S(r, E, t) = 0$ for $r \leq r_0$, where r_0 is the pellet radius.

At the outer unit cell boundary two conditions are assumed:

(I) Zero gradient boundary condition, eigenvalue problem.

The gradient of neutron flux is zero at the boundary, that is

$$\frac{d\psi}{dr} = 0 \quad \text{for } r = R_o \tag{B-7}$$

where R_o is the outer radius of the cell. This condition, Equation (B-7), implies that the cell is immersed into an infinite sea of identical cells. This procedure of using an equivalent cell with zero-gradient boundary condition (ZGBC) is known as the Wigner-Seitz boundary condition.

(II) Isotropic incident flux boundary condition or *fixed source problem.*

For an isolated BA rod (BA rod surrounded by UO_2 rods) the ZGBC is not true. Thus in this case a prescribed in-current of neutrons from the surrounding cells is assumed. The energy spectrum of the incoming neutrons is described by a two parameter distribution

$$J(E) \sim E\, e^{-E/K_B T_n} \quad \text{for } E < E_c$$

$$\sim \frac{A}{E} \quad \text{for } E > E_c \qquad \text{(B-8)}$$

One of the two "free" parameters is the in-current neutron spectrum temperature, T_n, expressed by (Reference B-3): $T_n = T_m (1 + \Delta')$, where T_m is the moderator temperature and Δ' is a dimensionless quantity for the situation under consideration which varies between 0.09 to 0.18. The other free parameter E_c is the transition energy at which the neutron flux changes its Maxwellian distribution to 1/E shape function. The larger the value of E_c the more pronounced is the flux of thermal neutrons compared to the epithermal (E ~ 1eV) neutrons. The value of E_c is chosen to be between 0.2 to 0.6 eV. The constant A appearing in Equation (B-8) is obtained from the continuity condition of current at $E=E_c$.

It should be mentioned that J(E) is normalized to unity. Thus making the transport problem a fixed source problem (in contrast the eigenvalue problem). An eigenvalue problem would emerge if the cell is assumed to obey the ZGBC. In the incoming section the general procedure of solving Equations (B-2) through (B-4) with the considered initial and boundary conditions are outlined.

B.2.3 The Algorithm for Solution of the Transport Equations

The general procedure for solution of the governing equations are summarized as follows

Step 1:

For given isotopic density functions $N_j(\tilde{x})$ compute the macroscopic cross sections $\Sigma(\tilde{x}, E, t)$ via Equation (B-1).

Step 2:

For given macroscopic cross sections, geometry and boundary conditions, solve the transport equation to find the neutron flux (Equations (B-2) through (B-3)).

The energy variable E is discretized to G intervals called groups, ranging from thermal energies (0.025 eV) to fast (fission) energies (100 keV-19MeV). In the present neutronics model the 25-group structure from the ABB Atom code PHOENIX library (Reference B-4, Chap. III) has been used.

To perform this computation the method of collision probability has been utilized. In this method the scalar flux ϕ is obtained accurately in the selected region (annulus) at once. For each group the following linear relation between fluxes in micro regions yields (Reference B-3, Chap. IV)

$$\Sigma_i V_i \phi_i = \sum_{j=1}^{N} P_{ji} \left[C_j \phi_j + \frac{Q_j}{\Sigma_j} \right] + \gamma_i J \qquad \text{(B-9)}$$

where V_i is the volume, Σ_i the total macroscopic cross section, P_{ij} the collision probability which gives the number of collisions at position r_i caused by the source at r_j, $C_j = \frac{\Sigma_{js}}{\Sigma_j}$ (Σ_s = macroscopic scattering cross section), S_j the source density in region j, γ_i the first flight blackness, meaning that the probability that a neutron entering the cell will suffer a collision in that region, and J is the external net current. The index i in Equation (B-9) refers to the region r_i and the energy group index has been suppressed for convenience. The details of solution of Equation (B-9) for ϕ is given by Stammler and Abbate (Reference B-4) and thus are not repeated here.

Step 3:

Integrate Equation (B-5) to find the reaction rates for j=1, ...m. In a discretization scheme the reaction rate for isotope j in the region r_j is calculated as

$$R_j (r_i) = \sum_{g=1}^{G} \sigma_j (g) \phi (r_i, g) \qquad \text{(B-10)}$$

where σ_j (g) is the cross section for isotope j in energy group g.

Having obtained the fluxes belonging to the generation of guessed fission source distribution, the fission source distribution for the next generation is evaluated. The fission source for a given energy group g in a macroregion r_I is

$$S(r_I, g) = \frac{\sum_{j=1}^{m} \sum_{i=1}^{I} dV_i \, N_j(r_i) \, \sigma_j^f(g) \, \phi(r_i, g)}{\sum_{i=1}^{I} dV_i} \qquad \text{(B-11)}$$

where $\sigma_j^f(g)$ is the fission cross section for isotope j in energy group g. Each new generation of neutrons defines a new source and the process is repeated until convergence is attained (outer iteration).

Step 4:

Advance the time t by a time step Δt selected such that the flux distribution remains constant in that time interval. Then solve Equation (B-4), a system of coupled first order ordinary differential equations for $N_j(\vec{x}, t)$.

Step 5:

If the total irradiation time of interest has not been reached return to Step 1 and repeat the steps.

B.2.4 Calculation of the Released Energy

The released energy at each time interval Δt in region i from the depletion of isotope j is obtained by

$$\Delta E_{ij} = e \, dV(i) \left[\int_0^{\Delta t} N_{ij}(t) \, dt \right] R_{ij}^{fiss} \qquad \text{(B-12)}$$

where e is the energy per fission event, V_i the volume of microregion, and R_{ij}^{fiss} the fission rate. It can be shown that

$$\Delta E_{ij} = e \, dV(i)[N_{ij}(0) - N_{ij}(\Delta t)] \, \alpha_{ij} \qquad \text{(B-13)}$$

where

$$\alpha_{ij} = \frac{R_{ij}^{fiss}}{R_{ij}^{abs}} \qquad \text{(B-14)}$$

and R_{ij}^{abs} is the neutron absorption rate. The accumulated energy for the pin

$$Q_{ij} = \sum_{i=1}^{N} edV_i \left[N_{ij}(0) - N_{ij}(\Delta t)\right] \alpha_{ij} \qquad \text{(B-15)}$$

Equation (B-15) can be directly used to calculate the energy released by an isotope without parents. Isotopes that are fissionable are ^{238}U and ^{235}U, while the burnable absorber isotopes are ^{155}Gd and ^{157}Gd. However, the energy release by an isotope such as ^{239}Pu which is created by its parents (^{238}U) and simultaneously fissions (burns) has to be treated differently:

$$\frac{dN_9}{dt} = -N_9 R_9^{abs} + N_8 R_8^{abs} (1 - \alpha_8) \qquad \text{(B-16)}$$

where N_9 denotes the ^{239}Pu number density, R_9^{abs} the absorbtion rate of ^{239}Pu, and $\alpha_8 = \dfrac{R_8^{fiss}}{R_8^{abs}}$ (indices i and j are supressed for convenience).

The solution of Equation (B-16) is written as

$$N_9(t) = N_9(0)\, e^{-R_9 t} + \frac{N_8(0)(1-\alpha_8) R_8^{abs}}{R_8^{abs} - R_9^{abs}} \left[1 - e^{-(R_8 - R_9)t}\right] \qquad \text{(B-17)}$$

Knowing N_8 and N_9 the energy release due to ^{239}Pu fissioning during time interval Δt can be calculated:

$$Q_9 = dV_i\, \alpha_9\, e\left\{N_9(0) - N_9(\Delta t) + (1-\alpha_8)\left[N_8(0) - N_8(\Delta t)\right]\right\} \qquad \text{(B-18)}$$

The power distribution in the fuel pellet region is obtained by

$$P(r_i) = \sum_{j=1}^{m} N_j(r_i)\, R_j^{fiss}(r_i) \qquad \text{(B-19)}$$

The integrated power across the pellet up to a given annulus n will become

$$W(n) = \sum_{i=1}^{n} dV_i \, P(r_i) \qquad \text{(B-20)}$$

where N is the total number of microregions of the pellet.

B.2.5 Eigenvalue Problem

When BA material is almost totally burned out, the considered unit cell becomes nearly critical or even overcritical, the fixed source solution outlined in Section B.2.3 is not applicable (iterative solution diverges). Under such a situation the cell does not obtain neutrons from neighboring cells, meaning that, the net current J = 0. This in turn means that the neighboring cells are all identical. This situation is typical for pin cell calculations for example in the code PHOENIX, (Reference B-4) and can be applied either to BA-free cells or to cells containing up to a maximum of ten percent of the initial BA content. Thus upon depletion of BA material the cell (reactor) can become critical, then the transport Equation (B-2) becomes:

$$\tilde{\Omega} \cdot \nabla \psi + \Sigma_t \psi = \int \Sigma_S (\tilde{x}, E' \rightarrow E, \tilde{\Omega}' \rightarrow \tilde{\Omega}, t) \psi \, dE' d\tilde{\Omega}' \qquad \text{(B-21)}$$

$$+ \frac{\chi(E)}{k} \iint \frac{\nu(\tilde{x}, E')}{4\pi} \Sigma_f (\tilde{x}, E') \psi_k' \, d\tilde{\Omega}' \, dE$$

where k, the effective multiplication factor, is the eigenvalue of Equation (B-21). The smallest eigenvalue is called k_{eff} which is the ratio of the number of neutrons in two successive generations, with the fission process partitioning the generations.

The eigenvalue k_{eff} is computed after each updating of the source term (Equation (B-11), outer iteration) and from the condition that the total number of fissions should be unity:

$$k_{eff}^{l} = \frac{\sum_{I=1}^{N-2} V_i (g) S^{l} (r_i \, g)}{\sum_{I=1}^{N-2} V_i (g) S^{l-1} (r_i, g)} \qquad \text{(B-22)}$$

Here l designates the outer iteration number, and V_i (g) is the volume of the I-th macroregion for the g-th group calculation. The computational procedure is the same as in the fixed source problem

outlined in Section B.2.3 except that $J_{ext} = 0$, and with the evaluation of k_{eff} via Equation (B-22). For BA fuel the fixed source problem is solved first up to a BA concentration of 10% of the initial value, then the computation is switched to the solution of the eigenvalue problem.

The model presented in Sections B.2.1 to B.2.5 has been coded in the computer program BURAS (Burnable Absorber Subroutines).

B.2.6 Comparison with Experiment

There have been several experimental programs for determining the radial burnup distributions and gadolinia isotope distribution across $(U,Gd)O_2$ fuel pellets for different gadolinia concentrations (References B-5 through B-7). For the purpose of this study the data reported by Fuji et al. (Reference B-5) are compared with computations performed with the model presented above.

The considered experiment (Reference B-5) consisted of three test assemblies irradiated in the Hal[illegible]n boiling water reactor with fuel rods bearing gadolinia concentrations up to 9 wt%. Post irradiation examinations performed on samples of the fuel pellets included neutron radiography and mass spectroscopy measurements. The neutron radiography showed that the isotopes ^{155}Gd and ^{157}Gd are symmetrically depleted from pellet outer surface to inner region. The mass spectroscopy analysis for the samples provided isotopic concentration of ^{155}Gd and ^{157}Gd as a function of sample burnup and distributions across the fuel pellet radius. Some of these data are plotted in Figures B1 and B2 plus the results of model calculations for comparison. It is seen that, taking into account the measurement uncertainties, the agreement is quite good.

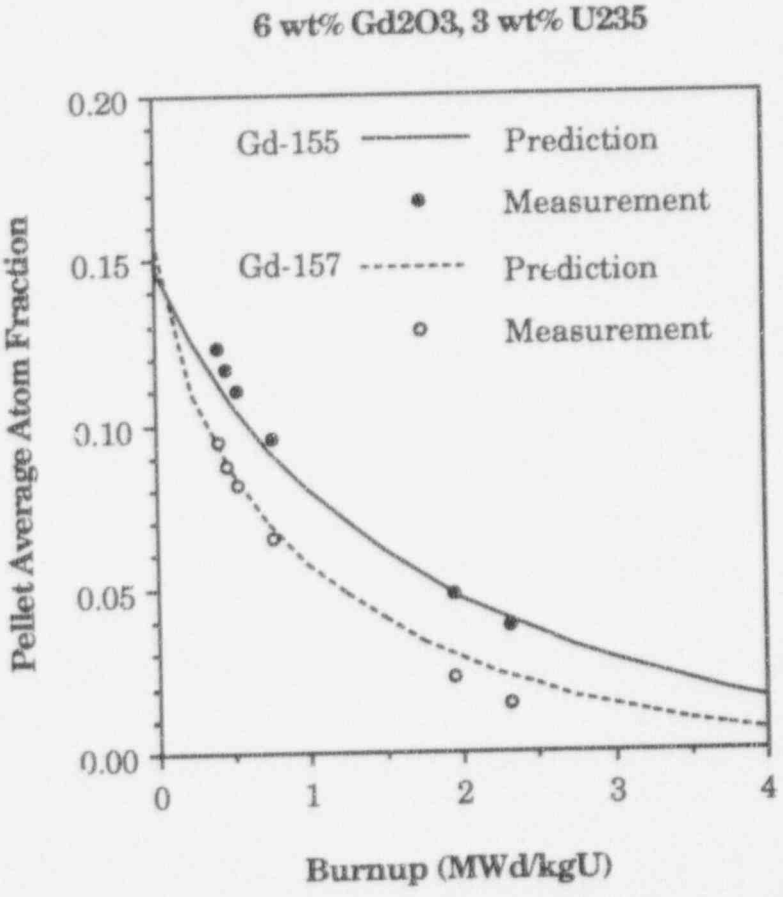

Figure B-1 Comparison between calculated and measured pellet-average atom fractions of ^{155}Gd and ^{157}Gd as a function of rod burnup.

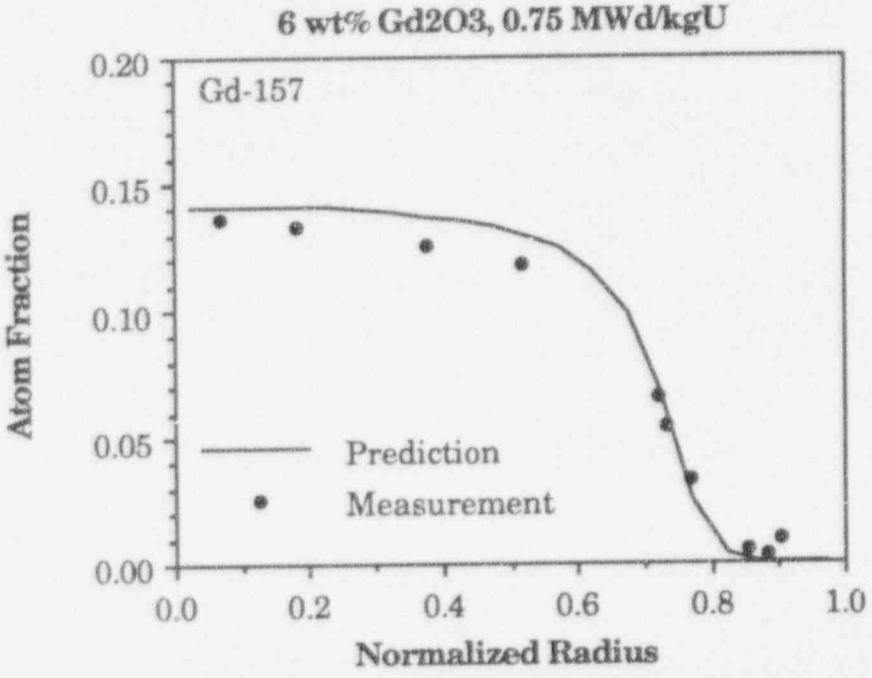

Figure B-2 **Comparison between calculated and measured radial distribution of ^{155}Gd and ^{157}Gd atom fractions.**

B.2.7 Discussion

The microburnup model described in Sections B.2.1 and B.2.2, does not have resonance shielded cross sections and as such only the infinite dilution data are utilized in 25 groups. This simplification does not affect the radial power distribution when BA is present, however, when the Gd isotopes (^{155}Gd, ^{157}Gd) are depleted the model does not redistribute the plutonium production properly, i.e., peak the Pu concentration at fuel periphery. Therefore for fuel rod modelling it is more appropriate that, upon the depletion of BA isotopes, the empirical correlation provided by Palmer et al (Reference B-8) which redistributes Pu properly across the pellet is utilized. Figure B-3 shows evaluation of radial power distribution with burnup for an ABB Gd-bearing SVEA-64 (8x8) fuel rod with gadolinia concentration of 3.95 wt%.

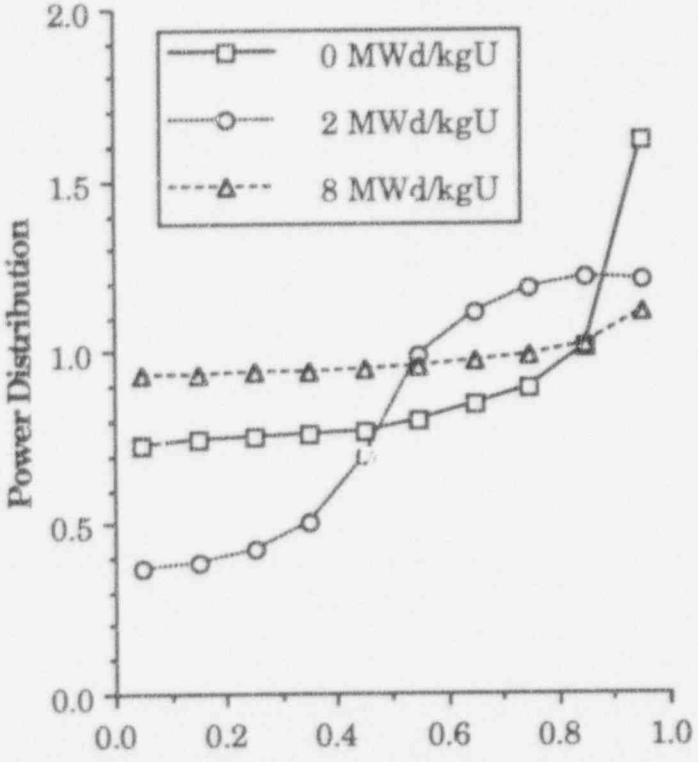

Figure B-3 **Radial power distribution calculated at different burnups for ABB SVEA-64S (8x8) fuel rod with pellet radius r_0= 5.22 mm, lattice pitch of 15.8 mm, ^{235}U enrichment of 3.17 wt%, and Gd_2O_3 concentration of 3.95 wt%. Computation are done for 10 radial annuli, i.e., each calculated point is an average over an annulus.**

B.3 Gas Atom Diffusion and (U, Gd)O_2 Structure

The fission product gases such as Xe and Kr, generated during fuel irradiation, at sufficiently high temperatures diffuse to UO_2 grain boundaries from where a fraction of them get released to the "free" volume of the fuel rod. Diffusion theory (Reference B-9) shows that the time evolution of the concentration of gas atoms on the grain boundaries, N, may be approximated by :

$$N \approx D_n^{1/2}\, t^{3/2} \quad \text{for short times} \tag{B-23}$$

$$\approx D_n\, t \quad \text{for long times, re-solution dominant} \tag{B-24}$$

where D_n is the net diffusion coefficient attenuated by the presence of intergranular traps (gas bubbles) and t the time. Thus the fission product gas release is proportional to the net diffusion coefficient as described by Equations (B-23) and (B-24). D_n is related to the intrinsic gas atom diffusion coefficient D via (Reference B-9):

$$D_n = \frac{C_s}{C_0} D = \frac{R_{out}}{R_{in}+R_{out}} D \qquad \text{(B-25)}$$

where C_s is the concentration of gas atoms in solution and C_0 the total gas atom concentration (in solution and in traps), R_{in} and R_{out} are the rates for trapping and detrapping of gas atoms respectively.

If crystal of UO_2 is grown with controlled amounts of Gd_2O_3 the charge distribution existing in the original UO_2 lattice modifies. The positive ion Gd keeps its +3 charge when dissolved in UO_2. To ensure the electric neutrality in the lattice an oxygen ion may be removed from the lattice, thereby producing a negative ion (anion) vacancy. Commonly in a situation where oxygen potential is not very large a mixture of higher valance uranium ions (U^{+5} and U^{+6}) and oxygen vacancies can result in the replacement of U^{+4} atoms by Gd^{+3} atoms.

In the light of the above consideration it can be asserted that the gas atom diffusion coefficient in urania-gadolinia solid decreases due to increase in the number of the intragranular traps. Consequently, this decrease in diffusion coefficient lowers the amount of fission gas release during the irradiation process.

In regard to fission gas release, it is argued that the increase in temperature of urania- gadolinia fuel can be compensated by the decrease of fission gas diffusion coefficient. In order to model this effect the following assumptions are made:

(i) At zero gadolinia concentration we should recover the pure UO_2 diffusion coefficient.

(ii) Evaluation of gas diffusion coefficient data in UO_2 (Reference B-10) shows that the intrinsic and effective diffusion coefficients are similar below a certain temperature T_0, i.e., at $T < T_0 \approx 1073$ K, $D_n \approx D$.

(iii) The expected higher fission gas release due to higher fuel temperature of the fuel during irradiation should be compensated by the reduction of the fission gas diffusion coefficient. The amount of this compensation has been decided by experimental data.

Thus the gas diffusion coefficient correlation in UO_2 can be extended to embody the effect of the gadolinia additive. This change is made with the assumptions (i) - (iii) described above. Performing this task, a gadolinia concentration dependent gas diffusion coefficient is obtained:

$$D_n = D[1 - a\frac{Q}{T}(1-\frac{T_0}{T})x] \quad \text{for } T>T_0 \tag{B-26}$$

where a and Q are constants obtained from experiments. In our calculation we have used a=2.14 and $D=D_0e^{-Q/T}$ where D_0 and Q are given in Table B-1. Using these values the net diffusion coefficient as a function of temperature and gadolinia concentrations are displayed in Figure B-4.

TABLE B-1

FISSION PRODUCT GAS DIFFUSION COEFFICIENT: $D=D_O\,E^{-Q/T}$, [M^2/S]

	T<1381 K	1381 <T<1650 K	T>1650 K
Q	9508	22884	6614
D_o	1.51×10^{-17}	2.14×10^{-13}	1.09×10^{-17}

Fission gas product retention can be studied by gamma spectroscopy. Some ABB Gd-bearing fuel rods irradiated up to a burnup of 42.4 MWd/kgU have been examined by axial and radial gamma scanning (on sliced pieces of fuel), (References B-11 through B-12). The measurements show that Gd-bearing fuel retains mobile fission products better than UO_2 fuel, even though the Gd-pellets are operating at a higher temperature.

In this test samples were taken from pieces of rods with axial mixing of Gd-doped pellets and UO_2 pellets with the same ^{235}U enrichment, i.e., similar power histories after a few months of operation. It was found that less fission-product migration had taken place in Gd-bearing fuel (Reference B-11).

ABB manufactured Gd-bearing fuel rods have been post irradiation examined and their fission gas release fractions were determined by destructive methods. These rods were 8x8 design (Reference B-13) and were irradiated in different ABB Atom built BWRs up to a rod average burnup of 42.4 MWd/kgU. The model presented in this note has been implemented in the fuel performance code STAV6.2 and were used to evaluate the fission gas release behaviour of the considered rods.

First individual power histories for these rods were calculated utilizing the ABB reactor physics codes. Then using nominal fuel rod design data, Table B-2, and best estimate models in STAV6.2, the fission gas fraction of the rods are predicted. Figure B-5 shows the overall comparison between measured and predicted release fractions values. As can be seen the release behaviour of seven of the rods are predicted very well, two rods are overpredicted and one rod is underpredicted.

In conclusion gamma scanning measurements and fission gas release determination of Gd-bearing fuel rods support the assumptions made in modelling the fission gas release behaviour of these rods.

TABLE B-2

NOMINAL FUEL ROD DATA FOR ABB ATOM 8X8 ASSEMBLY DESIGN

Rod diameter	12.25 mm
Clad wall thickness	0.80 mm
Pellet diameter	10.44 mm
Clad material	Fully annealed Zircaloy-2
Fuel rod length	3950 mm
UO_2 column length	3680 mm
Pellet density	10.49 g/cm^3
Fill gas	Helium
Fill pressure	0.1-0.4 MPa
Gadolinia concentrations	2-5 wt%

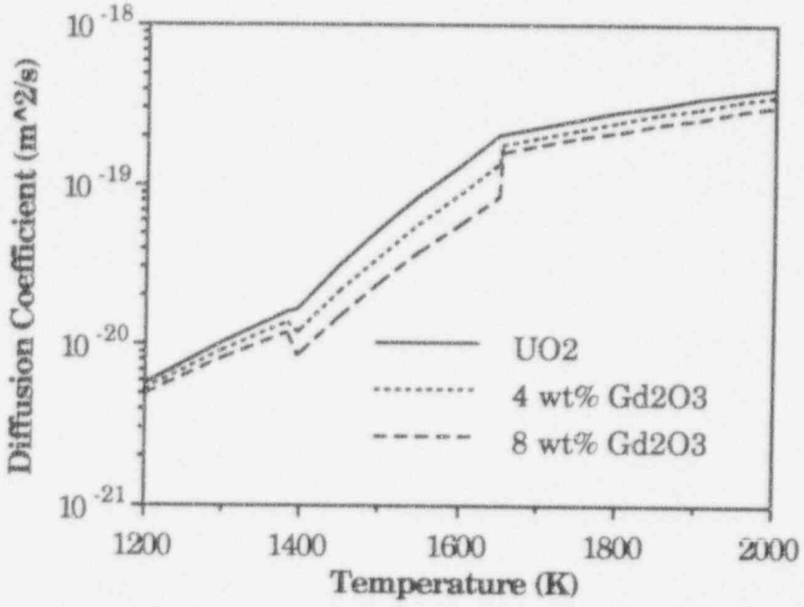

Figure B-4 **Calculated net diffusion coefficient of fission gases in $(U,Gd)O_2$ fuel for different gadolinia concentrations.**

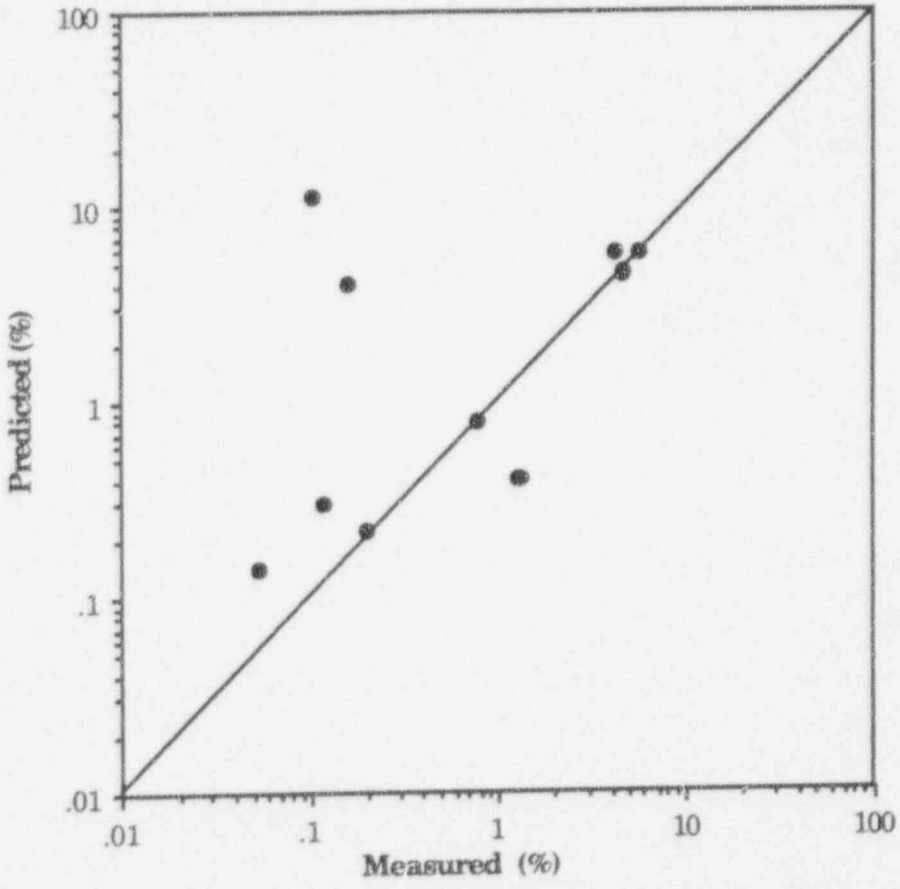

Figure B-5 **Comparison between calculated and measured fission gas release. The rods were irradiated in BWRs up to a burnup of 42.4 MWd/kgU and contained gadolinia concentrations in the range of 2 to 5 wt%.**

B.4 Summary

In this appendix the influence of Gd concentration upon nuclear, thermal and fission product gas behaviour of $(U,Gd)O_2$ is modelled. The nuclear model BURAS predicts the density of ^{155}Gd and ^{157}Gd as a function of burnup, and their distribution across the fuel pellet. The corresponding power distribution across pellet which has a bearing on fuel temperature thus can be determined.

It is shown, based on fission product retention and gas release behaviour of ABB manufactured Gd-fuel rods, that the net gas

diffusion coefficient in $(U,Gd)O_2$ is lower than in UO_2 for increasing Gd_2O_3 concentrations. An empirically based correlation for the net diffusion coefficient is constructed and implemented in the STAV6.2 code for evaluation of fission gas release data obtained from a number of irradiated Gd-bearing fuel rods. The agreement between model predictions and measurements are quite good despite of the complexity of the involved phenomena.

B.5 References

B-1 Hj. Matzke, Nucl. Appl., Vol. 2, pg. 131, 1966.

B-2 Hj. Matzke, J. Nucl. Mater., Vol. 21, pg. 190, 1967.

B-3 G. I. Bell and S. Glasstone, *Nuclear Reactor Theory*, Robert E. Krieger Publishing, New York, 1979.

B-4 R. J. Stammler and M. J Abbate, *Methods of Steady-State Reactor Physics in Nuclear Design*, Academic Press, London, 1983.

B-5 A. Fuji, A. Toba, T. Iwai, S. Izutsu, K. Kato, T. Ishida, H. Nozaki, T. Seino,T. Tanzawa, K. Sakurada, Proceedings of the Topical Meeting on Advances in Fuel Management, Pinehurst, North Carolina, March 2-5, 1986.

B-6 L. W. Newman, Development and Demonstration of an Advanced Extended Burnup Fuel Assembly Incorporating Urania-Gadolinia, DOE/ET/34212-36 (BAW-1681-2), August 1982.

B-7 F. B. Skaogen, A. H. O'Leary and K. E. Karcher, Proceedings of ANS Topical Meeting on LWR Fuel Performance, Williamsburg, Virginia, April 17-20, 1988.

B-8 I. D. Palmer, K. W. Hasketh and P. A. Jackson, IAEA Specialist Meeting on LWR Element Performance Modelling, Preston, UK, March 15-19, 1982.

B-9 M. V. Speight, Nucl. Sci. Eng., Vol. 37, pg. 180, 1969.

B-10 R. J. White and M. O. Tucker, J. Nucl. Mater., Vol. 118, pg. 1-38, 1983.

B-11 S. O. Andersson, E. Patrakka, L. Hyden, H. Pettersson and B. Grapengiesser Proceedings of Water Reactor Fuel Technology and Utilization, Stockholm, 13-19 Sept., 1986, International Atomic Energy Agency, Vienna 1984

B-12 B. Grapengiesser, A. R. Massih, O. Nylund, L. Hyden, S. O. Andersson, E. Patrakka and G. Rönnberg, Proceedings of ANS on LWR Fuel Performance, Williamsburg, Virginia, April 17-20, 1988.

B-13 S. Persson, A. R. Massih, G. Frenning and R. Lunabba, ANS/ENS Meeting on LWR Fuel Performance, Avignon, France, April 21-24, 1991.

APPENDIX C

GENERALIZED MEAN VALUES OF CRACKED PELLET GAP CONDUCTANCE

ABB

C GENERALIZED MEAN VALUES OF CRACKED PELLET GAP CONDUCTANCE

[Proprietary Information Deleted]

ABB Combustion Engineering Nuclear Operations
Combustion Engineering, Inc.
1000 Prospect Hill Road
Post Office Box 500
Windsor, Connecticut 06095-0500
Telephone: (203) 285-9678
Fax: (203) 285-4117